Heat Transfer Correction Modelling for RANS Simulations on Rough Surfaces

E.S.J. Beitler

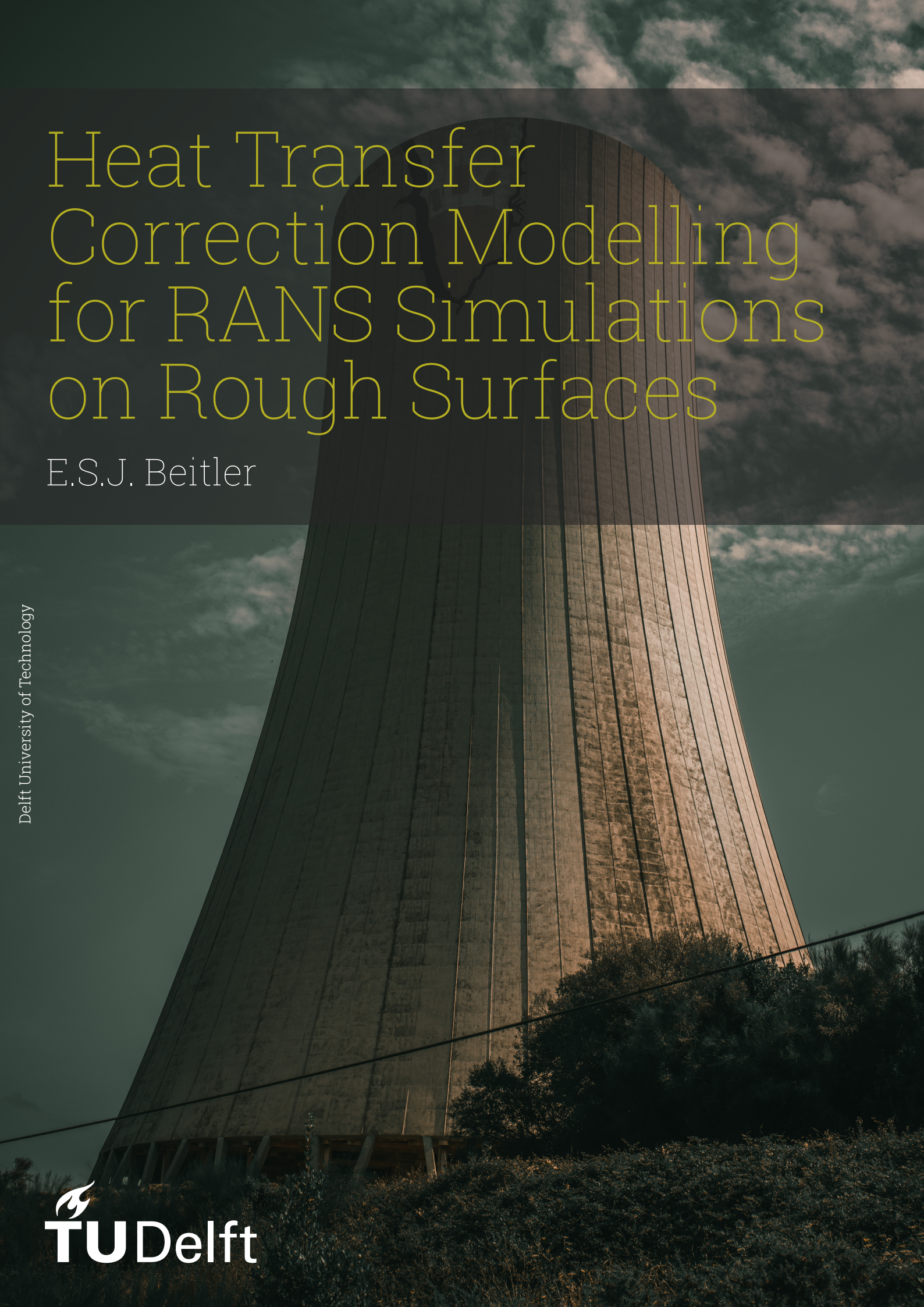

Delft University of Technology

TU Delft

Heat Transfer Correction Modelling for RANS Simulations on Rough Surfaces

by

E.S.J. Beitler

to obtain the degree of Master of Science
at the Delft University of Technology,
to be defended publicly on Wednesday September 21, 2022 at 2:00 PM.

Student number:	5311780	
Project duration:	November 2021 – September 2022	
Thesis committee:	Dr.ir. J.W.R. Peeters,	TU Delft, supervisor
	Dr. A. Mathur,	NRG, supervisor
	Prof.dr.ir. B.J. Boersma,	TU Delft
	Prof.dr.ir. K. Hooman,	TU Delft
	Prof.dr.ir. R. Pecnik	TU Delft

TU Delft

Abstract

The Nuclear Research and consultancy Group (NRG) performs CFD simulations to improve the safety of nuclear installations and conducts research leading to new computational methods. One of the problems encountered in nuclear installations is that vital parts of the reactor, such as the fuel rod bundle, corrode over time. Corrosion leads to roughness elements on the surface which affect the heat transfer. To increase safety and reduce costs, it is of paramount importance to predict the heat transfer accurately when the surface is rough. The effect of roughness on a flow is an increase in both skin friction and heat transfer. Current models rely on the Reynolds analogy to calculate the heat transfer. Because in most applications pressure has no effect on heat transfer, it is often overestimated. In this thesis the accuracy of RANS modelling with respect to predicting heat transfer rates from or to a rough wall has been investigated.

It was found that a model for Low Reynolds Number meshes showed promising results. A downside of a RANS simulation on a Low Reynolds Number mesh is the increased amount of computational time due to fully resolving the velocity and temperature profiles compared to one on a High Reynolds Number mesh where wall functions are used. Therefore the model has been applied on several High Reynolds Number meshes and was compared to DNS results from literature. The results clearly showed that the mesh size was of influence on the predictions. However, a possibility was identified to reduce the mesh size dependency. The damping function was found to be responsible for this dependency and was reformulated using DNS data, resulting in a fitted equation for two different Prandtl numbers. The calibrated damping function which was made for a Prandtl number of 0.7 was validated with experimental results. It was found that the adjusted model could predict the Stanton number accurately and that the mesh size dependency was greatly reduced.

For future research it is recommended that the damping function should be calibrated for other Prandtl numbers as well, so the different damping functions could be combined in a single Prandtl dependent equation.

Contents

1

Introduction

The Nuclear Research & consultancy Group (NRG) is a company specialized in research, development and production of medical isotopes for, among other, cancer diagnosis and treatment. They also research and advise about safety topics in existing nuclear power plants and innovating concepts such as thorium- and liquid-metal reactors [1]. Their head office is located in Petten at the Energy and Health Campus.
The Computational Fluid Dynamics (CFD) research group of NRG is focused on performing computations to improve the safety of nuclear installations and conducting research about computational methods to develop new models in order to present more reliable results to their customers. One of their current projects is to better predict heat transfer when rough surfaces are involved. Rough surfaces can appear in various types of nuclear installations, such as water cooled, molten salt and liquid-metal cooled reactors.

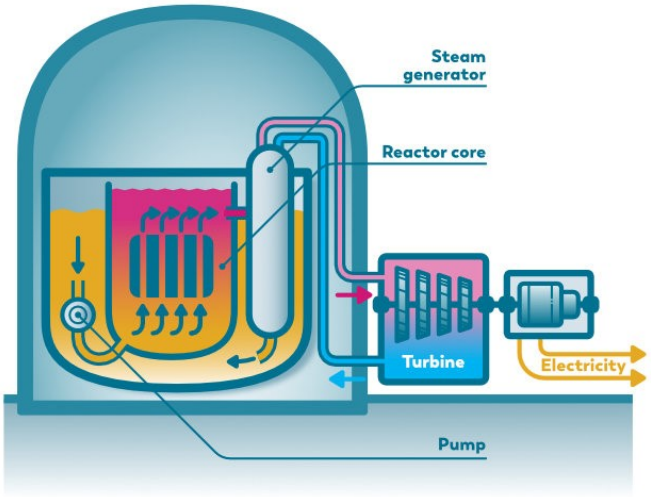

Figure 1.1: Schematic overview of a liquid-metal cooled reactor. The cooled down metal (yellow) is pumped trough the reactor core. Due to the nuclear reactions, the core heats up. The heat is transferred to the liquid metal which is heated up (pink). The liquid metal is then cooled down again by heating up cooled down water and turning it into steam. Finally, the steam is used to generate electricity. Figure from NRG.

For example, in liquid-metal reactors, metals are used for the cooling of the reactor core. In contrast to pressurized water reactors (PWR), the coolant does not have to be pressurized and therefore the risk of accidents is decreased. A schematic overview of a liquid-metal cooled reactor can be found in Figure 1.1. The benefit of these reactors is the wide temperature operating range of the coolant [2]. Besides, metals generally have a high thermal conductivity which results in efficient transportation of thermal energy. However, a downside of liquid-metal cooled reactors is that often the metal is corrosive. The surface structure of fuel rods, pipes and casings may become corroded and the surface becomes

rough, resulting in a loss of structural integrity [3]. This challenge also arises in water cooled reactors and a corroded fuel rod bundle for such a reactor can be seen in Figure 1.2.

Figure 1.2: Corroded fuel rods at the Palo Verde Nuclear Generating Station. Figure from Walter et al. [4].

Besides compromising the structural integrity, also the shear stress and heat transfer are affected. Therefore, research is being done on surface roughness and its effect on turbulent heat transfer. In this thesis, multiple existing computational models have been investigated to better predict the heat transfer when roughness is involved. One of these models has been implemented in a CFD solver for RANS simulations, tested and finally improved.
From the literature study of Chapter 2, a promising RANS model was found for Low Reynolds Number meshes [5] by Aupoix [5]. A downside of a RANS simulation on a Low Reynolds Number mesh is the increased amount of computational time due to fully resolving the velocity and temperature profiles compared to one on a High Reynolds Number mesh where wall functions are used. Therefore, the following research questions have been formulated:

- How does the thermal correction model from Aupoix [5] perform on a High Reynolds Number mesh in a channel flow and how do the results depend on the mesh size?
- How can the thermal correction model from Aupoix [5] be modified so the performance on a channel flow is improved?
- To what extent does the modified thermal correction model improve heat transfer calculations on a developing boundary layer over a flat plate?

Even though the motivation for this thesis stems from nuclear applications, the problem of predicting heat transfer due to rough surfaces appears in different engineering fields such as icing on airfoils and weather predictions. Therefore, the findings of this thesis can also be utilized when heat transfer over rough surfaces is encountered in general.

2

Literature Study

This chapter acts as the main body of the literature study. Firstly, some fundamentals are explained about turbulence and heat transfer. Because the thesis is a numerical study, the next section discusses the used scaling in various papers to simplify the Navier-Stokes equations. Furthermore, the RANS equations and RANS turbulence models are explained in this section. In the third section roughness is explained and its effect on momentum and heat transfer. In section four, the failure of the Reynolds analogy is presented, together with correction models posed by various authors to overcome this failure. Finally, the literature study is concluded.

2.1. Fundamentals

2.1.1. Laminar and Turbulence Flow

This thesis focuses on heat transfer in turbulent flows. It is however important to first explain the difference between laminar and turbulent flows. In laminar flows, fluid particles move in smooth lines from one point to the other and under certain conditions the flow can be solved analytically. Turbulent flow is described as unstable and chaotic. When the Reynolds number of the flow reaches a certain value, the flow is qualified as turbulent. The Reynolds number is defined in Equation 2.1 in which L is a characteristic length, ρ the density, U the velocity and μ the dynamic viscosity. When a flow is turbulent, it can no longer be solved analytically and vortices can be observed (eddies).

$$Re = \frac{\rho U L}{\mu} \tag{2.1}$$

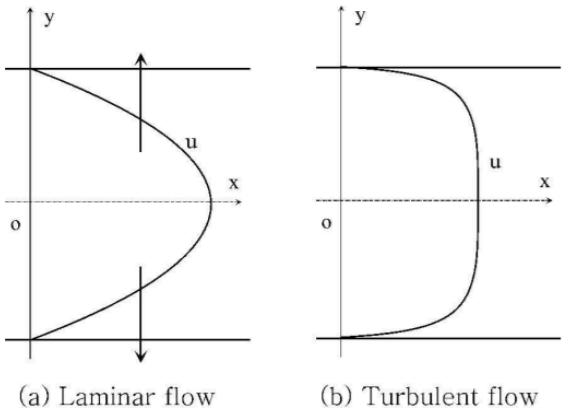

Figure 2.1: Velocity profiles for laminar and turbulent flows [6].

In Figure 2.1 the general shape of a laminar and turbulent velocity profile has been plotted. Turbulent flow differs from a laminar flow in such a way that the velocity gradient at the walls is higher and a more

uniform shaped flow in the center region. The higher velocity gradient at the wall, results in a higher wall shear stress and therefore a higher pressure loss [7].

2.1.2. Turbulent Flows over Smooth Walls

Textbooks by Townsend [8] and Pope [9] described the overall structure of turbulence in wall bounded flows. They describe that when the the velocity and length scales are rewritten in terms of the friction velocity, all wall bounded turbulent flows exhibit the same velocity profile. Therefore the friction velocity (Equation 2.2), dimensionless wall normal distance (Equation 2.3) and dimensionless velocity (Equation 2.4) are introduced. In these equations is τ_w the wall shear stress, ρ the density and ν the kinematic viscosity.

$$u_\tau = \sqrt{\frac{\tau_w}{\rho}} \tag{2.2}$$

$$y^+ = \frac{y u_\tau}{\nu} \tag{2.3}$$

$$u^+ = \frac{u}{u_\tau} \tag{2.4}$$

For $y^+ < 5$ it is observed that viscosity is dominant [10] and the mean velocity can be expressed as in Equation 2.5 [11]. This region is called the viscous sub layer. In the viscous sub layer velocity fluctuations are induced by the turbulence above the viscous sublayer [12].

$$u^+ = y^+ \tag{2.5}$$

For $y^+ > 30$, the velocity profile follows a logarithmic function. Therefore, this region is called the logarithmic layer [12]. In this region the Reynolds stress is dominant compared to the viscous stress. The logarithmic velocity profile can be described using Equation 2.6 [13]. In this equation, k is the von-Kármán constant which is approximately 0.41. For C, most values mentioned in literature are somewhere between 5.0 and 5.2 [14, 10, 13]. The region between the viscous and logarithmic layer is called the buffer zone. In this region, both the viscous and Reynolds stress are of similar magnitude [15].

$$u^+ = \frac{1}{k} \log\left(y^+\right) + C \tag{2.6}$$

Without modification, the wall shear stress is underestimated in CFD because the gradient at the wall is underestimated with a linear approximation. To increase the calculated wall shear stress, an eddy viscosity ν_t is introduced. The eddy viscosity is added to the molecular viscosity and thus increasing the calculated viscous forces as the shear stress τ_w has now become [16]:

$$\tau_w = -\rho\left(\nu + \nu_T\right)\frac{\partial \overline{u}}{\partial y} \tag{2.7}$$

In which $\overline{u}$ is the average velocity. The wall shear stress can be made dimensionless by dividing it by the local dynamic pressure [7] introducing a skin friction factor C_f, see Equation 2.8 in which U_∞ is the free stream velocity for a flow over a flat plate.

$$C_f \equiv \frac{\tau_w}{\frac{1}{2}\rho U_\infty^2} \tag{2.8}$$

For the use of pipe and duct flows, the Darcy friction factor $\overline{f_D}$ is introduced. The Darcy friction factor is used to estimate the pressure drop. The pressure drop over a certain pipe or duct can be found using Equation 2.9 in which U_B is the bulk velocity, L the length of the pipe or duct and d_h the hydraulic diameter [7].

$$\Delta P = \frac{1}{2}\rho U_B^2 \frac{L}{d_h}\overline{f_D} \tag{2.9}$$

2.1.3. Convective Heat Transfer

Convective heat transfer is one of the three main methods of heat transfer next to conduction and radiation. Convective heat transfer occurs when flow is forced over a surface. This can either happen due to an external force, such as a pump, (forced convection) or due to buoyancy effects (natural convection). The heat transfer rate can be calculated using Equation 2.10 in which h is the heat transfer coefficient, A the area, T_B the bulk temperature and T_w the temperature of the wall.

$$\dot{Q} = hA\left(T_B - T_w\right) \tag{2.10}$$

The heat transfer coefficient is a constant for a certain flow and can be found using empirical relations. Such a relation for a flow over a flat plate can be found in Equation 2.11. In this equation the Nusselt number is defined as the ratio between convection and conduction and C, m and n are empirical constants.

$$Nu = \frac{hL}{k} = CRe_L^m Pr^n \tag{2.11}$$

2.1.4. Heat Transfer in Turbulent Flows

The transport of both heat and momentum occurs through turbulent eddies from the core region which are transported to other regions in the flow so the physical processes of heat transfer are similar to those of momentum transport [16]. Reynolds proposed a relation between the friction factor C_f and the Stanton number for flows with a Prandtl number close to 1 [17]. This relation can be found in Equation 2.12 in which $St = \frac{Nu}{RePr} = \frac{h}{\rho c_p U_B}$. This is the so-called Reynolds analogy.

$$\frac{C_f}{2} = St \tag{2.12}$$

Besides a velocity profile in wall units, also a temperature profile can be plotted in wall units, see Equation 2.13. In this equation is T_τ the friction temperature and is obtained using Equation 2.14. The heat flux is computed using $q_w = -\rho\alpha\frac{\partial\overline{T}}{\partial y}$.

$$T^+ = \frac{T_w - T}{T_\tau} \tag{2.13}$$

$$T_\tau = \frac{q_w}{\rho c_p u_\tau} \tag{2.14}$$

For a turbulent flow, the gradient of the temperature is also of a higher magnitude compared to the laminar case. The same problem occurs as with the wall shear stress: the heat transfer from the wall is underestimated. Therefore, the thermal diffusivity α is increased by adding a turbulent thermal diffusivity α_t to obtain a better estimate of the wall heat transfer. In practice, α and α_t are replaced by $\alpha = \frac{\nu}{Pr}$ and $\alpha_t = \frac{\nu_t}{Pr_t}$ respectively.

2.2. Numerical Model

In this section, the Navier-Stokes equations are introduced together with a scaling for a channel flow. The benefit of this form of the Navier-Stokes equations for a channel flow, is the relative ease in defining the friction Reynolds number, which is often defined in DNS data. Also, the three main different turbulence models are presented. Next, the RANS equations are introduced together with its closure problem. Finally, several RANS models are explained briefly to overcome this problem.

2.2.1. DNS Scaling

For a channel flow with the channel height H equal to 2δ and cyclic boundary conditions for the in and outlet, the momentum equations seen in Equation 2.15 are scaled by certain length scales.

$$\rho\frac{\partial\vec{u}}{\partial t} + \rho\left(\vec{u}\cdot\nabla\right)\vec{u} = -\nabla P + \mu\nabla^2\vec{u} \tag{2.15}$$

In Busse et al. [18], Peeters and Sandham [19] and Zhou et al. [20], the time t is made dimensionless with the friction velocity $u_\tau = \sqrt{-\frac{\delta}{\rho}\frac{\partial P}{\partial x}}$, which is slightly different from Equation 2.2 to implement a

constant pressure gradient to drive the flow. The position vector, $\vec{x}$, is made dimensionless by the boundary layer thickness δ. The velocity vector $\vec{u}$ is scaled by the friction velocity only and at last the pressure is scaled with the density and friction velocity. These scalings can be found in Equation 2.16.

$$\tilde{t} = \frac{u_\tau}{\delta} t, \quad \tilde{x} = \frac{\vec{x}}{\delta}, \quad \tilde{u} = \frac{\vec{u}}{u_\tau}, \quad \tilde{P} = \frac{P}{\rho u_\tau^2} \tag{2.16}$$

After substituting the scaling equations, rewriting and putting the constant in front of the partial derivatives, the equation becomes:

$$\frac{\rho u_\tau^2}{\delta} \frac{\partial \tilde{u}}{\partial \tilde{t}} + \frac{\rho u_\tau^2}{\delta} (\tilde{u} \cdot \nabla) \tilde{u} = -\frac{\rho u_\tau^2}{\delta} \nabla \tilde{P} + \frac{\mu u_\tau}{\delta^2} \nabla^2 \tilde{u} \tag{2.17}$$

When Equation 2.17 is multiplied with $\frac{\delta}{\rho u_\tau^2}$, the final equation becomes Equation 2.18 in which $\frac{1}{Re_\tau} = \frac{\nu}{\delta u_\tau}$.

$$\frac{\partial \tilde{u}}{\partial \tilde{t}} + (\tilde{u} \cdot \nabla) \tilde{u} = -\nabla \tilde{P} + \frac{1}{Re_\tau} \nabla^2 \tilde{u} \tag{2.18}$$

Also the thermal transport equation has been scaled and can be found in Equation 2.19. The assumption has been made that $h = C_p T$ with C_p being a constant and $\alpha = \frac{k}{\rho C_p}$.

$$\frac{\partial T}{\partial t} + (\vec{u} \cdot \nabla) T = \alpha \nabla^2 T \tag{2.19}$$

For the velocity, time and position the same scaling has been used. The temperature has been scaled with the wall temperature T_w and friction temperature $T_\tau = \frac{q_w}{\rho C_p u_\tau}$. The dimensionless temperature becomes:

$$\Theta = \frac{T - T_w}{T_\tau} \tag{2.20}$$

Equation 2.19 has been fully written in Equation 2.21.

$$\frac{\partial T}{\partial t} + u \frac{\partial T}{\partial x} + v \frac{\partial T}{\partial y} + w \frac{\partial T}{\partial z} = \alpha \left(\frac{\partial^2 T}{\partial x^2} + \frac{\partial^2 T}{\partial y^2} + \frac{\partial^2 T}{\partial z^2} \right) \tag{2.21}$$

Filling in the scaled variables, moving the constants to the front and applying the right boundary conditions for a cyclic channel flow with constant heat flux, the following equation can be derived

$$\frac{T_\tau u_\tau}{\delta} \frac{\partial \Theta}{\partial \tilde{t}} + \frac{T_\tau u_\tau}{\delta} \left(\tilde{u} \frac{\partial \Theta}{\partial \tilde{x}} + \tilde{v} \frac{\partial \Theta}{\partial \tilde{y}} + \tilde{w} \frac{\partial \Theta}{\partial \tilde{z}} + \frac{\partial T_w}{\partial \tilde{x}} \right) = \alpha \frac{T_\tau}{\delta^2} \left(\frac{\partial^2 \Theta}{\partial \tilde{x}^2} + \frac{\partial^2 \Theta}{\partial \tilde{y}^2} + \frac{\partial^2 \Theta}{\partial \tilde{z}^2} \right) \tag{2.22}$$

After multiplying with $\frac{\delta}{T_\tau u_\tau}$ the equation reduces to Equation 2.23 in which $\frac{1}{Pe} = \frac{\alpha}{\delta u_\tau} = \frac{1}{Re_\tau Pr}$.

$$\frac{\partial \Theta}{\partial \tilde{t}} + \tilde{u} \frac{\partial \Theta}{\partial \tilde{x}} + \tilde{v} \frac{\partial \Theta}{\partial \tilde{y}} + \tilde{w} \frac{\partial \Theta}{\partial \tilde{z}} + \frac{\partial T_w}{\partial \tilde{x}} = \frac{1}{Pe} \left(\frac{\partial^2 \Theta}{\partial \tilde{x}^2} + \frac{\partial^2 \Theta}{\partial \tilde{y}^2} + \frac{\partial^2 \Theta}{\partial \tilde{z}^2} \right) \tag{2.23}$$

Finally, Equation 2.23 can be written more compact again to Equation 2.24 in which $q_s = \frac{\partial T_w}{\partial \tilde{x}}$.

$$\frac{\partial \Theta}{\partial \tilde{t}} + (\tilde{u} \cdot \nabla) \Theta = \frac{1}{Pe} \nabla^2 \Theta - q_s \tag{2.24}$$

The wall temperature gradient $\frac{\partial T_w}{\partial x}$ is not equal to zero and has a constant value for a constant heat flux boundary condition for the upper and lower wall. Meaning for a cyclic channel flow, this term acts as a source term and the bulk temperature keeps increasing. To reach a steady state, this heats needs to be removed by a heat sink.
For a constant temperature boundary condition it is also possible to make q_s a constant, which was the approach by Peeters and Sandham [19]. In that case, q_s is equal to unity.

2.2.2. Different turbulence models

In CFD, there are three main turbulence models. The first being a Direct Numerical Simulation (DNS), in which the flow is solved up to the smallest length scales present in a turbulent flow. These smallest length scales are called the Kolmogorov length scales and are found by characterizing the length, time and velocity by the kinematic viscosity ν and dissipation rate ϵ. The Kolmogorov scales can be found in Equation 2.25 for the length, time and velocity respectively.

$$\eta = \left(\frac{\nu^3}{\epsilon}\right)^{\frac{1}{4}}, \quad \tau = \left(\frac{\nu}{\epsilon}\right)^{\frac{1}{2}}, \quad v = (\nu\epsilon)^{\frac{1}{4}} \tag{2.25}$$

Combining with the scaling of the dissipation rate $\epsilon \propto \frac{U^3}{L}$ [12], in which U and L are the macroscopic length scales, it holds that $\frac{L}{\eta} \sim Re^{\frac{3}{4}}$. To perform a DNS simulation, the number of grid points scales linearly with the expression mentioned before. The number of time steps also scale linearly with the number of grid points to maintain computation stability (e.g. Courant number). This means that the total computational costs for a 3D simulation scales with $N_L^3 N_T \sim Re^3$ in which N_L and N_T are the number of grid points and time steps respectively. The computational costs explode for higher Reynolds number and are therefore not suited for complex and industrial simulations.
To decrease computational costs, Large Eddy Simulation (LES) can be used. In LES, the smallest turbulent eddies are modelled and the largest turbulent eddies are resolved. A LES simulation is always 3D and time dependent. However, LES simulations still require a significant amount of computing power. To even further reduce computational times, the third and last model, Reynolds Averaged Navier-Stokes (RANS), is explained. For the thesis only RANS simulations were performed, because low computational costs are required for industrial applications. In the next section, RANS is explained and some corresponding equations are derived.

2.2.3. RANS

Turbulent flows are chaotic and have fluctuating values for velocity, pressure and temperature. For most applications it is not required to know these exact fluctuating variables, so statistical quantities are derived such as the mean and standard deviation. For RANS calculations the instantaneous velocity and pressure are decomposed in a mean and fluctuating value. See Equation 2.26 in which a bar above a variable indicates the mean and a prime indicates a fluctuating variable.

$$u_i = \overline{u_i} + u_i', \quad P = \overline{P} + P' \tag{2.26}$$

Equation 2.26 can be substituted in the Navier-Stokes equations (2.27 and 2.28).

$$\frac{\partial u_i}{\partial x_i} = 0 \tag{2.27}$$

$$\frac{\partial u_i}{\partial t} + u_j \frac{\partial u_i}{\partial x_j} = -\frac{1}{\rho}\frac{\partial P}{\partial x_i} + \nu \frac{\partial^2 u_i}{\partial x_i^2} \tag{2.28}$$

After applying the Reynolds conditions and some rewriting, this yields for the mass equation:

$$\frac{\partial \overline{u_i}}{\partial x_i} = 0, \quad \frac{\partial u_i'}{\partial x_i} = 0 \tag{2.29}$$

For the momentum equation it yields:

$$\frac{\partial \overline{u_i}}{\partial t} + \overline{u_j}\frac{\partial \overline{u_i}}{\partial x_j} = -\frac{1}{\rho}\frac{\partial \overline{P}}{\partial x_i} + \nu \frac{\partial^2 \overline{u_i}}{\partial x_i^2} - \frac{\partial \overline{u_i' u_j'}}{\partial x_j} \tag{2.30}$$

The term $-\frac{\partial \overline{u_i' u_j'}}{\partial x_j}$ appeared in the momentum equation and can be interpreted as turbulent transport of the fluctuating components of the velocity. This is equivalent to a stress acting on a surface and is therefore known as the Reynolds stress [12]. The problem is that new unknown quantities are introduced and the number of unknown quantities are bigger than the number of equations. An extra relation is required to solve the system of equations. This is called the closure problem in RANS equations. The same problem occurs for the thermal transport equation seen in Equation 2.31. When the temperature

is decomposed in a mean value and fluctuating value (Equation 2.32) and is substituted, the equation can be rewritten into Equation 2.33 in which the term $-\frac{\partial \overline{u_j' T'}}{\partial x_j}$ appeared.

$$\frac{\partial T}{\partial t} + u_j \frac{\partial T}{\partial x_j} = \alpha \frac{\partial^2 T}{\partial x_i^2} \tag{2.31}$$

$$T = \overline{T} + T' \tag{2.32}$$

$$\frac{\partial \overline{T}}{\partial t} + \overline{u_j} \frac{\partial \overline{T}}{\partial x_j} = \alpha \frac{\partial^2 \overline{T}}{\partial x_i^2} - \frac{\partial \overline{u_j' T'}}{\partial x_j} \tag{2.33}$$

In RANS, these unknown closure terms are approximated by empirical relations or additional transport equations for the turbulent kinetic energy k, turbulent dissipation ϵ or specific dissipation ω. There are two types of models: Eddy viscosity models (EVM) en Reynolds Stress Models (RSM). In this thesis only attention is paid to EVM.
EVM rely on the hypothesis that turbulence leads to momentum exchange between elements of the fluid. This results in the assumption that the Reynolds stress term is proportional to the mean strain rate times a constant ν_t, the eddy viscosity. See Equation 2.34 in which S_{ij} is the strain rate tensor, δ_{ij} the Kronecker delta and k the turbulent kinetic energy.

$$-\overline{u_i' u_j'} = 2\nu_t S_{ij} - \frac{2}{3}\delta_{ij} k \tag{2.34}$$

The equation above can then be substituted into the RANS equation, removing the unknown Reynolds stress term. A downside of this assumption is that these models are unable to capture an-isotropic effects because the Reynolds stress tensor is reduced to a single parameter. The eddy viscosity ν_t is however still unknown and must be computed by for example the Prandtl mixing length, $k-\epsilon$ or $k-\omega$ model. For the Prandtl mixing length, the eddy viscosity can be found using Equation 2.35 in which κ is the von-Kármán constant and L is the size of the biggest eddy possible, which is assumed to be the distance to the wall for a certain cell [12].

$$\nu_t = \kappa L^2 \left| \frac{\partial \overline{u}}{\partial y} \right| \tag{2.35}$$

For the $k-\epsilon$ model, the eddy viscosity can be found using Equation 2.36 in which C_μ is a model parameter. k and ϵ are solved for using two additional transport equations [21, 22].

$$\nu_t = C_\mu \frac{k^2}{\epsilon} \tag{2.36}$$

The eddy viscosity for the $k-\omega$ model can be found using Equation 2.37 in which $\omega = \frac{1}{C_\mu}\frac{\epsilon}{k}$. k and ω are also solved using two additional transport equations [23].

$$\nu_t = \frac{k}{\omega} \tag{2.37}$$

Both of the last two mentioned models have their strengths and weaknesses for certain types of flow. The $k-\omega$ model is reported to perform better in transitional flows and in flows with adverse pressure gradients. However, the model is more sensitive to the free-stream boundary condition for ω in shear-free flows. The $k-\omega\, SST$ model combines both models using a blending function. Closer to the wall the $k-\omega$ model is ”stronger” and further away the $k-\epsilon$ model [24].

2.3. Effects on Momentum and Heat Transfer due to Roughness

So far, turbulence and heat transfer have been discussed in flows with smooth walls. However, for this thesis the heat transfer across rough walls were modelled. In this section it becomes clear what the effect on the momentum and heat transfer exactly is due to roughness. Besides a shift in the velocity and temperature profiles, also the increase in momentum and heat transfer are discussed. But first, a short summary is given on how to describe roughness in general.

2.3.1. (Equivalent) sand grain height

To simplify correction models and empirical relations for the velocity and temperature profiles, a length scale was introduced by Colebrook and White [25] to describe roughness, the equivalent sand grain height k_s. The equivalent sand grain height is a parameter for random roughness defined in such a way that it produces the same results as the experiments from Nikuradse [26]. Interested in drag increase on ship hulls due to fouling, Nikuradse performed experimental studies on the pressure drop in rough pipes [26]. He covered the inside of the pipes with sand grains of which the mean height were known and was therefore in fact a flat pipe covered with small spheres. These sand grains can be seen in the top part of Figure 2.2. It was found that the friction increased as a function of $\overline{k}/D$ in which $\overline{k}$ is the mean sand grain height and D the diameter of the pipe.

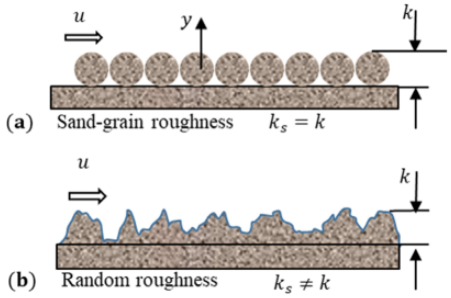

Figure 2.2: Schematic overview of sand-grain roughness and random roughness on a flat plate. Figure from Kadivar et al. [13].

For artificial and random surfaces, the roughness height k can vary and the shape might be different for every single roughness element. Therefore, the roughness height is not equal to the equivalent sand grain height as is the case for the sand grains from Nikuradse. This can be seen in the bottom half of Figure 2.2.
For the different correction models in CFD, which are discussed later, often the equivalent sand grain height is the one and only input parameter. Therefore, it is important to compute the equivalent sand grain height for a certain surface in advance. Several correlations have been developed throughout the years for example by Dirling [27] and Boyle and Stripf [28].

2.3.2. Rough flow regimes

To explain the effects of rough surfaces on the momentum and heat transfer, the roughness Reynolds number k_s^+ needs to be introduced. The roughness Reynolds number is defined according to Equation 2.38. With the roughness Reynolds number, it is possible to compare different rough surfaces and flows at different scales.

$$k_s^+ = \frac{k_s u_\tau}{\nu} \tag{2.38}$$

When the roughness Reynolds number is smaller than $k^+_{s,smooth}$, the roughness is called hydraulically smooth. The roughness elements are well within the viscous sublayer and the influence on the mean flow is negligible. When the roughness Reynolds number is bigger than $k^+_{s,smooth}$ but smaller than $k^+_{s,rough}$, it is called the transitionally rough regime. The influence on the flow due to the roughness is complex. Both viscous and pressure forces are increased and dominant. The exact effect of the transitionally region is still a topic of debate and is therefore unclear [10]. Finally, when the roughness Reynolds number is bigger than $k^+_{s,rough}$, the roughness elements penetrate into the fully turbulence regions. This is called the fully rough regime. The logarithmic profile is now significantly being shifted downwards and the pressure forces are significant, resulting in an even further increase in drag [13].
Several values for $k^+_{s,smooth}$ and $k^+_{s,rough}$ are reported. For example, 2.25 [29] and 5 [26] have been found for $k^+_{s,smooth}$ and for $k^+_{s,rough}$, 70 [26] and 90 [29].

2.3.3. Velocity shift

In an earlier section, the mean flow over a smooth wall has been discussed and the velocity profile for the different layers have been introduced. For flow over a rough wall, this velocity profile does not hold anymore. It is observed by various studies that the velocity profile, especially in the log layer, is shifted downwards [13]. Furthermore, due to the roughness elements, the flow is highly disturbed up to three to five times the roughness height above the surface [30]. Therefore Clauser [31] proposed to modify Equation 2.6 to 2.39 in which Δu_+ is the shift in the velocity profile. The shift can be seen in Figure 2.3 where the velocity profile of a smooth wall is compared to the velocity profile of some experiments with rough walls.

$$u^+ = \frac{1}{\kappa} \ln y^+ + C - \Delta u^+ \tag{2.39}$$

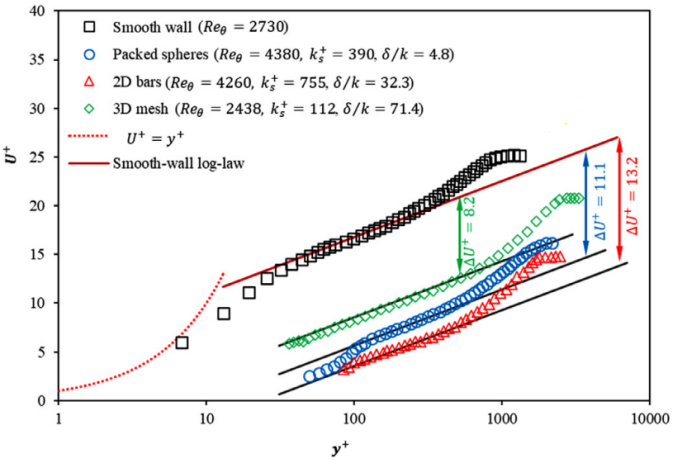

Figure 2.3: The shift in the velocity profile quantified for several experimental studies. Figure used from Kadivar et al. [13].

Multiple empirical relations have been made to compute the velocity shift as function of the equivalent sand grain height. Some relations are split in multiple parts to account for the three earlier mentioned regimes and some use a single expression which is then only valid for the fully rough regime. The first is referred as a "Nikuradse-type" roughness function and the second as a "Colebrook-type" roughness function. A general form of a Nikuradse-type function can be found in 2.40 [13]. In this equation, C_s is a roughness constant and varies from 0.253 for traditional Nikuradse roughness [29] to 0.5 for uniform sand grains and up to 10 for ribs and wire-mesh roughness [13]. An example of a Colebrook-type function, by White [32], can be found in Equation 2.41. This equation is calibrated for the fully rough region only and will therefore give wrong predictions in the hydraulically smooth and transitionally rough regimes.

$$\Delta u^+ = \begin{cases} 0, & \text{if } k_s^+ \leq k_{s,smooth}^+ \\ \frac{1}{\kappa} \ln\left(C_s k_s^+\right) \sin\left(\frac{\pi}{2} \frac{\ln k_s^+ - \ln k_{s,smooth}^+}{\ln k_{s,rough}^+ - \ln k_{s,smooth}^+}\right), & \text{if } k_{s,smooth}^+ < k_s^+ \leq k_{s,rough}^+ \\ \frac{1}{\kappa} \ln\left(C_s k_s^+\right), & \text{if } k_s^+ > k_{s,rough}^+ \end{cases} \tag{2.40}$$

$$\Delta u^+ = \frac{1}{\kappa} \ln\left(1 + 0.3 k_s^+\right) \tag{2.41}$$

However, the shift in the velocity profile becomes zero when the distance to the wall is big enough. In literature this phenomenon is called the Townsend Reynolds similarity for rough walls. At sufficiently high Reynolds numbers outside the viscous layer, turbulent motions are independent of the roughness [10]. Exceptions have been found by, among others, Flack et al. [33] when the boundary layer thickness δ compared to the roughness height is too small ($\delta/k_s \leq 40$). In these cases the velocity defect, $\Delta u^+ = u_s^+ - u_r^+$, remains non zero across the whole flow.

2.3.4. Temperature profile

Due to failing of the Reynolds analogy when rough surfaces are involved (which will be explained later), the shift in the temperature profile does not equal the shift in the velocity profile. Kays and Crawford [34] introduced an analog expression for the temperature profile for rough surfaces. This expression can be found in Equation 2.42 in which ΔT_0^+ is the shift in the temperature profile. When the temperature shift is equal to zero, the Reynolds analogy is recovered [13].

$$T^+ = \frac{Pr_t}{\kappa} \ln\left(\frac{32.6y^+}{k_s^+}\right) + \Delta T_0^+ \tag{2.42}$$

Dipprey and Sabersky introduced an empirical relation for the temperature shift, this relation can be found in Equation 2.43. C_{th}, m and n are constants determined by various papers. For C_{th}, often 0.8 is being used [35, 34]. For m and n, more variance can be found. For example, m and n are found to be 0.2 and 0.44 respectively by Dipprey and Sabersky [35] which Kays and Crawford [34] agreed with. Owen and Thomson [36] suggested 0.45 and 0.8.

$$\Delta T_0^+ = \frac{1}{C_{th}} k_s^{+m} Pr^n \tag{2.43}$$

2.3.5. Drag and heat transfer increase

Another way roughness affects the flow properties, is that the wall shear stress and heat transfer are increased. This can for example be observed by an increase in the pressure drop in pipes. The increase in pressure drop is caused by an increase in form drag and by a blockage effect due to a decrease in the local flow area [13]. The most famous result of the increase in drag, and therefore pressure drop, are the experimental studies by Darcy [37]. Colebrook used these experimental results to come up with an implicit equation for the Darcy friction factor, see Equation 2.44 [38], and is used by Moody [39] to construct the Moody diagram.

$$\frac{1}{f_D^{0.5}} = -2.0 \log\left(\frac{k_s/D_t}{3.7} + \frac{2.51}{\mathrm{Re}\, f_D^{0.5}}\right) \tag{2.44}$$

Flack and Schultz [40] wrote in a review paper about their research that for rough surfaces with a solidity λ smaller than 0.15, the frictional drag increases. For values bigger than 0.15 shielding occurs due to the increase in roughness element density and the frictional drag starts to decrease again. The total drag might still increase due to the pressure drag. In another paper Schultz and Flack [41] performed a study on a systematically varied rough wall and studied the drag increase. They found that the roughness height was the most important length scale, except for the pyramids with the smallest slopes. This might have indicated that these surfaces were more wavy instead of fully rough. In these cases, the equivalent slope was found to be the best predicting parameter for the drag increase.

Next to the increase in drag, an increase in heat transfer is observed in applications where roughness is involved. Due to the increased turbulence levels caused by the roughness elements, mixing of the fluid is stimulated and therefore more heat is being transferred. Turbulence also causes an increase in the temperature gradient near the wall. Some examples found in literature are given in this section.

Jacobi and Shah [42] reviewed the use of longitudinal vortices to increase the heat transfer coefficient in heat exchangers. They explain the use of active and passive methods and the difference between main and secondary flow enhancements. The use of longitudinal vortices are categorized as passive secondary flow inducers. It was found that a pair of longitudinal vortices caused an increase in the heat transfer coefficient at certain locations. For inward rotating vortices (Figure 2.4) this was the inside region and for outward rotating vortices (Figure 2.5) this was the outer region. The main explanation was the local thinning of the boundary layer, thus increasing the temperature gradient. On the other side of the vortices the heat transfer coefficient decreased, but with a smaller magnitude compared to the increase. They concluded in the end that the use of vortices are promising for increasing heat transfer, but that the total potential remained unclear.

Stroh et al. [43] performed a DNS study on a similar topic. They studied the effect of secondary flow caused by streamwise ridges in a channel. These ridges also introduced longitudinal vortices, causing an increase in the heat transfer. It was found that the heat transfer enhancement comes from both the dispersive component of the secondary flow and a strong modification of turbulent flow properties.

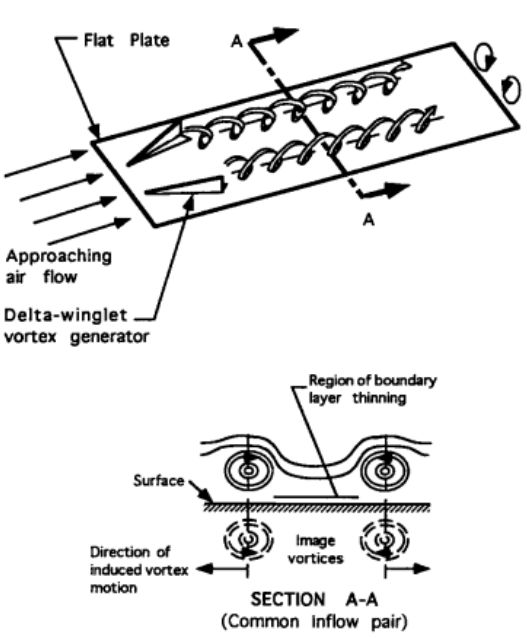

Figure 2.4: Schematic drawing of inward rotating vortices. Figure used from Jacobi and Shah [42].

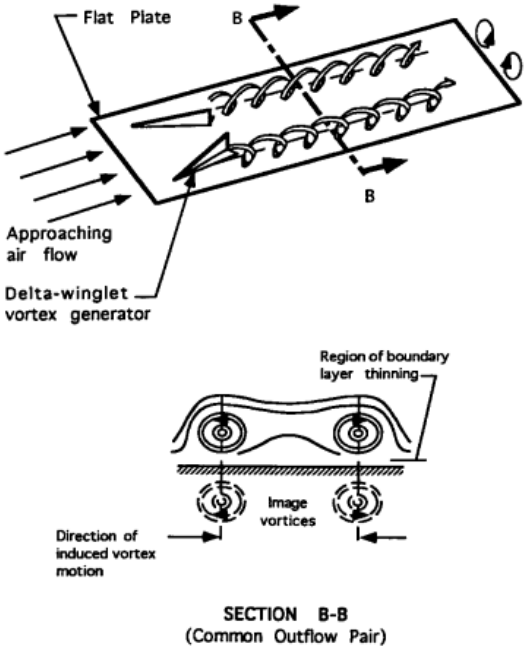

Figure 2.5: Schematic drawing of outward rotating vortices. Figure used from Jacobi and Shah [42].

Stimpson et al. [44] performed a series of experiments on (micro) channels which were made using additive manufacturing. They studied the effect of the introduced surface roughness due to the manufacturing process on the pressure drop and heat transfer. It was found that the Nusselt number increased for all cases compared to the smooth channel. However, the Nusselt number did not increase as much as the friction factor, confirming the failure of the Reynolds analogy for rough flows. They described the introduced roughness not only as a downside due to the increase in friction, but also acknowledged the possibilities for applications where an increase in heat transfer is required.
Soleimani and Eckels [15] reviewed various experimental papers about drag reduction and heat transfer enhancement due to riblets normal to the flow direction. They specifically focused on the cross section of these topics, conditions in which there is a drag reduction but a heat transfer increase. They stated that mostly the tips of the riblets are responsible for the increase in heat transfer for low Prandtl numbers. For high Prandtl numbers, the thermal boundary layer thickness becomes in the order of the riblet size itself. In these cases, the entire rib area plays an important role in the heat transfer, instead of only the tips compared to low Prandtl numbers. Furthermore, they mention the importance of secondary flows and vortices for the increase in heat transfer.

2.4. Modelling Wall Roughness Effects

In literature it has been found that the Reynolds analogy fails when roughness is involved [45, 13, 46]. More specifically, Bons [47] used experimental data to show that the Reynolds analogy factor, $RA = 2St/C_f$, varied in both directions corresponding to the positive and negative pressure gradients. This indicated a more direct effect of the pressure on the wall shear stress and not on heat transfer. The physics involved are somewhat different, because the pressure drag contributed to the skin friction whilst there is no such mechanism for the heat transfer. Therefore heat transfer increases less than the wall shear stress. He also found that when the free stream turbulence intensity was increased, it was the other way around i.e. the heat transfer was increased more than the wall shear stress, indicating the importance of mixing for heat transfer. Furthermore, Hantsis and Piomelli [48] concluded that their data show significant scatter on the Prandtl number dependency. They showed that the mechanisms governing the production of scalar fluctuations and turbulent kinetic energy differ from each other and therefore call for the definition of a scalar equivalent sand grain height, which is analogous to the equivalent sand grain height for the momentum transfer.
To better predict the heat transfer, different models have been developed for RANS simulations. In this

section, first the difference between Low and High Reynolds Number meshes are explained and some momentum transfer correction models are discussed. Secondly, different thermal correction models for LRN and HRN meshes are explained in more detail.

2.4.1. Low and High Reynolds Number

Because CFD often relies on the Reynolds analogy, heat transfer computations need to be improved when roughness is involved. To that goal, several thermal corrections and wall functions have been developed. For the thermal corrections, two general strategies can be followed. For the wall function approach, the cell center of the wall adjacent cell is placed in the log-layer. This means that the Δy^+ value of the first cell adjacent to the wall is larger than 30. This is called a High Reynolds Number (HRN) mesh. For the second strategy, the flow is resolved up to the wall by ensuring Δy^+ is smaller than 1. In this approach, the governing equations are modified to cope with certain turbulence effects. Such a mesh is also called a Low Reynolds Number (LRN) mesh. The difference in computational time between these two meshes is significant. Because the flow is fully resolved up to the wall for a LRN mesh, the flow calculations below the log-layer takes up to 90% of the total computational time [49]. The increase in computational time is due to the need of smaller cells in both the flow and vertical direction, which results in more cells in the mesh and the need of a smaller time step. The smaller time step is the consequence of the requirement that the Courant number, see Equation 2.45, is smaller than 1.

$$C_{max} \geq \frac{u\Delta t}{\Delta x} \tag{2.45}$$

2.4.2. Momentum transfer

The first model is an extension of the Spalart-Allmaras turbulence model by Aupoix and Spalart [50] and is an one-equation model designed for aerodynamics flows [51]. The additional transport equation which is solved for, is the value $\tilde{\nu}$ which is far from walls equal to ν_t. Aupoix and Spalart [50] stated that there are two approaches for increasing the turbulent viscosity ν_t to predict a higher skin friction. First: forcing a value of zero at the wall, the increase in skin friction is than obtained by reducing turbulence damping at the wall. The second approach is by applying a non-zero value for the turbulent viscosity at the wall. This approach can be interpreted as placing a virtual wall located part-way up the roughness. Two different models have been derived in the paper and both use the second approach to alter the turbulent viscosity. For both models it is important that the roughness height must be smaller than the boundary layer, because the flow is averaged over numerous roughness elements. The exact location and geometry is not accounted for, so the flow around each roughness elements is not being solved. The models however differ from each other. The Boeing extension only uses the roughness height, while the other extension uses the friction velocity as well. Both extensions performed well and gave similar results compared to each other and experimental results. However, the question has risen about the use of k_s as input parameter because it might be too general to describe roughness.
Another model which has been modified to cope with roughness, is the $k-\omega\,SST$ model. Aupoix [52] reviewed corrections for the $k-\omega\,SST$ and $k-\omega$ turbulence models, discussed their shortcomings and proposed two new corrections. It is stated that because $k-\omega$ models have no wall damping functions build in, roughness corrections can only be based on modifying the transport equations for k and ω. In particular, the values at the wall are modified to increase the calculated wall shear stress. The first correction for the $k-\omega$ model has been made by Wilcox [23]. In this correction, only the specific dissipation rate at the wall ω_w has been modified. It has been decreased in order to increase the drag. This model had however some shortcomings in the transitional regime and failed completely when applied to the $k-\omega\,SST$ model. Therefore the correction was modified by Hellsten and Laine [53] and Knopp et al. [54] to improve the compatibility. These modifications indeed worked for the $k-\omega\,SST$ model, but the increase in friction was underestimated for the transitionally rough regime. For this reason new corrections were developed by Aupoix [52]. The first correction was based on data from Colebrook [25] and the second on the data from Nikuradse [26]. After the implementation and validation of these models, Aupoix [52] concluded that both models performed satisfactorily, even when pressure gradients were involved. The Colebrook [25] based model was favoured after all because it predicted a slightly higher friction in the transitionally rough regime, indicating a more conservative approach.
Also specifically for the $k-\epsilon$ turbulence model, a correction has been developed. Ambrosini et al. [55]

came up with a correction for LRN meshes with this model. Also for this model no wall damping function is implemented, so the k and ϵ transport equations have been modified. The basis for this model lies in the assumption that the effect of the flow due to roughness is proportional to the local dynamic pressure, $P_{dyn} = \frac{1}{2}\rho u^2$. When this assumption was applied, new equations for k and ϵ appeared with a source term. They concluded that the model showed a qualitative improvement, but quantitatively it lacked accuracy. Therefore an improvement of the model is still required to give satisfactorily results.
Finally, Prakash and Laurendeau [56] developed a wall function which is independent of the turbulence model used. They based their work on log-law functions for the velocity and temperature. They used this approach, instead deriving a wall function analytically, because it was more convenient to be implemented. Starting from the velocity profile of a smooth wall, some modifications have been made to also account for rough surfaces. The wall function was tested using the Spalart-Allmaras and $k-\omega\,SST$ models. It turned out that the skin friction was in good agreement with the LRN counterparts. The results also matched with semi empirical relations and experiments. In the end, the failure of the Reynolds analogy was confirmed for rough surfaces and a thermal correction model has been implemented to predict the temperature profile more accurately. This model is the model from Aupoix [5] and is discussed later.

2.4.3. Wall functions over smooth walls

After discussing momentum correction models, the focus is shifted towards thermal correction models. A good starting point is the paper from Craft et al. [57] in which they developed a wall function for RANS modelling for smooth walls. The benefit of such a wall function is not requiring a fine grid size at the wall and thus decreasing the computational time. They shortly mention the general strategy for developing a wall function; in a wall function, the first near-wall grid node is placed far enough away from the wall such that y_p, which is the center point of the cell, is located in the fully turbulent inner region. Also, the flow over this region is assumed to follow the inner law of the wall. At last, the local equilibrium conditions are then used to estimate the wall shear stress and also to evaluate the source terms in the turbulent transport equations (for example the turbulent kinetic energy k). To determine the wall shear stress, Equation 2.46 is used from Launder and Spalding (1974). In this equation, κ, c_μ, E are constants, k_p the turbulent kinetic energy at the cell center, ρ the density, U_p the velocity parallel to the wall and y_p^* the y position of the cell center in wall units with an alternative definition of the friction velocity $u_\tau = \sqrt{c_\mu^{1/4} k_p}$.

$$\tau_w = \frac{\kappa c_\mu^{1/4} \rho k_p^{1/2} U_p}{\ln E c_\mu^{1/4} y_p^*} \tag{2.46}$$

To integrate the turbulent kinetic energy equation across the near-wall cell, viscous transport of k is neglected and the source term P_k and dissipation term ϵ are not assumed constant which is the usual approach with internal cells. The final result for the source and dissipation term can be found in the following two equations. With these equations it is possible to compute the correct wall shear stress without the need of fine cells near the wall.

$$\overline{P_k} = \frac{\tau_{wall}^2}{\kappa c_\mu^{1/4} \rho k_p^{1/2} y_n} \ln \frac{y_n}{y_v} \tag{2.47}$$

$$\overline{\epsilon} = \frac{1}{y_n}\left[y_v \frac{k_p^{3/2}}{c_l y_v} + \frac{k_p^{3/2}}{c_l} \ln \frac{y_n}{y_v} \right] \tag{2.48}$$

In the wall function from Craft et al. [57], diffusion of enthalpy parallel to the wall is neglected. The convective term perpendicular to the wall is also assumed small compared to the diffusion so the energy transport equation for the wall adjacent cell becomes:

$$\frac{\mu_v^2}{\rho_v^2 k_p}\left(\rho U \frac{\partial T}{\partial x}\right) = \frac{\partial}{\partial y^*}\left[\left(\frac{\mu}{Pr} + \frac{\mu_t}{Pr_t}\right)\frac{\partial T}{\partial y^*}\right] \tag{2.49}$$

For the velocity field a similar approach is used in which also a buoyancy term is included. After the implementation of both the temperature and velocity wall functions, the wall functions have been tested for three test cases. From these test cases, the authors concluded that the computational speed

increased without losing too much accuracy. The size of the wall adjacent cell was still of some influence on the results, showing the possibility for improvement. Some other limitations are the assumption of a Prandtl number of approximately 1 and the need for non-skewed cells near the wall.
Craft et al. [57] mentioned in their article, besides the analytical integration of momentum and energy equations in the wall adjacent cell, a second approach to decrease the computational time. In this second approach, a sub-grid is made in the wall adjacent cell, see Figure 2.6. They explained and implemented this second approach in Craft et al. [58]. They stated that this quasi wall function differs from a LRN mesh, because it decouples the numerical solution of the near-wall region from the main region of the flow. It also uses simplified transport equations (1D only) to reduce complexity. Finally, the pressure-correction equation is also not solved for in the sub-grid. These properties make the simulations faster than conventional LRN approaches. This (quasi) wall function is developed for a smooth wall only. Even though this other method is slower compared to the previous wall function approach, it has some benefits in cases where the Prandtl number is larger than unity. The number of sub-grid cells can be then increased to resolve the thinner thermal sublayer. The model is tested and the paper concludes with the statement that the accuracy is similar compared to LRN approaches with an order of magnitude smaller computational time.

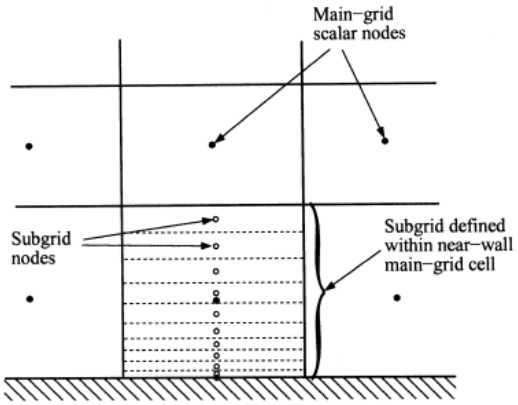

Figure 2.6: Schematic overview of the sub-grid layout in a mesh. Used from Craft et al. [58]

.

2.4.4. Wall functions over rough walls

Suga et al. [59] developed an analytical wall function for flows over both smooth and rough walls. They extended the work of Craft et al. [57] to also account for rough surfaces. In this extension, y_v^* is not longer fixed at a value of 10.7 (which corresponds roughly to a y_v^+ value of 5), but varies depending on the roughness height. As a consequence, the assumed μ_t profile across the wall adjacent cell shift towards higher values, which can be seen in Figure 2.7.

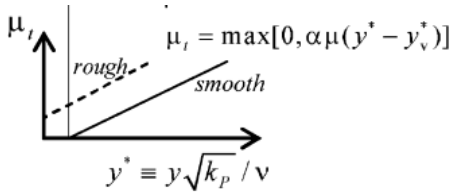

Figure 2.7: Assumed μ_t across the wall adjacent cell [59].

The value of y_v^* can be found with Equation 2.50 in which m is given in Equation 2.51. y_{vs}^* is the viscous sub-layer thickness in the smooth wall case.

$$y_v^* = y_{vs}^* \left[1 - \left(\frac{h^*}{70}\right)^m\right] \tag{2.50}$$

$$m = max\left[\left(0.5 - 0.4\left(\frac{h^*}{70}\right)^{0.7}\right), \left(1 - 0.79\left(\frac{h^*}{70}\right)^{-0.28}\right)\right] \tag{2.51}$$

Unlike in a sub-layer over a smooth wall, the total shear stress now includes the drag force from the roughness elements which is proportional to the local velocity squared and becomes dominant away from the wall, compared to the viscous force. Therefore the momentum equivalent of Equation 2.49 should be modified. In particular, the left hand side including the pressure term is set to be zero when $y^* \leqslant h^*$. Concerning the energy equation, Pr_t is no longer constant across the wall adjacent cell because fluid is trapped around the roughness elements forming a thermal barrier so the turbulent transport of energy is relatively reduced compared to the momentum transport. An increase of the turbulent Prandtl number close to the wall is supported by Nagano et al. [60]. In the paper Suga et al. [59] mentioned that even though it might be better to calculate the turbulent Prandtl number with a non-linear function, it is assumed that the turbulent Prandtl number can be calculated using Equations 2.52, 2.53 and 2.54. The assumed turbulent Prandtl number profile can be seen in Figure 2.8.

$$Pr_t = Pr_t^{\infty} + \Delta Pr_t \tag{2.52}$$

$$\Delta Pr_t = C_0 max\left(0, 1 - \frac{y^*}{h^*}\right) \tag{2.53}$$

$$C_0 = \frac{5.5}{1 + (h^*/70)^{6.5}} + 0.6 \tag{2.54}$$

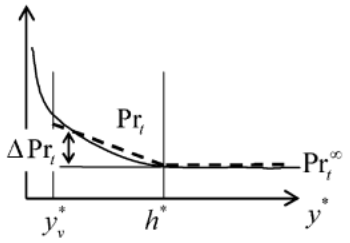

Figure 2.8: Pr_t distribution across the wall adjacent cell, in which the solid line represents the findings of [60] and the dashed line is the assumed profile [59].

These assumptions and therefore the wall function is applicable only for Prandtl numbers ≤ 1 because at higher Prandtl numbers the sub-layer at which turbulent transport of thermal energy is negligible becomes thinner than the viscous sub-layer. The assumption that the turbulent heat flux becomes negligible when $y < y_v$ no longer applies. The analytical solutions of both mean flow and energy equations then can be obtained in the four different cases illustrated in Figure 2.9 in which the assumption has been made that the wall adjacent cell center is always bigger than the roughness height. The wall shear stress τ_w and wall heat flux q_w can be found using two analytical expressions. These expressions can be found in Equations 2.55 and 2.56. The integration constants A_u and A_T are determined by applying boundary conditions and the details can be found in the appendix of Suga et al. [59]. At last the different equations for $\overline{P_k}$ and A_t can be found in the tables from Suga et al. [59]. Note that the momentum and Pr_t corrections can be applied in every cell, but they are only used in the wall adjacent cell due to numerical reasons.

$$\tau_w = (\mu + \mu_t)\frac{du}{dy} = \frac{\rho\sqrt{k_p}A_u}{\mu} \tag{2.55}$$

$$q_w = \left(\frac{\mu}{Pr} + \frac{\mu_t}{Pr_t}\right)\frac{du}{dy} = -\frac{\rho C_p\sqrt{k_p}A_T}{\mu} \tag{2.56}$$

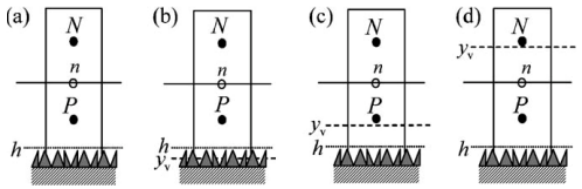

Figure 2.9: Near-wall cells over a rough wall: (a) $y_v \leqslant 0$, (b) $0 < y_v \leqslant h$, (c) $h < y_v \leqslant y_n$, (d) $y_n < y_v$ [59].

In the end, Suga et al. [59] concludes that the effects of wall roughness on the turbulence momentum and heat transfer are captured by using an analytical wall function. The analytical wall function used the equivalent sand grain roughness for the non-dimensional thickness of the modelled viscous sub-layer and the turbulent Prandtl number at the wall adjacent cell. They further conclude that the analytical wall function was applied successfully both for attached and separated flows. Even though the conventional log-laws are included in the wall function, it was able to reproduce the velocity and temperature log profiles without grid dependency. At last they conclude that the computational cost required for the analytical wall function is of similar magnitude to that of the standard log-law wall-function for smooths walls. In Figure 2.10 the results for the Stanton number for a flow over a flat plate can be seen, showing agreement with experiments.

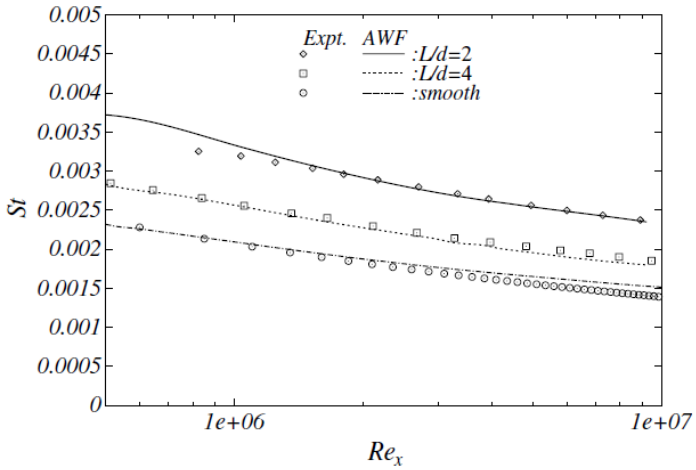

Figure 2.10: Stanton number distribution for flow over a flat plate with different roughness ($Pr = 0.71$). Figure from Suga et al. [59]

2.4.5. Prandtl corrections for LRN approaches

Besides the use of wall functions, it is also possible to correct the turbulent Prandtl number in the whole computational domain in a fine mesh. In this approach, the roughness itself is not modelled in the mesh and the cells are smaller than the roughness elements. To capture the effect roughness on heat transfer, the turbulent Prandtl number can be modified to better predict the thermal transport. Aupoix [5] used this method.

Aupoix [5] used RANS simulations on a very fine grid, $\Delta y^+ = 0.01$ for the wall adjacent cell, with an expansion rate of 1.05, to generate a large database to investigate the thermal roughness effects. With that database he made a thermal correction and processed the corrections in a model. It must be noted that the database was made with only artificial roughness, so his results may not be suitable for random roughness. It was found that besides the equivalent sand grain height, another parameter can be introduced to better describe the thermal effects due to roughness. This other parameter is the wetted corrected surface ratio S_{corr}, or corrected surface in short. The corrected surface can be calculated as follows: first the height must be calculated if the whole surface would be melted down. With this melt down height, the surface is modified so all of the roughness elements below this height are neglected. The total area of this new surface must be calculated and divided by the area of the

surface if the surface would be a smooth wall. A full explanation can be found in Olazabal-Loumé et al. [61] with a clear example.
Because it is assumed the turbulent viscosity has already changed to predict the right wall shear stress, the only way to improve the heat transfer prediction is by changing the turbulent Prandtl number. When the turbulent Prandtl number increases, the heat diffusivity becomes smaller compared to the turbulent diffusivity. Therefore, a correction has been found in the form of Equation 2.57 in which Pr stands for the Prandtl number. $Pr_{t,smooth}$ has been taken as 0.89.

$$Pr_t = Pr_{t,smooth} + \Delta Pr_{t,rough} \tag{2.57}$$

Aupoix [5] stated that the Prandtl correction, $\Delta Pr_{t,rough}$, should capture the dynamic roughness effects as well as the increased surface area. The Prandtl correction should also be restricted to the wall region because the effect of the wall roughness becomes smaller and ultimately disappears away from the wall. Therefore, the Prandtl correction was split in two parts: $\mathcal{F}$ and $\mathcal{G}$ in which $\mathcal{F}$ captures the roughness effects and increased surface area and $\mathcal{G}$ is a damping function which restricts the correction to the wall region. This resulted in Equation 2.58.

$$\Delta \mathcal{P}_{t,rough} = \mathcal{F}\left(\Delta u^+, S_{corr}\right) \mathcal{G}\left(\frac{y}{h}\right) \tag{2.58}$$

Before determining $\mathcal{F}$, $\mathcal{G}$ was tuned to have "nice" forms of $\mathcal{F}$. This led to the short equation for $\mathcal{G}$ in which y is the height of the cell and h the roughness height:

$$\mathcal{G}\left(\frac{y}{h}\right) = \exp\left(-\frac{y}{h}\right) \tag{2.59}$$

To determine $\mathcal{F}$, the required $\mathcal{F}$ value was plotted against the observed velocity shift Δu^+. It was found that the profiles looked parabolic and therefore a function in the form of Equation 2.60 has been looked for.

$$\mathcal{F} = A\Delta u^{+2} + B\Delta u^+ \tag{2.60}$$

In this equation are A and B coefficients depending on the earlier mentioned wetted corrected surface ratio. The equations for the coefficients have been determined and can be found in Equations 2.61 and 2.62.

$$A = \left(0.0155 - 0.0035 S_{corr}\right)\left(1 - \exp\left[-12\left(S_{corr} - 1\right)\right]\right) \tag{2.61}$$

$$B = -0.08 + 0.25 \exp\left[-10\left(S_{corr} - 1\right)\right] \tag{2.62}$$

The full equation for the turbulent Prandtl number can be seen in Equation 2.63, with the same values for A and B.

$$\mathcal{P}_t = \mathcal{P}_{t,smooth} + \left(A\Delta u^{+2} + B\Delta u^+\right) \exp\left(-\frac{y}{h}\right) \tag{2.63}$$

The model requires in total three input parameters: the roughness element height h (for determining the damping), the equivalent sand grain height k_s (to determine the velocity shift Δu^+, which must be determined by another equation or model), and the corrected wetted surface ratio S_{corr}. In the validation of this model, the equation from Grigson [62] is used to determine the velocity shift. Grigson [62] constructed this equation to match the data from Colebrook [25]. It has to be noted that this data is only valid for fully rough regimes, so the prediction for the velocity shift for the transitionally rough region might not be predicted accurately.
Aupoix validated the model by comparing his results with a variety of experiments such as roughness due to icing, Figure 2.11, and a flat plate with roughness elements made by spheres, see Figure 2.12. He concluded his paper by mentioning that his model increased the accuracy of thermal transport over rough surfaces even though the coefficients do not fill all of the database data. He also mentioned a weak point of the model, which is the need for the evaluation of the wetted corrected surface ratio. For artificial roughness, this value can be analytically calculated, but for real and random roughness the evaluation can become a problem. A point of improvement of the model can be the determination

of the coefficients because only computational results are used to come up with the model and not experimental studies as well.

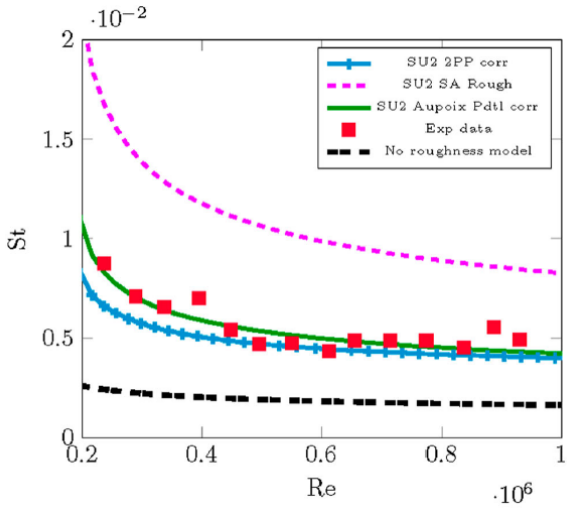

Figure 2.11: Stanton number distribution simulations compared with an experiment from Dukhan et al. [63]. Also the results from the model which is discussed next are included. Figure from Morency and Beaugendre [64].

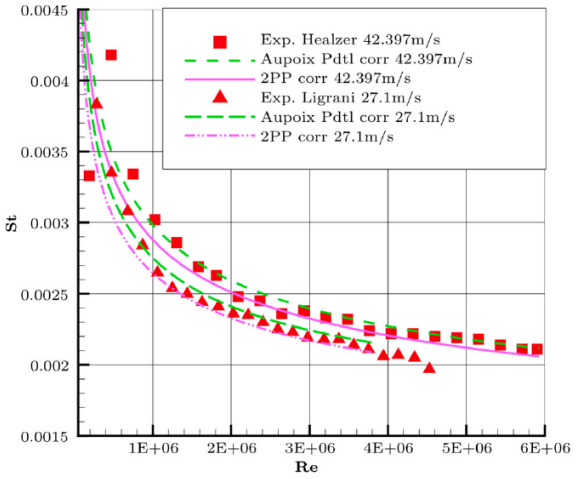

Figure 2.12: Stanton number distribution simulations compared with an experiment from Healzer et al. [65] and Ligrani [66]. Also the results from the model which is discussed next are included. Figure from Morency and Beaugendre [64].

Besides Aupoix [5], Morency & Beaugendre [64] also made a LRN model to increase accuracy of the prediction of heat transfer over rough surfaces. This paper was motivated by the urge to improve in-flight ice accretion on airplane wings. Also like Aupoix [5], the authors acknowledged the need for more than a single parameter than just the equivalent sand grain height. They shortly discuss findings from Dipprey and Sabersky [35] and Kays and Crawford [34] that the inverse of the sublayer Stanton number can be used to shift the temperature profile near the wall. Even though it is a LRN model, it is assumed that the flow is averaged over the roughness elements. Therefore it is not necessary to make a mesh which follows the roughness and to discretise and solve the flow equations around each element. Their goal was to derive and implement a two parameter model based on the thermal correction model of Dipprey and Sabersky [35].
Without a thermal correction, the heat transfer is over predicted when roughness is involved. Morency & Beaugendre [64] mentioned there are two possibilities to decrease this over prediction. The first being modifying the effective thermal conductivity k_e and the second the modification of the effective turbulent Prandtl number. They chose the second, so the same principles as in Aupoix [5] concerning the increase in turbulent Prandtl number have been used. They state that the modification of the turbulent Prandtl number Pr_t should be a smooth function in which the maximum value is at the wall. A schematic overview of the roughness elements at the wall with the assumed turbulent Prandtl number can be found in Figure 2.13.

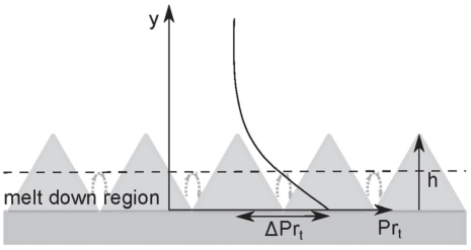

Figure 2.13: Turbulent Prandtl number evolution above a rough wall. Also the meltdown height is shown, discussed earlier, and circulating eddies trapped within the roughness elements. Also note the difference between the roughness height h and equivalent sand grain height k_s. Figure used from Morency & Beaugendre [64].

They further mention that for a turbulent flow over a smooth wall, it is generally assumed that the turbulent Prandtl number is 0.9 and the turbulent viscosity 0 at the wall. However, because in the case of the rough Spalart & Allmaras model from Aupoix and Spalart [50] $\mu_t > 0$, the ΔPr_t function does not change the turbulence model and so the values of ΔPr_t are computed for each time step after the turbulence equations are solved.
In the Spalart-Allmaras turbulence model, the friction velocity has been tuned such that it is related to $\tilde{\nu}$ and the corrected rough wall distance $d + 0.03k_s$ [50]. The relation can be found in Equation 2.64. This assumption is however only valid for the fully rough region and not for the transitionally rough region as well in which the predictions are less accurate. Even though, Morency & Beaugendre [64] used this assumption and mentioned that it gave good results.

$$u_\tau = \frac{\tilde{\nu}}{\kappa\left(d + 0.03k_s\right)} \tag{2.64}$$

The starting point of the Prandtl correction lies within experiments at Stanford which led to a model based on an increase in the rough wall temperature by a value δT_0 [66]. The temperature shift is normalised by the friction temperature $T_\tau = \frac{-q_w}{\rho c_p u_\tau}$ to become:

$$\delta T_0^+ = \frac{\delta T_0 \rho c_p u_\tau}{q_w} \tag{2.65}$$

After stating from Kays and Crawford [34] that in the logarithmic region of a rough boundary layer $\frac{\nu_t}{\nu} = \kappa(y^+ + 0.031k_s^+)$, assuming the viscous sub layer y_v^+ is much smaller than $0.031k_s^+$ and only molecular effects account for the thermal transport in the viscous sub layer, the temperature in wall units can be expressed as in Equation 2.66.

$$T^+ = \frac{Pr_t}{\kappa} \ln\left(\frac{y^+ + 0.031k_s^+}{0.031k_s^+}\right) + \delta T_0^+ \tag{2.66}$$

The expression found by Dipprey and Sabersky [35] and Owen and Thomson [36] was used to compute the value of δT_0^+, which is:

$$\delta T_0^+ = \frac{{k_s^+}^\alpha Pr^\beta}{C} \tag{2.67}$$

In this equation, C, α and β are constants. Different sources uses different values. Morency and Beaugendre [64] used the values according to Radenac [67] because they are used the most in icing codes. These values are $C = 1.92$, $\alpha = 0.45$ and $\beta = 0.8$. Because the previous equation is only valid for the fully rough region, Ligrani, Moffat and Kays [66] suggested that the expressions should be multiplied with a damping parameter g. The expression for this value is dependent on the regime and is a function of the roughness Reynolds number k_s^+. The expressions can be found in Equation 2.68.

$$g = \begin{cases} 1, & \text{if } k_s^+ \geq 70 \\ \frac{\ln k_s^+ - \ln 5}{\ln 70 - \ln 5}, & \text{if } 5 < k_s^+ < 70 \\ 0, & \text{if } k_s^+ \leq 5 \end{cases} \tag{2.68}$$

It appeared that the combined equations of δT_0^+ are equivalent to the corrected turbulent Prandtl number. The equations for δT_0^+ were rewritten to Equation 2.69 with F being equivalent to the $\mathcal{F}$ in Equation 2.58 from Aupoix. The damping function $\mathcal{G}$ is used from Aupoix [5]. The equation for F can be found in Equation 2.70.

$$\delta T_0^+ \approx \frac{3.02}{\kappa} F \tag{2.69}$$

$$F = 0.136 \frac{g {k_s^+}^\alpha Pr^\beta}{C} \tag{2.70}$$

With the final form of the thermal correction, the model was compared with the thermal correction of Aupoix [5] and experimental data. The model was validated for the following cases: a flat plate with ice accretion, a swept wing with roughness at the first 15% of the leading edge and an iced airfoil.

They concluded that the difference between Aupoix [5] and their model was within typical experimental uncertainties, see Figures 2.11 and 2.12.
Furthermore, no pro's or cons are discussed about this model compared to the model from Aupoix [5]. One property, which can both be a strength and a weakness of the model, is the simplicity of the input parameter. Only the roughness Reynolds number, which is the same as equivalent sand grain roughness in wall units, and the Prandtl number are necessary. This can be a benefit, because less information from the rough surface is required, but it can also be a downside because every surface affects the heat transfer differently due to the fact that the physics differ from the momentum transfer, on which is the equivalent sand grain height is based off.
To further study the difference between the two thermal correction models discussed in this section, Ignatowicz, Morency & Beaugendre [68] performed a study on the influence of the input parameters. So the models from Aupoix [5] and from Morency & Beaugendre [64] (2PP) were compared. The study was focused on the ice accretion on an airfoil. It appeared that the predicted ice maximum thickness is sensitive to the choice of the thermal correction model and its parameters. The difference was about 20% for the convective heat transfer coefficient. In addition, the model from Aupoix showed a larger standard deviation compared to the 2PP model. It was also concluded that the most influential parameter for the Aupoix model is S_{corr} (75%) and for the 2PP model the roughness height k (90%).

2.4.6. Combining both methods

The two previously mentioned thermal correction models predict the heat transfer more accurately compared to older methods. A downside of these models is however the need for fine meshes at the wall, as it is a low Reynolds number approach [69]. For industrial applications, the extra computational costs might not be worth it. Therefore, the earlier mentioned wall function can be a solution. Chedevergne [69], saw the opportunity for an improvement in the analytical wall function from Suga et al. [59]. Because the heat transfer is a combined effect of an increase of near wall turbulence and an increase of surface area, both mechanisms should be taken into account according to his paper. Suga et al. [59] only takes into account the increase in turbulence levels and not the increase in surface area. The model from Aupoix [5] is not a wall function, but it takes into account the increase in surface area due to roughness. Therefore Chedevergne combined the two models into one to benefit from both the increased computational speed of a wall function and the improved accuracy due to the implementation of the increase in surface area. Therefore, Chedevergne said, the applicability of Suga's model is extended. In this section, the combined model of Suga and Aupoix by Chedevergne is summarized and explained.
With the idea from Aupoix to use a wall shift y_0, a new model for the rough viscous sub layer height $y^*_{v_r}$ has been made. With the use of Reichardt's law (see Equation 2.71, which is the velocity for a smooth wall) [70] and $\mu_t^+ = \left(\frac{\partial u^+}{\partial y^+}\right)^{-1} - 1$, the turbulent viscosity has been computed.

$$u_s^+ = \frac{1}{\kappa}\ln\left(1+\kappa y^+\right) + 7.8\left[1 - \exp\left(-\frac{y^+}{11}\right) - \left(\frac{y^+}{11}\right)\exp\left(-0.33y^+\right)\right] \tag{2.71}$$

Using $y^*_{v_r} = -\frac{\mu^+_{t,w}}{\alpha}$ several values for $y^*_{v,r}$ have been computed. The obtained curve has been fitted with Equation 2.72 to obtain an equation for the rough viscous sub layer height.

$$\begin{aligned}
y^*_{v_r} &= -\frac{1}{\alpha} f_1\left(h_s^+\right) f_2\left(h_s^+\right) f_3\left(h_s^+\right) f_4\left(h_s^+\right) + y^*_v \exp\left(-2h_s^+\right) \\
f_1 &= \left(\frac{h_s^+}{180}\right)^{1.15} \\
f_2 &= \left[1 + 2\exp\left(-\left(\frac{h_s^+}{100}\right)^{0.9}\right)\right] \\
f_3 &= \left[1 - 0.4\exp\left(-\left(\frac{h_s^+}{100}\right)^{1.2}\right)\right] \\
f_4 &= \left(1 + \ln\left(h_s^{+-0.9}\right)\right)\exp\left(-\frac{h_s^+}{7}\right)
\end{aligned} \tag{2.72}$$

Because of the wall shift y_0^+ in the model from Chedevergne [69], the averaged production term $\overline{P_k}$ and the averaged dissipation rate $\bar{\epsilon}$ have been modified. For $\overline{P_k}$, the lower limit of the integration has been changed from y_v to $y_{v,r}$. For the dissipation rate the new equations become:

$$\bar{\epsilon} = \begin{cases} \frac{2k_p^2}{\nu y_\epsilon^{*2}}, & \text{if } y_n^* < y_\epsilon^* \\ \frac{k_p^2}{\nu\left(y_n^* - y_0^*\right)} \left[\frac{2(y_\epsilon^* - y_0^*)}{y_\epsilon^{*2}} + \frac{1}{c_l} \ln\left(\frac{y_n^*}{y_\epsilon^*}\right)\right], & \text{if } y_n^* \geq y_\epsilon^* \geq y_0^* \\ \frac{k_p^2}{\left(y_n^* - y_0^*\right)} \ln\left(\frac{y_n^*}{y_0^*}\right), & \text{if } y_n^* \geq y_0^* \geq y_\epsilon^* \end{cases} \tag{2.73}$$

To compare the model from Chedevergne [69] with the model from Aupoix [5], Chedevergne [69] used the $k-\omega$ SST model. Therefore, he expressed the dissipation term in the k-equation as $\bar{\epsilon} = \overline{\omega} C_{mu} k_p$. He further modified the damping function $\mathcal{G}$ used in Aupoix [5] to ease integral calculations to be $\mathcal{G} = \max\left(0, 1 - \frac{y^*}{a h_s^*}\right)$. In this equation, $a = 1.3h/h_s$. Chedevergne [69] says in his paper that now three parameters are included in the modified wall function from Suga et al. [59], which only used one parameter (h_s^*).
The model from Chedevergne [69] is implemented and validated. Due to the code he used, the definition of y_n has been changed. y_n is no longer the north (or top) side of the cell but it is the location of the cell center.
In the validation, several cases had large h_s^+ values. In some of these cases, the equivalent sand grain height was bigger than the wall adjacent cell. In those cases, the wall function is not able to capture the complete effect on the heat transfer. Therefore, in all the cells above the wall adjacent cells, the model from Aupoix [5] was applied. Chedevergne [69] also noted that all the validation cases made use of prism layers in the unstructured mesh, which is common practice for such meshes. As a consequence, the wall adjacent cells are quad cells in 2D simulations.

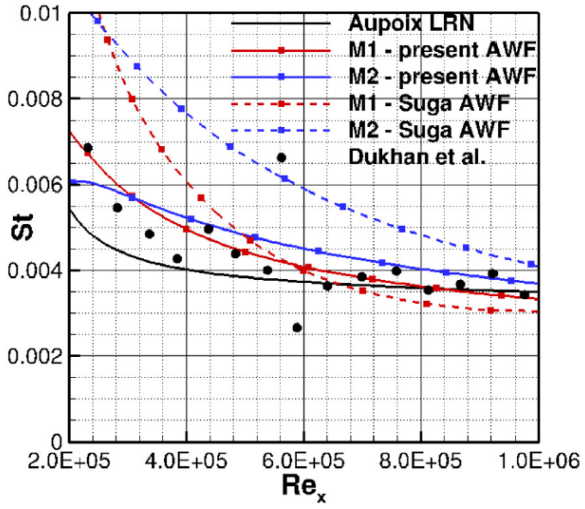

Figure 2.14: Stanton number distribution simulations compared with an experiment from Dukhan et al. [63], the AWF from Suga et al. [59] and the LRN model from Aupoix [5]. The model from Chedevergne is labeled present AWF. Note that the mesh size influenced the results. Figure from Chedevergne [69].

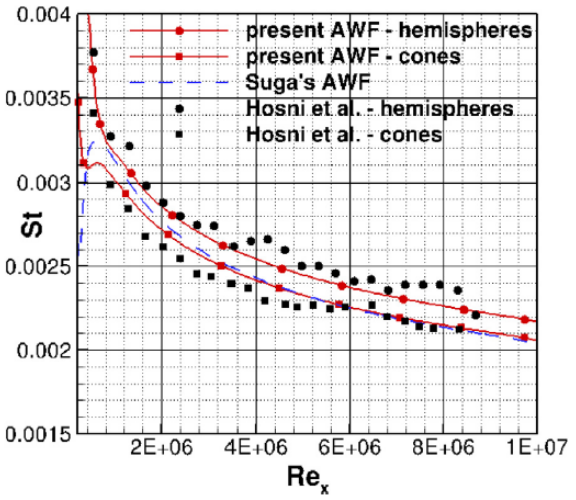

Figure 2.15: Stanton number distribution simulations compared with experiments from Hosni et al. [71]. Note the ability from the model from Chedevergne to distinguish between hemispheres and cones. Figure from Chedevergne [69].

The model has been compared with experiments from Hosni et al. [71] and Dukhan et al. [63]. Four different meshes have been made with a varying wall adjacent cell height to study the effect of the cell size on the results for the experiments from Hosni et al [71]. Also a fine mesh was been made corresponding to a LRN mesh with the model from Aupoix [5] applied in all cells. Chedevergne [69] concluded that the results for the coarse meshes need a certain distance before the skin friction and Stanton number distributions are recovered but after a while the difference between the new wall function and the wall function from Suga et al. [59] become small, irregardless of the mesh size used. See Figure 2.14. The most interesting results are however those which are compared with the experiments

of Dukhan et al. [63]. The model from Chedevergne [69] was able to better distinguish between the results from the hemispheres and cones compared to the model from Suga et al. [59]. The cases with hemispheres and cones had different wetted corrected surfaces, which is a property the newer model from Chedevergne took into account. Unfortunately, the results with the LRN model from Aupoix [5] were not shown in this graph, so they could not be compared. These results can be found in Figure 2.15.
In the end, Chedevergne [69] concluded that the results were also more accurate compared to the model from Suga et al. [59] due to the implementation of Aupoix's model [5] and the extra input parameter, the corrected wetted surface. A mentioned downside is that the results are still sensitive depending on the mesh size, which is not desired for wall functions.

2.5. Conclusion

After doing a literature research about roughness and its effect on heat transfer, it can be concluded that the Reynolds analogy fails. Heat transfer is over predicted for both the transitionally and fully rough regimes. To increase the accuracy of heat transfer simulations, several models for both LRN and HRN meshes have been developed by various authors. This was achieved by either decreasing the turbulent thermal conductivity or increasing the turbulent Prandtl number. Each model has his own strengths and weaknesses. However, researchers agreed that a single input parameter to correct the heat transfer, the equivalent sand grain height k_s, is not enough to precisely predict the influence of the roughness on the heat transfer. This was also recognized in the correction model from Aupoix [5]. This model, which increases the turbulent Prandtl number close to the wall, introduced the corrected wetted surface to implement the effect of an increased surface area. Unfortunately, the model was designed for a LRN mesh, which conflicts with industrial applications which require a model for HRN meshes. The model from Chedevergne [69] can be applied on a HRN mesh, but it was showed that the results were dependent on the mesh size. It is however unclear how the model from Aupoix [5] performs on a HRN mesh and if it fails, if it can be modified in a certain way that it can be used nonetheless on a HRN mesh and even reduce the dependency of the mesh size compared to the model from Chedevergne [69].

3

OpenFOAM

The open source software OpenFOAM was used to perform simulations. In this chapter a brief explanation of the software and governing equations is given.

3.1. Overview

OpenFOAM is an open source toolbox for numerical solvers, among which Computational Fluid Dynamics is the most important. OpenFOAM provides the same tools for CFD simulations as most commercial software packages such as Simcenter STAR-CCM+ and Ansys Fluent. This includes pre-processing tools for mesh generation, solvers for different flow problems and post-processing tools to present the results. An overview of the OpenFOAM structure can be seen in Figure 3.1. The version used in this thesis was version 9.

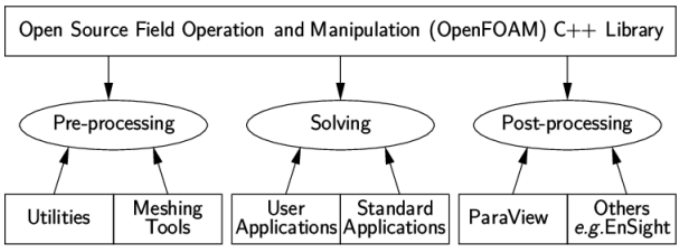

Figure 3.1: Overview of OpenFOAM structure. Figure from OpenFOAM User Guide [72].

OpenFOAM runs on a Linux environment. Simulations are run using a case folder structure, meaning each case has its own folder. In this folder the case set up, results and post-processing files are stored. The case folder always contains at least three sub-folders named: `0`, `constant` and `system`. In the `0` folder, the boundary conditions and initial values for all flow parameters are prescribed. The `constant` folder contains all simulation constants such as the mesh in the `polymesh` folder and fluid properties in `thermophysicalProperties`. All dictionaries are stored in the `system` folder. `controlDict` is used to define simulation parameters such as the simulation time and time step (for time dependent simulations) or the maximum number iterations (for steady state simulations). `blockMeshDict` is used to define the mesh geometry. `fvSchemes` and `fvSolution` contain the discretization schemes and solution algorithms, respectively. At last, for every defined time step (or number of iterations), results are stored in a folder corresponding to their time. After completion of a simulation and running `postProcess`, a new folder `postProcessing` is created where the post processed results are stored. This folder structure can be seen in 3.2.

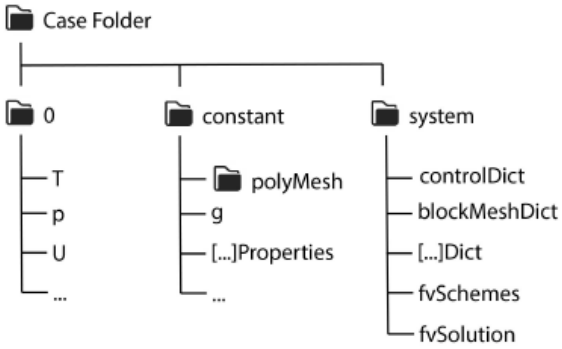

Figure 3.2: OpenFOAM case folder structure. Figure from Habiyaremye [73].

OpenFOAM is popular due to multiple reasons. Because the software is free to use, users do not have to spend money in contrast to commercial packages. Another reason is the possibility to read the code. Therefore, solvers and other parts of the code can be verified by the user. The last reason is that users can implement their own CFD models and modify the code for their own purposes, which has been done in this thesis as well.
A downside of the software is the steep learning curve. To get familiar with OpenFOAM more time has to be spend compared to working with commercial packages. The reason is twofold. First no GUI is included in the software. Therefore the user is required to modify case files themselves instead of using the mouse button to set up a simulation and receiving immediate visual feedback. The second reason is the lack of 'protection' algorithms. Whilst commercial packages include pieces of code to improve convergence and troubleshooting, OpenFOAM uses a lot less to not restrict the user. Therefore more knowledge is required to run a simulation and interpret the results correctly.

3.2. Solvers

For all simulations in this thesis it is assumed that the density is constant and the pressure can not be obtained by an equation of state, i.e. $p = f(\rho, T)$ [74]. To cope with this problem, different algorithms have been developed.
In this thesis the solvers `buoyantPimpleFoam` and `buoyantSimpleFoam` are used. `buoyantPimpleFoam` is used in Chapter 4 and 5. `buoyantSimpleFoam` is used in Chapter 6. `buoyantPimpleFoam` is the transient version of the steady state `buoyantSimpleFoam` solver. `buoyantPimpleFoam` and `buoyantSimpleFoam` are based on the PIMPLE and SIMPLE algorithms, explained in Versteeg and Malalasekra [74], with the addition of the energy equation. The PIMPLE solver is a combination of SIMPLE and PISO to solve for transient simulations and improve stability. In the next sections, the different solvers are explained briefly.

3.2.1. SIMPLE

The SIMPLE algorithm calculates the pressure of steady state problems on a staggered grid. It is based on guessing and correcting the pressure field until the solution has converged. The SIMPLE algorithm goes through the following steps [74]:

- First, a pressure field p^* is guessed.
- Using this guessed pressure field, the momentum equations are solved and this gives the velocity components u^*, v^* and w^* for three-dimensional flow.
- Velocity and pressure corrections u', v', w' and p' are defined as follows:

$$u' = u - u^*, \quad v' = v - v^*, \quad w' = w - w^*, \quad p' = p - p^* \tag{3.1}$$

  in which, u, v, w and p are the real velocities and pressure.
- A momentum correction is created based on the pressure correction p' only and not on the velocity corrections in neighboring cells. This is an approximation made in the SIMPLE algorithm [74].

- In order to ensure that the corrected velocity field also satisfies the continuity equation, the continuity imbalance source term b' is added. Solving gives the pressure correction field p', which is then used to obtain a new guessed pressure field.
- For `buoyantSimpleFoam`, now the energy equation and turbulent transport equations are solved.
- The solver goes back to step 2 until convergence is reached.

3.2.2. PISO

The PISO algorithm is used as a non-iterative computation method to calculate the pressure and velocity fields in unsteady flows. It can be considered as an extension to the SIMPLE algorithm with an additional correction step [74].

- The algorithm starts in the same way as the SIMPLE algorithm by guessing a pressure field and solving for the guessed velocity field.
- The correction step of the SIMPLE algorithm is used to obtain a pressure correction field p'. In the PISO algorithm a second correction step will follow. This results in an once corrected pressure and velocity:

$$p^{**} = p^* + p', \quad u^{**} = u^* + u', \quad v^{**} = v^* + v', \quad w^{**} = w^* + w' \tag{3.2}$$

- Next, a second correct step will be made. The second pressure correction p'' and the twice corrected pressure p^{***} are then defined as:

$$p^{***} = p^{**} + p' + p'' \tag{3.3}$$

- It is then assumed that p^{***} and the twice corrected velocity fields are then the correct pressure and velocity and the solver moves on to the next time step.

3.2.3. PIMPLE

The PIMPLE algorithm combines the PISO and the SIMPLE algorithms to solve transient flow problems. Within each time step, the steps of the PISO algorithm are followed to give an initial solution for a certain time step. For a pre-defined number of outer corrector loops, the solution of the PISO algorithm is used as the initial guess of the outer corrector loop. When this outer corrector loop is completed using the SIMPLE algorithm, the solution is considered as final and the PIMPLE algorithm moves on to the next time step.
For stability and preventing divergence of the solution, under relaxation can be used when correcting the pressure and velocity. The final corrector should however not be under relaxed to ensure that the final solution of each time step satisfies the continuity equation [74]. In Chapter 4 and 5 no relaxation factors have been used. In Chapter 6 they were set to 0.5, 0.35, 0.45, 0.4 and 0.4 for p_{rgh}, U, h, k and ϵ respectively.

3.3. Governing Equations

The equations for `buoyantSimpleFoam` are equal to `buoyantPimpleFoam` but without the $\partial/\partial t$ terms. Only the equations for `buoyantPimpleFoam` will be shown.
The momentum equation can be seen in Equation 3.4 [75]. In this equation, $-\nabla p + \rho \boldsymbol{g}$ is rewritten as in Equation 3.5 in which **r** is the position vector. In this equation, p_{rgh} is the pressure minus the hydro static pressure. For the simulations done in this thesis, g is set to zero and therefore the term $-\nabla p + \rho \boldsymbol{g}$ in Equation 3.4 reduces to $-\nabla p_{rgh}$. Furthermore, in Equation 3.4 is μ_{eff} the effective dynamic viscosity, Tr the trace and I the identity matrix.

$$\frac{\partial \rho \mathbf{u}}{\partial t} + \nabla \cdot (\rho \mathbf{u}\mathbf{u}) = -\nabla P + \rho g + \nabla \cdot \left(\mu_{eff} \left(\nabla \mathbf{u} \right)^T - \frac{2}{3} \mu_{eff} \, \mathrm{Tr} \left(\nabla \mathbf{u} \right)^T \boldsymbol{I} \right) + \nabla \cdot \left(\mu_{eff} \nabla \mathbf{u} \right) \tag{3.4}$$

$$\begin{aligned} -\nabla p + \rho \boldsymbol{g} &= -\nabla \left(p_{rgh} + \rho \boldsymbol{g} \cdot \mathbf{r} \right) + \rho \boldsymbol{g} \\ &= -\nabla p_{rgh} - (\boldsymbol{g} \cdot \mathbf{r}) \nabla \rho - \rho \boldsymbol{g} + \rho \boldsymbol{g} \\ &= -\nabla p_{rgh} - (\boldsymbol{g} \cdot \mathbf{r}) \nabla \rho \end{aligned} \tag{3.5}$$

For the energy equation, the user can either solve for the internal energy e or enthalpy h. In this thesis the enthalpy has been used. The full equation can be seen in Equation 3.6 [75]. In this equation $K \equiv |\mathbf{u}|^2/2$ is the kinetic energy per unit mass. The enthalpy per unit mass is defined as the sum of the internal energy per unit mass and the kinematic pressure, so $h \equiv e + p/\rho$. Furthermore, κ_{eff} is the effective thermal conductivity and S is a source term.

$$\frac{\partial \rho h}{\partial t} + \nabla \cdot (\rho \mathbf{u} h) + \frac{\partial \rho K}{\partial t} + \nabla \cdot (\rho \mathbf{u} K) - \frac{\partial p}{\partial t} = \nabla \cdot (\kappa_{eff} \nabla h) + \rho u \cdot g + S \tag{3.6}$$

Because $\partial \rho K/\partial t$ and $\partial p/\partial t$ are practically 0 and gravity is neglected, these terms are dropped out of the equation. Fluid properties are kept constant and so Equation 3.6 reduces to:

$$\rho \frac{\partial h}{\partial t} + \rho \nabla \cdot (\mathbf{u} h) + \rho \nabla \cdot (\mathbf{u} K) = \kappa_{eff} \nabla \cdot (\nabla h) + S \tag{3.7}$$

3.4. Discretization schemes

For solving the equations, the Gauss divergence theorem is used (Equation 3.8). The theorem relates the divergence of a volume to the flux over the surface enclosing that volume. In other words, it relates the change of a quantity in a volume by what comes in and out through the surface.

$$\iiint_V \nabla \cdot \mathbf{F} dV = \iint_s \mathbf{F} \cdot \hat{n} dS \tag{3.8}$$

In OpenFOAM both scalar and velocity variables are stored at the cell center. To apply the Gauss divergence theorem, values are needed at cell faces. These values are obtained using interpolation schemes and in this thesis multiple discretization schemes have been used. In Chapter 4 and 5, `Gauss linearUpwind grad(U)` has been used for the divergence scheme of the velocity. For the other terms, `Gauss limitedLinear 1` has been used. For the $\partial/\partial t$ terms, the `Euler` scheme has been used and for the gradient schemes `Gauss linear`. In Chapter 6, the time t and divergence schemes were changed. For t, no scheme was used because the simulation was steady state. For the divergence schemes `Gauss upwind` has been used to improve stability.

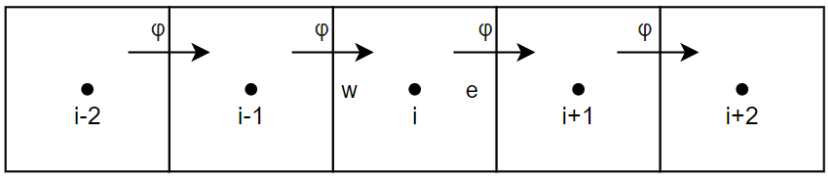

Figure 3.3: 1D grid finite volume example

To compute the flux ϕ at a cell face, the value at the up stream cell node is used in the upwind scheme. Using Figure 3.3 as an example, ϕ_w = ϕ_{i-1} and $\phi_e = \phi_i$. This method is first order accurate. For the linear scheme, which is second order accurate, phi at a cell face is calculated using the values at the adjacent cell centers, see Equation 3.9. The gradient of ϕ at point i is computed using Equation 3.10. Substituting $(x_{i+1} - x_i)$ = $2(x_e - x_i)$ for an equilateral mesh, so Equation 3.9 is simplified to Equation 3.11.

$$\phi_e = \phi_i + \left[\frac{\partial \phi}{\partial x}\right]_i (x_e - x_i) \tag{3.9}$$

$$\left[\frac{\partial \phi}{\partial x}\right]_i = \frac{\phi_{i+1} - \phi_i}{x_{i+1} - x_i} \tag{3.10}$$

$$\phi_e = \phi_i + \frac{1}{2}(\phi_{i+1} - \phi_i) \tag{3.11}$$

For the linear upwind scheme, the value at the face center is computed using the gradient of the up stream cell node. So instead of using Equation 3.10, Equation 3.12 is used to compute the gradient at

node i. Equation 3.9 is then simplified to Equation 3.13 using the same assumptions as for the linear scheme.

$$\left[\frac{\partial \phi}{\partial x}\right]_i = \frac{\phi_i - \phi_{i-1}}{x_i - x_{i-1}} \tag{3.12}$$

$$\phi_e = \phi_i + \frac{1}{2}\left(\phi_i - \phi_{i-1}\right) \tag{3.13}$$

When a limiter is used, a factor ψ appears in front of the gradient, resulting in Equation 3.14. In this equation, ψ is the limiter which is computed using Equation 3.15. k is the input parameter for `limitedLinear k` and r_i is the ratio of successive gradients which is computed using Equation 3.16.

$$\phi_e = \phi_i + \frac{1}{2}\psi\left(\phi_{i+1} - \phi_i\right) \tag{3.14}$$

$$\psi = \frac{2}{k} r_i \tag{3.15}$$

$$r_i = \frac{\phi_i - \phi_{i-1}}{\phi_{i+1} - \phi_i} \tag{3.16}$$

4

Validation

In this chapter it is explained how the model from Aupoix [5] is implemented in OpenFOAM and how it is validated using two different DNS data sets. Each data set used a different surface geometry and different values for Re_τ and k_s^+. The approach on how the cases have been set up is also explained, together with the explanation of the surface calculations.

4.1. Implementation

4.1.1. Momentum correction

The thermal correction model from Aupoix [5] relies on several input parameters. One of those inputs is the predicted shift in the velocity profile, Δu^+. To validate the model, it is therefore important to accurately predict the wall shear stress and roughness wall function. To account for wall roughness without actually resolving it, the wall function must be modified. This is achieved as follows: the wall shear stress has been predicted by setting `nutkRoughWallFunction` as a boundary condition for the turbulent viscosity at the wall, ν_w. This function modifies the value E in Equation 4.1 to E' in order to increase the viscosity at the wall. The shift in the velocity profile is calculated with the use of Equation 4.2 [29]. E' can then be calculated using Equation 4.3 [29].

$$\nu_w = \nu + \nu_t = \frac{y^+ \nu}{\frac{1}{\kappa} \ln (E y^+)} \tag{4.1}$$

$$\Delta u^+ = \begin{cases} 0, & \text{if } k_s^+ \leq 2.25 \\ \frac{1}{\kappa} \ln \left(\frac{k_s^+ - 2.25}{87.75} + C_s k_s^+ \right) \sin \left(0.4258 \ln (k_s^+) - 0.811 \right), & \text{if } 2.25 < k_s^+ \leq 90 \\ \frac{1}{\kappa} \ln (1 + C_s k_s^+), & \text{if } k_s^+ > 90 \end{cases} \tag{4.2}$$

$$E' = \frac{E}{e^{\kappa \Delta u^+}} \tag{4.3}$$

4.1.2. Thermal correction

Instead of modifying the thermal transport equations in OpenFoam, the same approach has been used analogous to the momentum correction. A new function `alphatRoughWallFunction` has been made to modify the thermal diffusivity α_t. This new function has been made from the original `alphatWallFunction` by adding ΔPr_t. The equations of the thermal correction model from Aupoix [5] as applied in the validation are summarized in Equations 4.4, 4.5, 4.6 and 4.7. $\mathcal{F}$ is the actual correction in which Δu^+ is computed using Equation 4.2 and S_{corr} is the corrected surface ratio which is a surface property and is calculated in advance. $\mathcal{G}$ is a damping function which makes sure the correction is only applied in the region near the wall. In these equations Δy^+ is the y^+ value of the wall adjacent cell center and k_s^+ the equivalent sand grain height of the roughness. In this new boundary function, the damping function decreases the calculated ΔPr_t number as function of the wall distance and roughness height, see Figure 4.1. The thermal correction model can in theory be applied on every turbulence model, i.e. $k - \epsilon$ and $k - \omega$.

$$Pr_t = Pr_{t,\infty} + \Delta Pr_{t,rough} \tag{4.4}$$

$$\Delta Pr_{t,rough} = \mathcal{F}\mathcal{G} \tag{4.5}$$

$$\mathcal{F} = (0.0155 - 0.0035 S_{corr}) \left(1 - e^{-12(S_{corr}-1)}\right) \Delta u^{+2} + \left(0.25 e^{-10(S_{corr}-1)} - 0.08\right) \Delta u^{+} \tag{4.6}$$

$$\mathcal{G} = e^{-\frac{\Delta y^+}{k_s^+}} \tag{4.7}$$

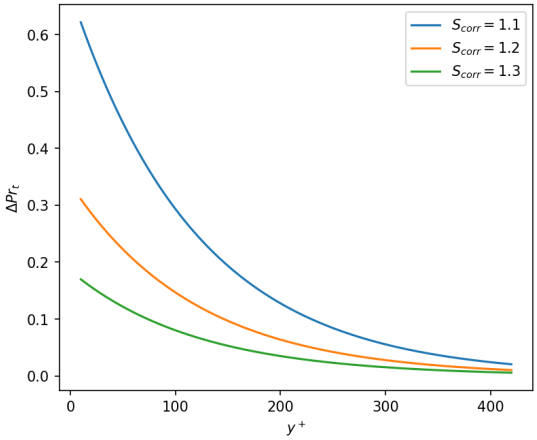

Figure 4.1: Calculated ΔPr_t as function of y^+ for several values of the corrected surface ratio. y^+ represents a certain mesh height of the wall adjacent cell and k_s^+ is equal to 120 for all plots.

4.2. Expectations

The wall distance is defined as the distance from the wall to the center of the wall adjacent cell. When looking at Equation 4.7, it can be seen that the calculated value of the damping function will be smaller with increasing cell size and thus the calculated ΔPr_t number will be smaller as well. However, the area in which the model is active is also larger with bigger cells, see Figure 4.2.

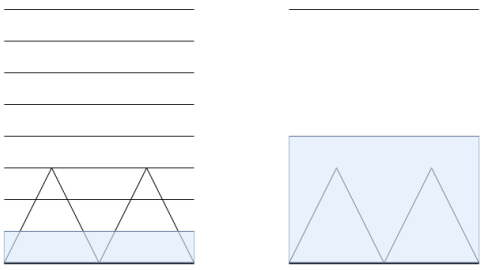

Figure 4.2: Schematic drawing of two different meshes with the same roughness elements. The thermal correction model is only applied in the wall adjacent cell, shown by the blue colored cell, resulting in a difference between the area in which the model is applied. On the left a smaller mesh is shown compared to the right mesh. Note that the roughness elements are not part of the mesh, but are shown as a reference.

As a consequence, it is expected that the influence on the results are dependent of the mesh size. It is expected that there is an equilibrium between the decreasing behaviour of the damping function and increasing behaviour of the area when the cell size increases. To make a first estimate where this equilibrium results in a maximum influence of the model, the calculated ΔPr_t has been multiplied with the cell size and plotted as a function of the wall distance. Multiplying ΔPr_t with Δy^+ shows a combined effect of the influence of the cell size on the area and corrected turbulent Prandtl number. The result can be seen in Figure 4.3. It is therefore estimated that the influence of the thermal correction

model reaches a maximum when the roughness height is equal to the mesh size. It is after all the goal of the model to avoid having to resolve the wall roughness and thus end up with a mesh with a large number of grid points. Therefore, relatively large cell sizes are expected and it will be shown that the results are indeed dependent on the mesh size.

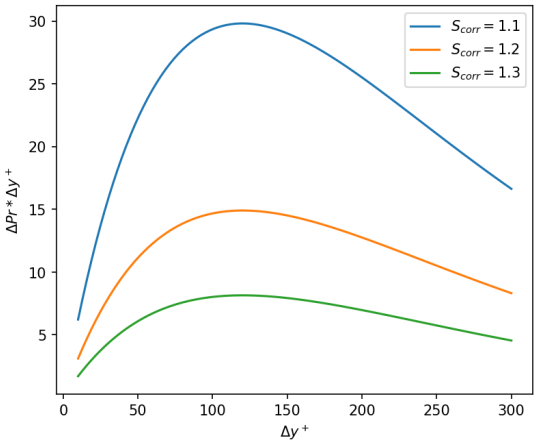

Figure 4.3: Calculated ΔPr times the cell height as function of Δy^+ for several values of the corrected surface. Δy^+ is equal to the mesh height of the wall adjacent cell and k_s^+ is equal to 120 for all plots.

4.3. General set-up

4.3.1. Geometry and boundary conditions

The geometry of the channel flow cases can be found in Figure 4.4. In this figure, L_x and L_y are the dimensions of the channel in the x- and y-direction. The boundary conditions of the in- and outlet of the channel are set to be cyclic. This means that what goes out the domain, enters the domain on the other side. Forcing a mean velocity ensures the flow does not stop due to friction at the walls. The temperature of the walls are kept constant at $300K$.

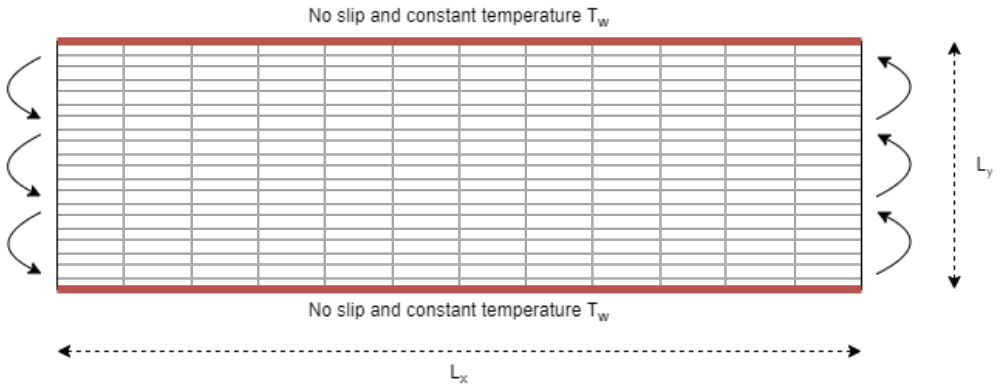

Figure 4.4: Schematic drawing of the channel flow geometry with the boundary conditions for the velocity and temperature.

To introduce heat transfer from the fluid to the walls, a heat source has been used by the reference papers. Peeters and Sandham [19] added a heat source, Q, to the transport equation for the temperature and due to the scaling of u_τ and T_τ, it was equal to unity. MacDonald et al. [46] split the temperature into a mean and periodic component and the mean component was applied as the source term: $Q = -udT/dx$. For the RANS validation cases, the heat source has been applied as a constant in every cell of the computational domain. It was expected that the solution in Θ^+ units would be independent of the applied heat source. To confirm this hypothesis, several values have been studied to see the effect on the results. In Figure 4.5 it can be seen that there is indeed no effect of the heat source on the results in Θ^+ units because all temperature profiles overlap. The heat source for the

RANS simulations has been set to $1 \times 10^4 W/m^3$.

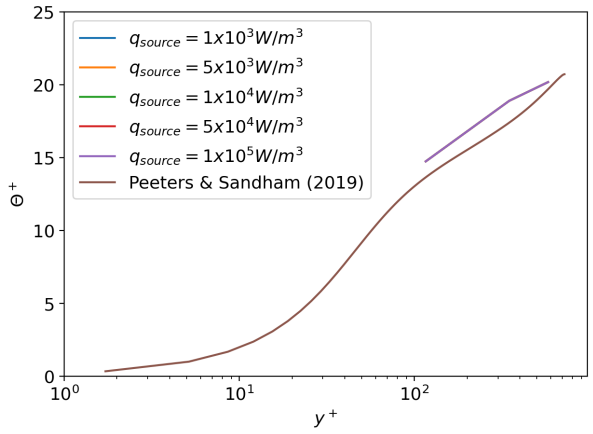

Figure 4.5: Influence on the temperature profile for different values of the heat source. No effect on the temperature profiles have been observed, so any heat source would give valid results. $Re_\tau = 720$ and $k^+ = 120$ for these simulations.

4.3.2. Surface calculations

One of the input parameters of the correction model is the corrected surface ratio S_{corr}. For the two validation cases, these values are determined according to Aupoix [52]. The surface areas have been calculated by generating data points in xyz coordinates across a rectangular grid. Every four points have been split into two triangles and the area of these triangles have been computed with the use of Heron's formula, which can be seen in Equation 4.8. In this equation, a, b and c are the lengths of each side of the triangle and s is the semi-perimeter, see Equation 4.9 and Figure 4.6. The lengths of each side are computed using Pythagoras: $length = \sqrt{(x_i - x_j)^2 + (y_i - y_j)^2 + (z_i - z_j)^2}$. Because distortion can occur by discretizing the surface geometry, the corrected surface ratio has been calculated at several grid sizes. In the following sections it will be shown that the computed value of the corrected surface ratio converged as function of the number of grid points. The determination of the corrected surface ratios has been done separately for each case and in advance of the CFD simulations.

$$A = \sqrt{s(s-a)(s-b)(s-c)} \tag{4.8}$$

$$s = \frac{a+b+c}{2} \tag{4.9}$$

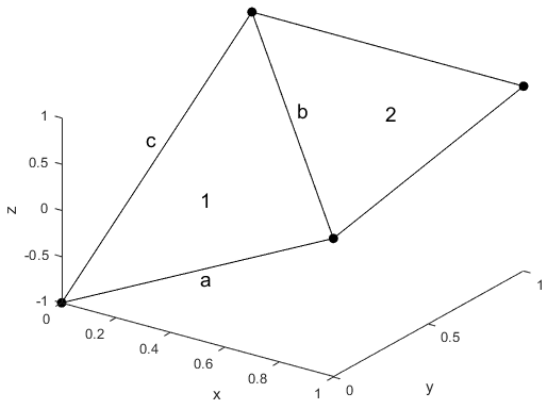

Figure 4.6: Example of approximating the area of a surface connected by four points using two triangles.

4.3.3. Turbulence model

Besides validating the thermal correction model, also the influence of the turbulence model has been studied. Because only when the momentum is predicted accurately, conclusions can be made about the thermal correction model. It was found that the velocity and temperature profiles for turbulent flows past a smooth wall were more accurate for the $k-\omega$ model compared to the $k-\epsilon$ model. However, when roughness was introduced, the $k-\omega$ model failed. This can be seen in the velocity shift profiles in Figure 4.7. The wall shear stress of the $k-\omega$ model was under predicted for the cases with roughness and hence it was not able to predict the velocity shift. The mesh was set in such a way that the Δy^+ value of the wall adjacent cell was equal to 45. This value has been chosen by maximizing the number of cells to increase accuracy, but also ensuring the restriction that the first cell center must lie within the log-layer.

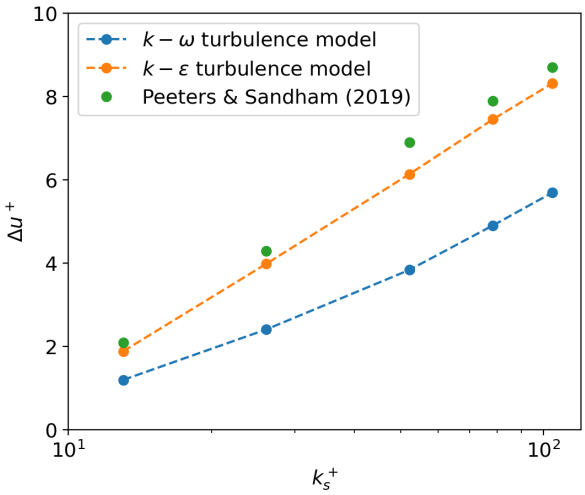

Figure 4.7: Velocity shift plot as function of the equivalent sand grain height. $\Delta y^+ = 45$ for both simulations.

4.4. Channel Flow with Irregular Roughness

4.4.1. Validation data

The validation data for the first test case comes from a DNS study by Peeters and Sandham [19]. In this paper, a cyclic channel flow with roughness on the upper and lower plates was studied. The roughness height k was set as a fraction of the channel half height δ. Therefore, k^+ was defined and k_s^+ was determined to be $k_s^+ \approx 0.87k^+$. The driving force was a pressure gradient Π and the friction velocity was defined by $u_\tau = \sqrt{-(\delta/\rho)\,\Pi}$. Using these definitions, it was convenient to set the friction Reynolds number, $Re_\tau = u_\tau \delta/\nu$, to a constant value. The friction Reynolds numbers and roughness heights were varied from 180 to 720 and 0 to 120 respectively. In this validation, the results from $Re_\tau = 180$ were not used because the mesh required for a High Reynolds Number mesh ($\Delta y^+ \gtrapprox 30$) is too coarse to extract any useful results. The simulated cases in the validation together with the corresponding bulk Reynolds numbers can be found in Table 4.1. In OpenFOAM it was more convenient to define a bulk Reynolds number and use it to force a mean velocity. The simulations however under-predicted the friction Reynolds number when the bulk Reynolds number of the paper was used. Therefore, the bulk Reynolds number was increased so $\frac{Re_{\tau,RANS} - Re_{\tau,paper}}{Re_{\tau,paper}} < 0.02$. These bulk Reynolds numbers are included in the table as well.

For every roughness height, the velocity and temperature profiles are compared to the corresponding case with the same friction Reynolds number without roughness. An average velocity and temperature shift has been calculated in the log-layer for every roughness height. These results can be found in Figure 4.8. It can be seen that the temperature shift is not equal to the velocity shift, even though the molecular Prandtl number is equal to 1.0. This indicates the failure of the Reynolds analogy. Furthermore, it can be seen in the temperature shift that when the roughness increases, the temperature shift profile starts leveling out. There are no results available for larger roughness heights in this paper. MacDonald et al. [46] also reported leveling out of the temperature shift and will be discussed in the

Table 4.1: Details of the DNS cases from Peeters and Sandham [19] which are used as reference data. Note the absence of the case with $Re_\tau = 180$ because the friction Reynolds number is too low to make a proper HRN mesh.

k^+	k/δ	Re_τ	$Re_{B,paper}$	$Re_{B,used}$
0	0	360	12.6×10^3	13.0×10^3
0	0	540	20.0×10^3	20.7×10^3
0	0	720	27.8×10^3	28.6×10^3
15	$1/24$	360	11.1×10^3	11.7×10^3
30	$1/12$	360	9.5×10^3	10.0×10^3
60	$1/6$	360	7.9×10^3	8.5×10^3
90	$1/6$	540	11.8×10^3	12.6×10^3
120	$1/6$	720	15.5×10^3	16.8×10^3

next section. The reason for leveling out of the temperature shift might be caused by heat transfer only occurring via conductive heat transfer within the roughness elements [34].

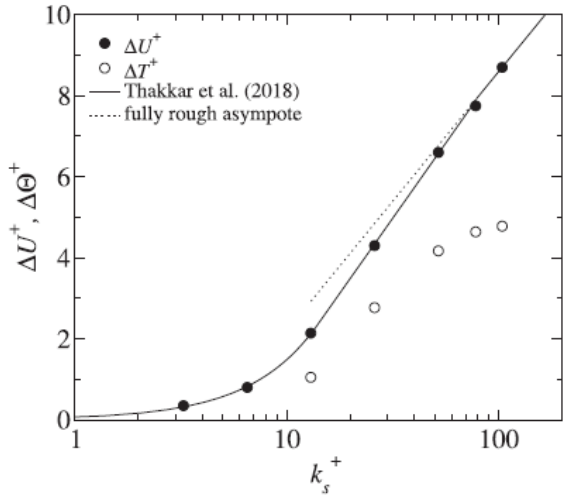

Figure 4.8: Velocity and temperature shift as function of the Reynolds roughness height k_s^+. Figure from Peeters and Sandham [19].

4.4.2. Case description

The rough surface Peeters and Sandham [19] used, is based on a surface scan by Busse et al. [18]. Their surface was grit-blasted and a filtered copy was stored using Fourier coefficients. With these coefficients and Equation 4.10, the surfaces could be reconstructed with varying grid sizes. In Equation 4.10, $h(x, z)$ is the height as function of x & z and λ_x & λ_z are the domain sizes which are equal to 5.63 and 2.815 respectively. The surface can be seen in Figure 4.9 and the minimum and maximum height are -0.1589 and 0.1031.

$$h(x,z) = \sum_{n=-24}^{n=24} \sum_{m=0}^{m=12} A_{n,m} \cos\left(\frac{2n\pi x}{\lambda_x} + \frac{2m\pi z}{\lambda_z}\right) + B_{n,m} \sin\left(\frac{2n\pi x}{\lambda_x} + \frac{2m\pi z}{\lambda_z}\right) \tag{4.10}$$

To calculate the corrected surface, the topology below the average height must not be taken into account (see also section 4.3.2). The average height is equal to 1.8×10^{-5}, which results in the surface seen in Figure 4.10. The calculated corrected surface ratio is 1.036. The convergence of this value as function of the number of grid points can be seen in Figure 4.11.

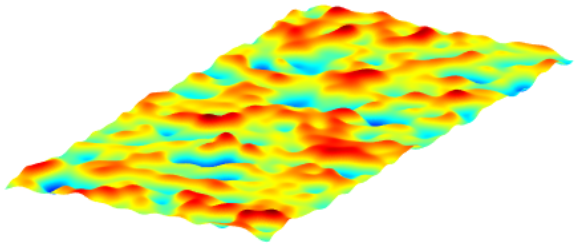

Figure 4.9: The filtered surface used for the DNS simulations and validation.

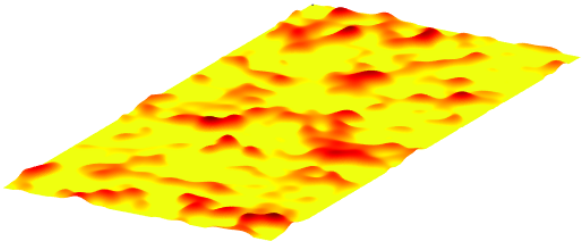

Figure 4.10: The corrected surface in which roughness below the meltdown height is neglected. The area of this surface is used to compute the corrected surface ratio.

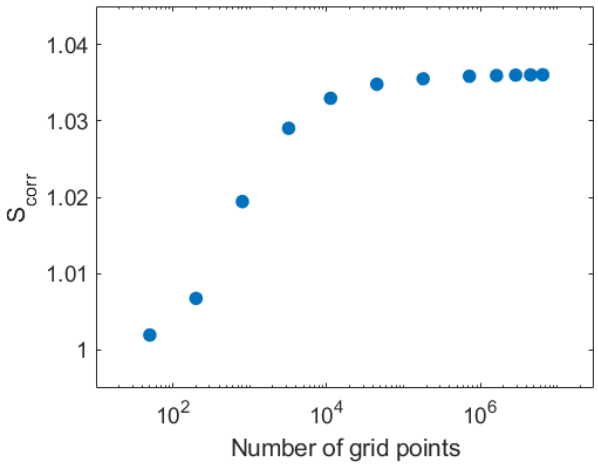

Figure 4.11: The calculated corrected surface as function of the number of grid points. It can be seen that the value converged to 1.036.

For the prediction of the velocity shift, it is important to obtain the correct k_s^+ from k^+ and the corresponding C_s value for Equation 4.2. For C_s a value of 0.253 has been chosen because this value is suggested by Cebeci and Bradshaw [29]. In Figure 4.12 it can be seen that $C_s = 0.253$ is indeed a valid assumption for this surface.

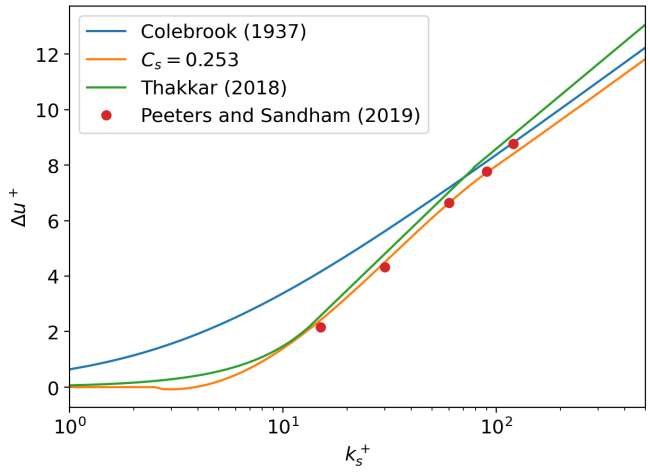

Figure 4.12: Δu^+ prediction according to Colebrook [25], Cebeci and Bradshaw [29] and Thakkar [76] as function of the equivalent sand grain height. The DNS results from Peeters and Sandham [19] are also shown.

4.4.3. Results

To see the effect of the mesh size on the results, multiple meshes have been made. For every mesh, the channel flow was simulated until steady state was reached for both the case with and without roughness. The velocity and temperature profiles of rough cases have been compared to those of the cases without roughness. For each mesh a temperature and velocity shift graph have been made by calculating the average shift in velocity and temperature profile for $y^+ > 30$. Concerning the choice of the mesh sizes, it is important to highlight the accompanying friction Reynolds numbers of the different simulations to the different roughness heights. For every graph in this section, the mesh size is defined by the roughness height k^+ divided by a number N. This makes sure that the mesh sizes are defined relative to the roughness height and therefore better comparable to each other. For an overview of the cases, N and accompanying Δy^+ of the wall adjacent cell, see Table 4.2. It can be seen that the Δy^+ values of several cases are below 30, meaning the cell nodes are located in the buffer-zone or even in the viscous region. It was therefore expected that the momentum results for these cases would fail, because the wall function was built with the condition that the wall adjacent cell center node lies within the log-layer. As the results will show, this condition is too strict for these simulations. The momentum results only failed when $\Delta y^+ < 12$.

Table 4.2: Overview of N and corresponding Δy^+, Re_τ and k^+.

Re_τ	360	360	360	540	720
k^+	15	30	60	90	120
N	Δy^+	Δy^+	Δy^+	Δy^+	Δy^+
$\frac{2}{3}$	22.5	45	90	135	180
1	15	30	60	90	120
2	7.5	15	30	45	60
3	5	10	20	30	40
4	3.75	7.5	15	22.5	30
5	3	6	12	18	24
6	2.5	5	10	15	20

In Figures 4.13 and 4.14, the results can be found for $N = \frac{2}{3}$. It can be seen that the velocity shift becomes slightly less accurate when k^+ increases. For the thermal correction it can be seen that the accuracy improved compared to the Reynolds analogy. Only for the lowest value of $k^+ = 15$, the improvement is minimal.

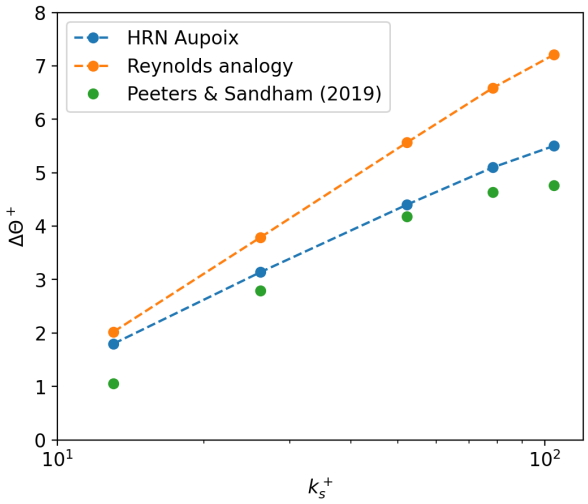

Figure 4.13: Temperature shift profile with $\Delta y^+ = k^+/\frac{2}{3}$.

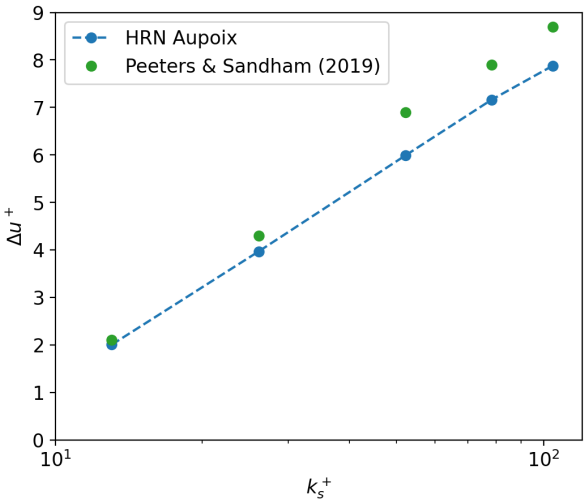

Figure 4.14: Velocity shift profile with $\Delta y^+ = k^+/\frac{2}{3}$.

In Figures 4.15 and 4.16, the results can be found for $N = 1$. The difference between the Reynolds analogy results and HRN Aupoix model has increased for all k^+ compared to the results with $N = \frac{2}{3}$.

This means the influence of the model has increased as well, which was expected for going from a very coarse to a finer mesh. Concerning the velocity shift, for all points the velocity shift is predicted within tolerances which can be expected for RANS computations and is of an equal magnitude compared to $N = \frac{2}{3}$.

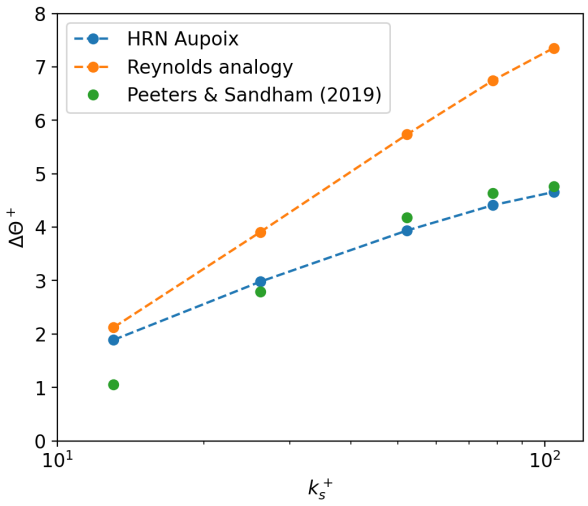

Figure 4.15: Temperature shift profile with $\Delta y^+ = k^+/1$.

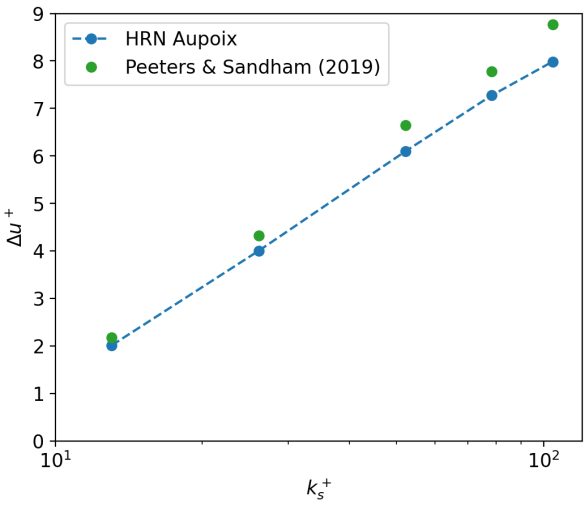

Figure 4.16: Velocity shift profile with $\Delta y^+ = k^+/1$.

In Figures 4.17 and 4.18, the results can be found for $N = 2$. For the first point, $k^+ = 15$, it can be seen that the velocity shift prediction failed. The predicted friction Reynolds number is equal to 447 and 415 for the smooth and rough case respectively instead of 360. When N was equal to 1, Δy^+ was equal to 15 and has now become 7.5. It is important to repeat these values for Δy^+ because the failure of the momentum prediction when $\Delta y^+ < 12$ will become apparent. Also the thermal prediction is wrong because the model relies on a correct prediction of the velocity shift. This can be seen at the first point of Figure 4.17. For the last three points in this figure, it can be seen that the difference between the Reynolds analogy and the HRN Aupoix model increased further. There is even an over-prediction of the reduction in heat transfer.

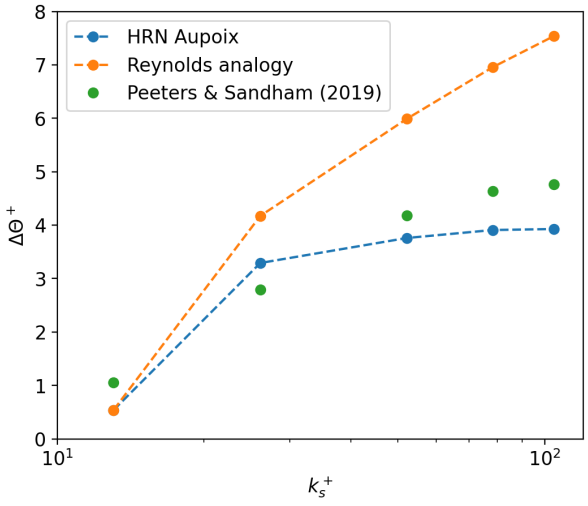

Figure 4.17: Temperature shift profile with $\Delta y^+ = k^+/2$.

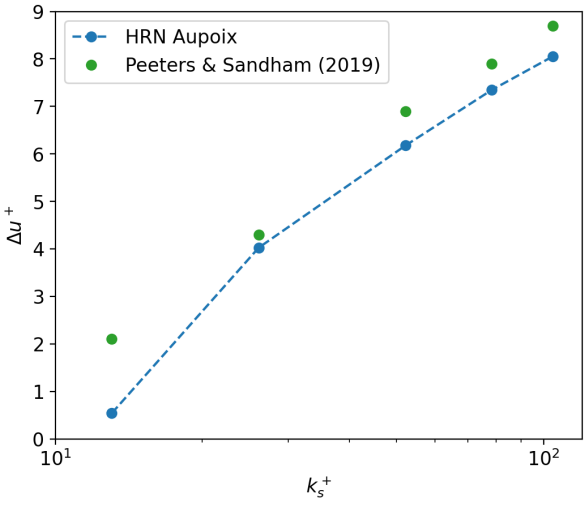

Figure 4.18: Velocity shift profile with $\Delta y^+ = k^+/2$.

In Figures 4.19 and 4.20, the results can be found for $N = 3$. It can be seen that also the prediction of the velocity shift for the second point fails. The Δy^+ value decreased from 15 to 10. As a consequence, the prediction of the temperature shift failed as well. Furthermore, the difference between the Reynolds

analogy and HRN Aupoix model has been decreased for the last three points compared to $N = 2$. This means the maximum impact of the thermal correction model was reached with $N = 2$, which was predicted in section 4.2
In Figures 4.21 and 4.22, the results can be found for $N = 4$, $N = 5$ and finally $N = 6$. In these graphs a failing velocity shift can be observed when $\Delta y^+ < 12$. This can best be seen for the cases where $k^+ = 60$. When $N = 5$, the velocity shift prediction is still accurate, when $N = 6$, the velocity shift prediction fails. The limit of $\Delta y^+ = 12$ has also been observed for the cases where $k^+ = 90$ and $k^+ = 120$. These results are not included in the thesis. Furthermore, for the points where the velocity shift is still accurate, a decreasing trend of the difference between the Reynolds analogy and HRN Aupoix model can once more be observed when the mesh becomes finer. Even though the estimate was wrong where the difference between the Reynolds analogy and HRN Aupoix model was at a maximum, the equilibrium between the cell area and damping function was observed in these results.

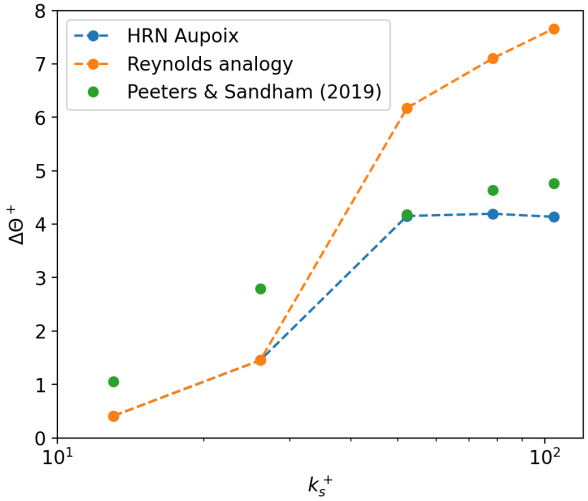

Figure 4.19: Temperature shift profile with $\Delta y^+ = k^+/3$.

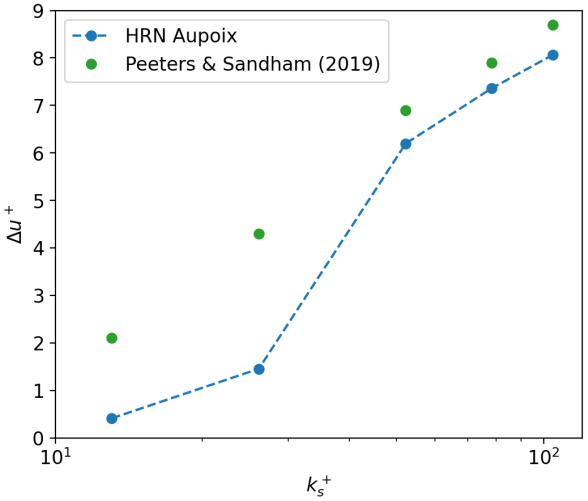

Figure 4.20: Velocity shift profile with $\Delta y^+ = k^+/3$.

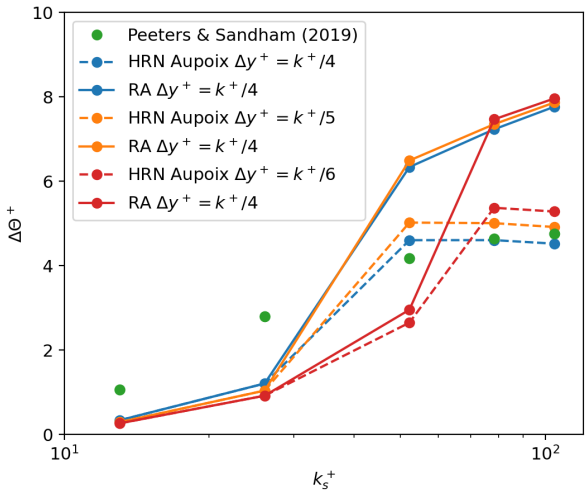

Figure 4.21: Temperature shift profile with $\Delta y^+ = k^+/4$, $\Delta y^+ = k^+/5$ and $\Delta y^+ = k^+/6$.

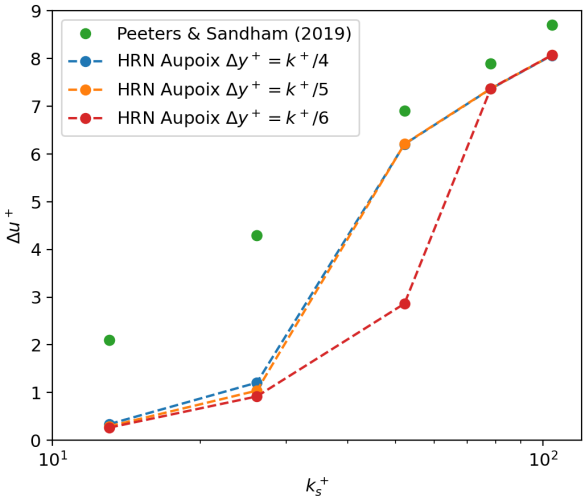

Figure 4.22: Velocity shift profile with $\Delta y^+ = k^+/4$, $\Delta y^+ = k^+/5$ and $\Delta y^+ = k^+/6$.

4.5. Channel Flow with Regular Roughness

4.5.1. Validation data

The validation data for the second test case comes from a DNS study by MacDonald et al. [46]. A cyclic channel flow with roughness on the upper and lower plates and a molecular Prandtl number of 0.7 was studied. The roughness height was set as a fraction of the channel half height δ. Therefore, a k^+ value for every case was described and the paper mentioned that $k_s^+ \approx 4.1k^+$. The driving force was a fixed mean velocity and was defined by a bulk Reynolds number. The bulk Reynolds number was varied until it matched a desired friction Reynolds number. This approach differs from the earlier reference data and is, however, the same approach as in this thesis. No values for the bulk Reynolds number have been mentioned. Therefore, several simulations have been ran, with the previous values from Peeters and Sandham [19] as starting point, until $\frac{Re_{\tau,RANS} - Re_{\tau,paper}}{Re_{\tau,paper}} < 0.02$. In the paper, the friction Reynolds number and roughness heights, in wall units, were varied from 395 to 1680 and 0 to 93.3 respectively. The simulated cases in the validation together with the corresponding bulk Reynolds numbers can be found in Table 4.3.

Table 4.3: Details of the DNS cases from MacDonald et al. [46] which are used as reference data.

k^+	k/δ	Re_τ	$Re_{B,used}$
0	0	395	14.6×10^3
0	0	590	22.9×10^3
0	0	720	28.6×10^3
0	0	1200	50.7×10^3
0	0	1680	73.9×10^3
11.0	1/36	395	11.6×10^3
21.9	1/18	395	9.7×10^3
32.8	1/18	590	13.7×10^3
40.0	1/18	720	16.4×10^3
66.7	1/18	1200	26.1×10^3
93.3	1/18	1680	36.3×10^3

The velocity and temperature shift found by Macdonald et al. can be seen in Figure 4.23 [46]. In the previous section it was noted that the results from Peeters and Sandham [19] saw leveling out of the temperature shift profile. For Macdonald et al. [46], this phenomenon can also be spotted. For the highest roughness height, even a decline can be seen in the temperature shift even though the velocity shift keeps increasing.

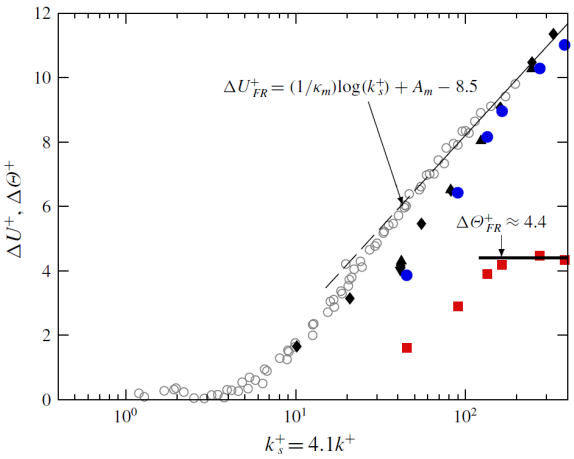

Figure 4.23: Velocity (blue circle) and temperature (red square) shift as function of the Reynolds roughness height k_s^+. Figure from MacDonald et al. [46].

4.5.2. Case description

The rough surface MacDonald et al. [46] used is a three-dimensional sinusoidal surface applied to both the top and bottom wall. The corresponding equation describing the roughness can be found in Equation 4.11. λ_x and λ_z are the sinusoidal wavelengths and are both equal to $7.07k$ and k is the sinusoidal semi-amplitude, given by the earlier mentioned table. Because the wavelengths are dependent on the roughness height, every surface of the reference cases is different. The length in the x-direction has been taken from the reference paper and $L_z = L_x/3$. In Figures 4.24 and 4.25 the surfaces of $k^+ = 11.0$ and $k^+ = 93.3$ can be found. In Figure 4.26 and 4.27 the corrected surfaces with the same roughness heights can be seen. The corrected surfaces are found by neglecting roughness below the meltdown height, which was equal to 0 for these cases.

$$h(x,z) = k \cos\left(\frac{2\pi x}{\lambda_x}\right) \cos\left(\frac{2\pi z}{\lambda_z}\right) \tag{4.11}$$

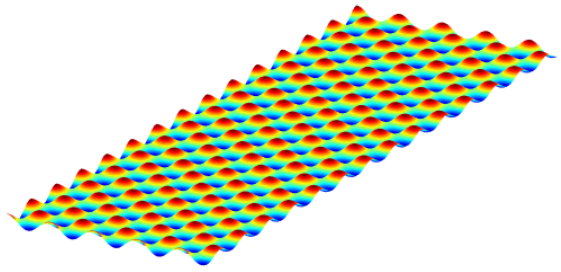

Figure 4.24: Sinusoidal rough surface with $k^+ = 11.0$.

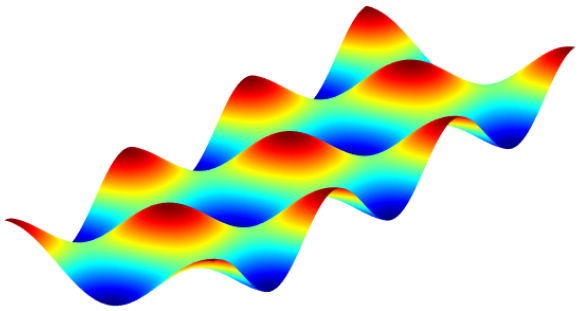

Figure 4.25: Sinusoidal rough surface with $k^+ = 93.3$.

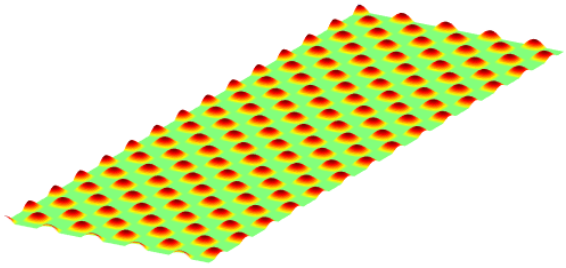

Figure 4.26: Sinusoidal rough surface with $k^+ = 11.0$ without roughness below the meltdown height.

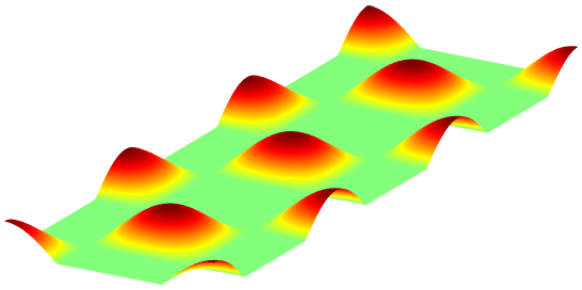

Figure 4.27: Sinusoidal rough surface with $k^+ = 93.3$ without roughness below the meltdown height.

The corrected surface ratio of the different surfaces are equal to each other. This has been verified with the smallest and biggest roughness height. Therefore, it was assumed that it also will be the case for the intermediate roughness heights. The convergence of the calculated corrected surface ratio for both surfaces can be seen in Figure 4.28 and is found to be 1.089, which is larger compared to the calculated corrected surface ratio from the Peeters and Sandham [19] surface.
For the prediction of the velocity shift, it was important again to predict k_s^+ using k^+ and obtain a C_s value to be used in Equation 4.2. In the reference paper it is mentioned that $k_s^+ = 4.1k^+$. It was found that when $k_s^+ = 4.1k^+$ and $C_s = 0.253$ is used, the prediction of the velocity shift was not accurate for smaller roughness heights. This can be seen in Figure 4.29. Cebeci and Bradshaw [29] stated that when roughness deviates from Nikuradse type roughness, a higher value for C_s should be chosen. According to Kadivar et al. [13], C_s values up to 10 have been reported by various experiments. For the validation it has therefore been chosen to assume $k_s^+ = k^+$ and use a C_s value of 1.0 because it gave more accurate results for the smaller roughness heights, see more Figure 4.29.

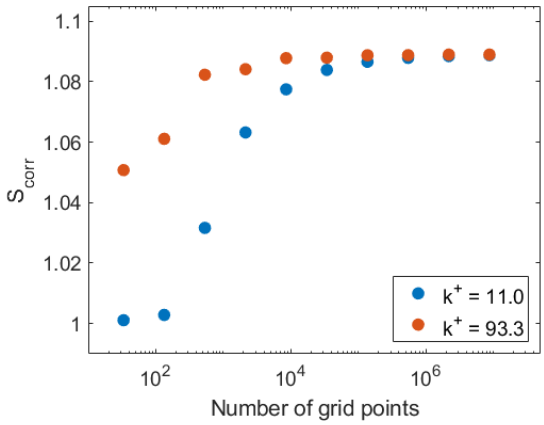

Figure 4.28: The calculated corrected surface as function of the number of grid points. It can be seen that the value converged to 1.089 for both surfaces.

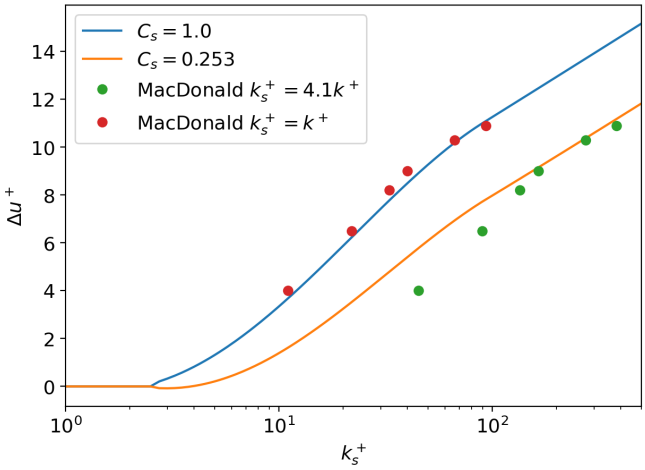

Figure 4.29: Δu^+ prediction for the MacDonald et al. [46] case. Predictions using Nikuradse type roughness with $C_s = 0.253$ and $C_s = 1.0$ are also shown.

4.5.3. Results

To see the effect of the mesh size on the results, multiple meshes have been made. The velocity and temperature profiles of rough cases have been compared to those of the cases without roughness. For each mesh a temperature and velocity shift graph has been made by calculating the average shift in velocity and temperature profile for $\Delta y^+ > 30$. This time, it has been chosen to simply vary the number of cells in the y-direction because the ratio between the friction Reynolds number and roughness is larger. This gave the possibility to use, relatively, coarser meshes compared to the previous validation. An overview of the different mesh sizes with corresponding friction Reynolds number, roughness and Δy^+ of the wall adjacent cell can be found in Table 4.4. The influence of the mesh size on the results have been studied for more meshes than presented in the table. However, it has been chosen to present a selection which gave the clearest overview.

In Table 4.4 Δy^+ values smaller than 30 can be seen, which means that these cell nodes are located in the buffer-zone or viscous region. It could therefore be expected that the prediction of the velocity shift would fail for these cases. However, in agreement with the previous results, this condition is too strict and the momentum prediction only failed when $\Delta y^+ < 12$.

Table 4.4: Overview of the number of cells for the different meshes and corresponding Δy^+, Re_τ and k^+.

Re_τ	395	395	590	720	1200	1680
k^+	11.0	21.9	32.8	40.0	66.7	93.3
Number of cells in channel half-height	Δy^+	Δy^+	Δy^+	Δy^+	Δy^+	Δy^+
4	49.4	49.4	73.8	90	150	210
8	24.7	24.7	36.9	45	75	105
12	16.5	16.5	24.6	30	50	70
18	11.0	11.0	16.4	20	33.3	46.7
28	7.1	7.1	10.5	12.9	21.4	30
40	4.9	4.9	7.4	9	15	21

In Figures 4.30 and 4.31 the results can be found for 4 cells in the channel half-height. It can be seen that the velocity shift is predicted accurately and arguably better compared to the previous case. For the thermal correction, it can be seen that there is a slight improvement compared to the Reynolds analogy for most roughness heights. Only for $k^+ = 11.0$, the influence of the correction model is almost zero.

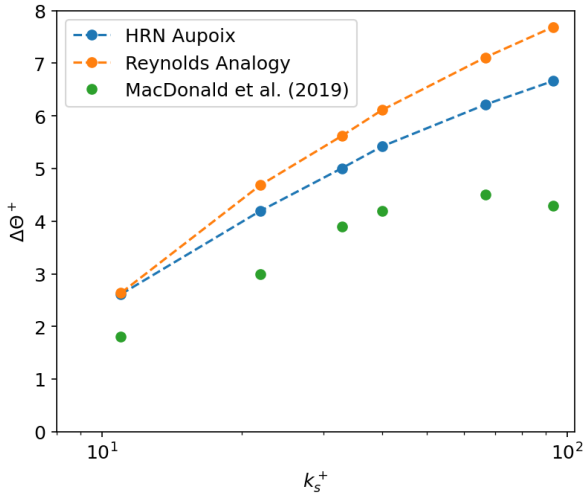

Figure 4.30: Temperature shift profile with 4 cells in the channel half-height.

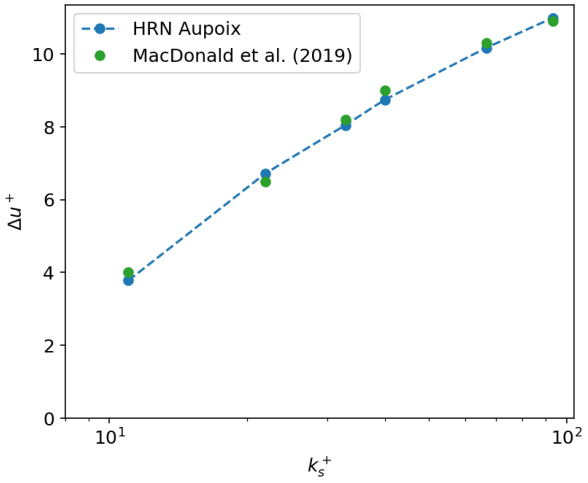

Figure 4.31: Velocity shift profile with 4 cells in the channel half-height.

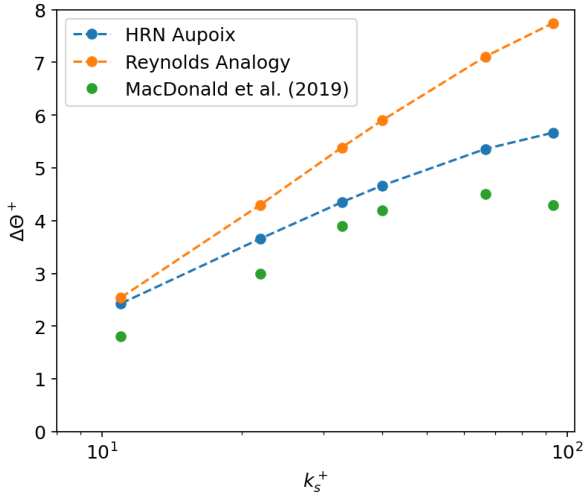

Figure 4.32: Temperature shift profile with 8 cells in the channel half-height.

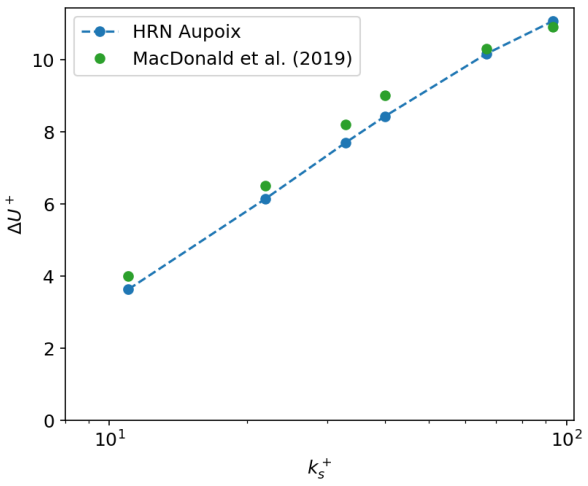

Figure 4.33: Velocity shift profile with 8 cells in the channel half-height.

In Figures 4.32 and 4.33 the results can be found for 8 cells in the channel half-height. The velocity shift predictions are still accurate and the influence of the mesh size is minimal. The temperature shift predictions show an improvement compared to 4 cells in the channel half-height. The difference between the Reynolds analogy and the thermal correction model has been increased as expected when comparing a very coarse to a finer mesh. For $k^+ = 11.0$, the difference between the Reynolds analogy and thermal correction modal is still marginal.
In Figures 4.34 and 4.35 the results can be found for 12 cells in the channel half-height. The velocity shift predictions are still accurate and the influence of the mesh size is minimal. The temperature shift predictions show a further increase in the difference between the Reynolds analogy and thermal correction model. Around this mesh size, up to around 18, the difference is at a maximum. Compared to the results of the previous case, there is no over prediction of the reduction in heat transfer.

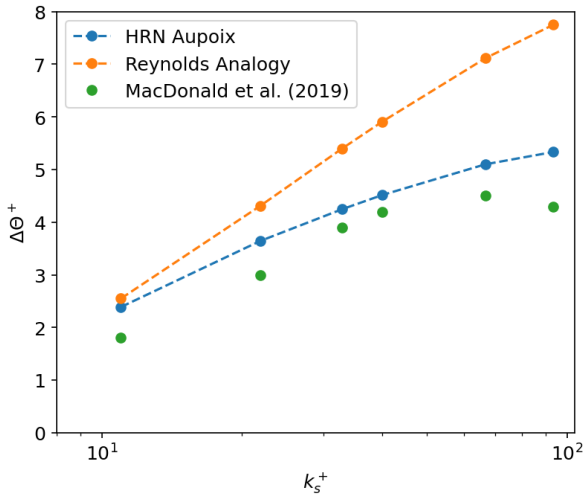

Figure 4.34: Temperature shift profile with 12 cells in the channel half-height.

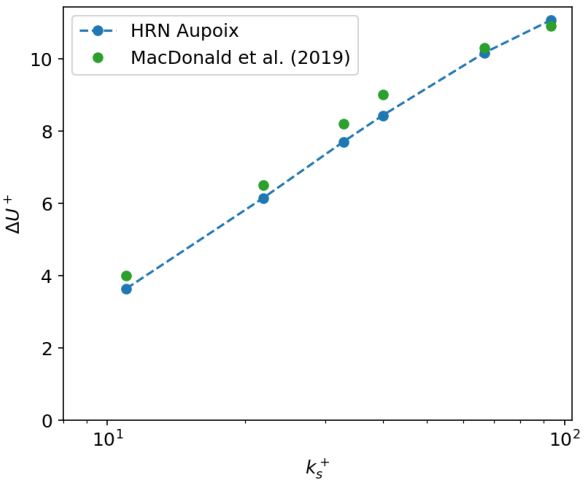

Figure 4.35: Velocity shift profile with 12 cells in the channel half-height.

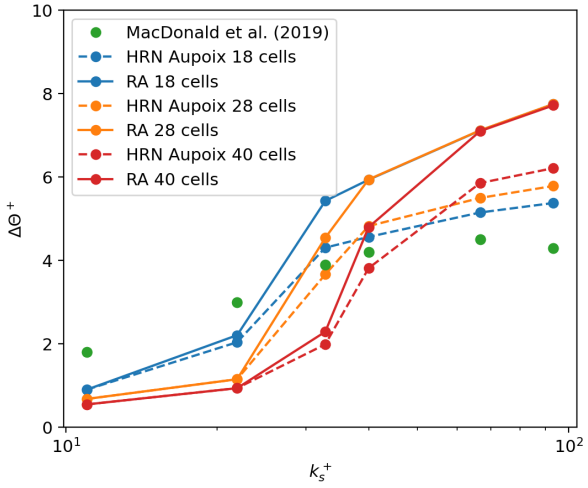

Figure 4.36: Temperature shift profile with 18, 28 and 40 cells in the channel half-height.

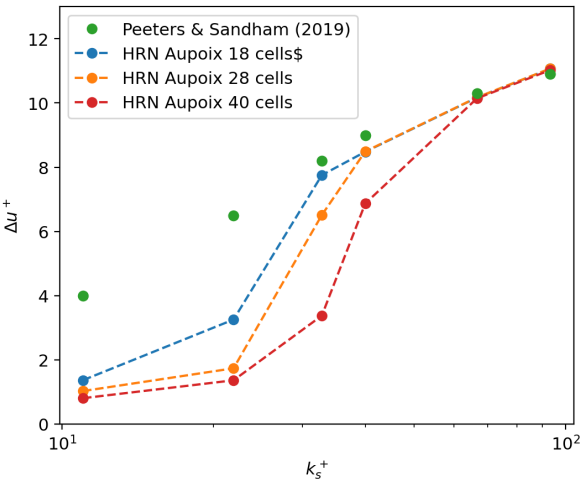

Figure 4.37: Velocity shift profile with 18, 28 and 40 cells in the channel half-height.

In Figures 4.36 and 4.37 the results can be found for 18 cells in the channel half-height. In the graph showing the velocity shift it can be seen that the prediction failed for $Re_\tau = 395$. The corresponding Δy^+ for the wall adjacent cell is 11.0. When the mesh size was 16 cells for the channel half-height, Δy^+ was equal to 12.3 and no failure of the predication could be seen. This further confirmed the failure of the momentum prediction when $\Delta y^+ < 12$. Because the velocity shift prediction failed, also the

temperature shift prediction failed for $k^+ = 11.0$ and $k^+ = 21.9$. For the other roughness heights, the difference between the Reynolds analogy and the thermal correction model is still at a maximum.
In Figures 4.36 and 4.37 also the results for 28 and 40 cells, in the channel half-height can be found. For both mesh sizes the failure of the momentum prediction can be seen for smaller friction Reynolds numbers. This happened for all the simulations where $\Delta y^+ < 12$. For the points where the velocity shift is still accurate, a decreasing trend of the difference between the Reynolds analogy and HRN thermal correction model can once more be observed when the mesh becomes finer. Even though the estimate was wrong where the maximum difference between the Reynolds analogy and HRN thermal correction model was, the equilibrium between the cell area and damping function can still be observed in these results.

4.6. Conclusion

The thermal correction model from Aupoix [5] is based on modifying the turbulent Prandtl number in every cell of the mesh by adding ΔPr_t to Pr_t. ΔPr_t is calculated using two functions which are multiplied by each other; $\mathcal{F}$ and $\mathcal{G}$. $\mathcal{F}$ is the actual model computed by the corrected surface ratio and predicted velocity shift. $\mathcal{G}$, the damping function, only makes sure the model is restricted to the wall region and its value decreases as a function of the wall distance and roughness height. A prerequisite to make the thermal correction function properly is that the mesh is fully resolved, which entails $\Delta y^+ \approx 1$ for the wall adjacent cell (LRN).
The downside of a LRN mesh is the amount of cells required in the computational domain, which is much larger compared to that of a HRN mesh. As a consequence, the computational time increases significantly when solving a case on a LRN instead of a HRN mesh. The goal was to find a thermal correction model which can be applied on a HRN mesh as well. Therefore, the model from Aupoix [5] is applied as a wall function on a HRN mesh in the wall adjacent cell only and has been tested.
Due to the damping function it was expected that the results on the two different cases are dependent on the wall adjacent cell size. When looking at the results, this is indeed the case. It could be seen that when the mesh became finer, the correction on the Reynolds analogy increased due to an increasing value of the damping function. At a certain mesh size a limit was reached in which the difference between the Reynolds analogy and the HRN thermal correction model was at its largest. After that point, whilst the mesh size kept decreasing, the increasing behaviour of the damping function could not oppose the decreasing cell height and so the magnitude of the correction on the Reynolds analogy solution decreased as well.
It can also be stated that it is in general required for the velocity shift prediction to make sure that $\Delta y^+ > 12$ for the wall adjacent cell to give accurate results. When the velocity shift was not predicted accurately, the temperature shift could also not be computed with satisfying results.
Even though the results showed that implementing the LRN thermal correction model from Aupoix [5] does not work when it is implemented on a HRN mesh in the wall adjacent cell only, a possible improvement of the HRN thermal correction model to give more accurate results has been identified. The damping function $\mathcal{G}$ is dependent on the mesh size and will therefore be reevaluated to decrease its dependency. It is assumed that the actual correction $\mathcal{F}$ should not be modified because the only input are roughness parameters such as the corrected surface and predicted velocity shift. The approach and results of the modification of the damping function will be discussed in the next chapter.

5 Calibration

In this chapter it is explained how the model has been modified and how the modified model has been calibrated using the DNS data from the previous chapter.

5.1. Modification

In the original model from Aupoix [5], the Prandtl correction was applied in every cell of the computational domain. To restrict the effect of the model to the wall region a damping function was introduced (see Equation 2.59). As discussed in the previous chapter, in this thesis the model is implemented in a different way. The Prandtl correction is only applied in the wall adjacent cell and consists of two parts; the actual correction (as function of the corrected surface ratio and the predicted velocity shift) and the damping function. Because the value of the damping function is dependent on the roughness height and the size of the wall adjacent cell, the results were dependent on the mesh size.
Therefore, a new damping function had to be found to reduce this dependency. The new damping function has been made by finding the value of $\mathcal{G}$, for every roughness height and various mesh sizes, which reduced the error between the RANS simulations and DNS data. With these values, two fits have been made for each molecular Prandtl number used in the cases from the previous chapter.

5.2. Calibration approach

5.2.1. Optimization problem

Finding the correct values for $\mathcal{G}$ can be seen as an optimization problem and can be stated as: minimize the error function $f(\mathcal{G})$ in which $f(\mathcal{G})$ is the difference between the temperature shift of the RANS simulation outcome and corresponding DNS reference data as function of $\mathcal{G}$. Note, f is the outcome of the error function and should not be confused with $\mathcal{F}$, which is part of the calculation of $\Delta Pr_{t,rough}$. The average temperature shift has been calculated using Equation 5.1 in which i indicates the first index where $y^+ > 30$ and N the last. $\Theta_{i,rough}$ and $\Theta_{i,smooth}$ are the temperature values for the rough and smooth simulation respectively. The temperature profile for the smooth cases have been calculated in advance with the same amount of cells as for the rough case. $\Delta\Theta^+_{RANS}$ has been compared with the value from the DNS reference data, $\Delta\Theta^+_{DNS}$, until Equation 5.2 is satisfied in which tol is the required tolerance.

$$\Delta\Theta^+_{RANS} = \frac{\sum_{i=1}^{N}(\Theta_{i,rough} - \Theta_{i,smooth})}{N} \tag{5.1}$$

$$f(\mathcal{G}) = |\Delta\Theta^+_{RANS} - \Delta\Theta^+_{DNS}| < tol \tag{5.2}$$

5.2.2. Golden section search

To find the value for $\mathcal{G}$ for every mesh size and k^+, it would be an option to brute force the solution by trying every value with a certain tolerance between two boundaries. This method would however take

considerably more time and would therefore occupy the data-cluster for a longer period than necessary. Therefore, the golden section search method has been used [77].
The golden section search method was chosen because it is not required to calculate the gradient of the error as function of $\mathcal{G}$ since the derivative is unknown. The algorithm will converge to the minimum of the function (in case there is one), to one of them (in case there are more than one minima) or to the boundary of the search domain if no minima are found. This can for example be the case when the minimum is outside the domain. Using this algorithm, as opposed to brute forcing, has as benefit that either a reduced number of evaluations for the same tolerance are required or a smaller tolerance for the same number of evaluations is achieved.
The golden section search works as follows. The algorithm is started with four points; a^i, b^i, c^i and d^i in which i is the iteration index, starting at 0. The points represent a value of $\mathcal{G}$ with a^0 and b^0 being the boundary points i.e. the minimum and maximum value of $\mathcal{G}$ for which the error will be computed. For the algorithm it is only important to know whether $f(c^i) > f(d^i)$ or $f(d^i) > f(c^i)$. So only $f(c^i)$ and $f(d^i)$ needs to be determined to initialize the search and not $f(a^i)$ and $f(b^i)$ as well, saving computational time.

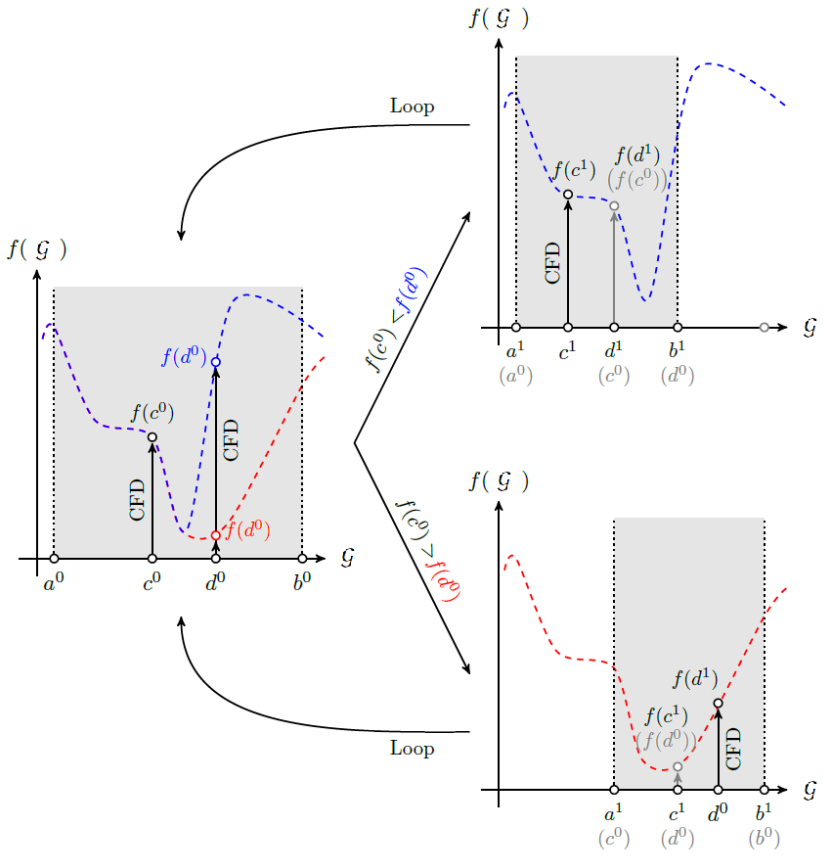

Figure 5.1: Schematic overview of comparing $f(c^i)$ and $f(d^i)$ to each other and determining the new values for a^i, b^i, c^i and d^i to compute the boundaries before starting the process again until the value for $\mathcal{G}$ has been found which makes sure $f(\mathcal{G}) =< tol$.

The new boundary values for $\mathcal{G}$ are determined by the outcome of $f(c^i)$ and $f(d^i)$. If $f(d^i) > f(c^i)$, the minimum must lie between a^i and d^i. The values for the next iteration will then become $a^{i+1} = a^i$, $b^{i+1} = d^i$, $d^{i+1} = c^i$. c^{i+1} will be determined with the use of the golden ratio, which will be explained later. This new point is also the only point where a new CFD simulation is required because $f(d^{i+1}) = f(c^i)$ and has already been computed.
When $f(c^i) > f(d^i)$, the minimum must lie between c^i and b^i. The values for the next iteration will then become $a^{i+1} = c^i$, $b^{i+1} = b^i$, $c^{i+1} = d^i$. d^{i+1} will be determined with the use of the golden ratio. This new point is also the only point where a new CFD simulation is required, because $f(c^{i+1} = f(d^i)$ and

has already been computed. The process of comparing $f(c^i)$ and $f(d^i)$ to each other and determining the new a^i, b^i, c^i and d^i is visualised in Figure 5.1.
To minimize the number of iterations, the ratio between $|c-a|$ and $|d-c|$ should equal the ratio of $|b-d|$ and $|d-c|$ and to the ratio of $|b-c|$ and $|c-a|$. This ratio happens to be equal to the golden ratio $\phi = 1.618...$, hence the name of the algorithm [77]. This results in the following expressions for the points c and d, where $\Delta x = b - a$:

$$\begin{aligned} c &= b - (\Delta x/\varphi) \\ d &= a + (\Delta x/\varphi) \end{aligned} \tag{5.3}$$

The formula above is valid for every iteration and is therefore used to determine not only c^0 and d^0 but also c^{i+1} and d^{i+1}, depending on which point has to be determined. At last, the theoretical maximum number of iterations before the tolerance criterion is met can be calculated using Equation 5.4. In which Δx^0 and Δx^{tol} are the initial difference between a and b and the tolerance respectively.

$$N = \frac{\ln\left(\frac{\Delta x^{tol}}{\Delta x^0}\right)}{\ln(\varphi - 1)} \tag{5.4}$$

When obtaining the results, first an estimation run has been performed by setting the boundaries a^0 and b^0 to 0 and 10 respectively. No negative values were expected, because the RANS simulations without the implemented model always showed an over prediction of the heat transfer. The value of 10 has been estimated by performing some manual test runs on individual cases. The tolerance was set to 1 to limit the number of iterations and thus the computational time. The tolerance was then reduced in, two steps, to 0.1 and 0.01 while also narrowing the initial boundary values to obtain the correct values of $\mathcal{G}$. In practice this was only achieved by reducing b^0, because the lowest values remained close to 0.

5.3. Calibration results

5.3.1. Irregular roughness

The first case which has been calibrated is the cyclic channel flow with irregular roughness on both walls from Peeters and Sandham [19]. The golden section search algorithm has been used on the five roughness heights and on 23 different mesh sizes. The mesh sizes were varied by changing the number of cells in the channel-half height from 2 to 24. The finest mesh of 24 cells has been chosen because for $k^+ = 120$, the corresponding friction Reynolds number was 720 and this would give an estimated Δy^+ value of 15 for an uniform mesh in the wall-normal direction. It has already be shown that for smaller values of Δy^+, the momentum prediction fails. Therefore $\Delta y^+ = 15$ has been set as the minimum cell size. For the roughness heights with $Re_\tau = 360$ and $Re_\tau = 540$, the Δy^+ values were smaller than 15 for certain numbers of cells. For these cases the value for $\mathcal{G}$ has been set to 0 in the algorithm and no CFD simulations have been run. This was possible, because the smooth reference simulations were computed in advance. This reduced the computational time significantly because it was unnecessary to run rough simulations where $\Delta y^+ < 15$.
The calibrated values for $\mathcal{G}$ have been plotted in several ways to find a possible relationship between different input parameters such as the roughness- and cell-height in both wall and non-wall units. Three different graphs have been made using the same data set and will be shown. Firstly, the calculated values of $\mathcal{G}$ have been plotted as function of Δy^+. Secondly, the calculated values have been plotted as function of $\Delta y^+/k^+$. At last, the calculated values have been plotted as function of $\Delta y^+/k_s^+$, in which $k_s^+ = 0.87k^+$. These graphs can be found in Figures 5.2, 5.3 and 5.4. In these Figures also the original damping function has been plotted as a reference.
When looking at Figure 5.2 it can be seen that the shape of the estimated values for $\mathcal{G}$ for each roughness height is similar. When Δy^+ is small, the value of $\mathcal{G}$ is at its largest and decreases rapidly with increasing Δy^+. Also the gradient of $\mathcal{G}$ decreases when Δy^+ increases (less negative). Furthermore, the function $\mathcal{G}$ appears to reach a constant value or asymptote for every k^+. It can also be seen that when k^+ increases, the overall value for $\mathcal{G}$ increases as well. This was also the case for the original damping function. The only exception is for $k^+ = 15$. This roughness height does not follow the trend of decreasing values of $\mathcal{G}$, they increased instead of decreased. Compared to the original damping function, there is less distinction between different roughness heights. Furthermore, the simulations

where $\Delta y^+ < 15$ can be identified by either the location on the x-axis or by a value of 0 on the y-axis (with one exception where an unidentified error occurred and resulted in a $\mathcal{G}$ of 0). These simulations have not been taken into account when the data was fitted. When the data is plotted in this way, no relation has been found between $\mathcal{G}$, Δy^+ and k^+. This entails that $\mathcal{G}$ is by no means a function of Δy^+ alone and the original damping function does not correctly calculate the temperature shift.

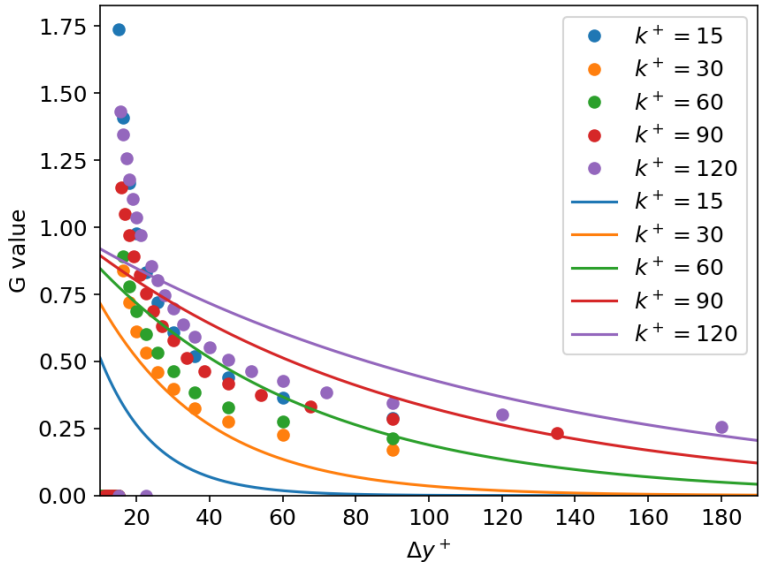

Figure 5.2: $\mathcal{G}$ as function of Δy^+. Dots represent the values found by the golden section search for the different roughness heights. Lines represent the original damping function from Aupoix [5].

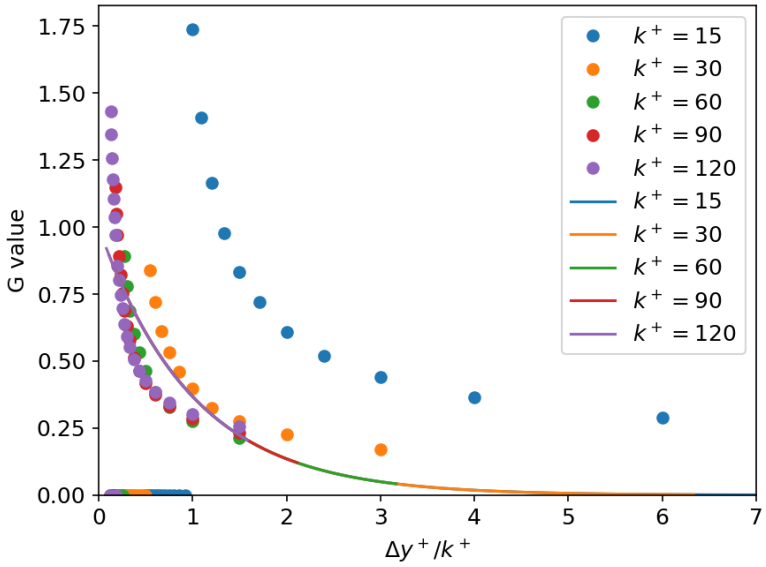

Figure 5.3: $\mathcal{G}$ as function of $\Delta y^+/k^+$. Dots are the found values by the golden section search for the different roughness heights. Lines represent the original damping function from Aupoix [5].

In Figure 5.3 the distance from the wall to the cell center of the wall adjacent cell is normalized by the roughness height (both in wall units). It can immediately be seen that the three largest roughness heights overlap with each other. The two other roughness heights deviate from this trend, especially for $k^+ = 15$. It can be noted that the results for $k^+ = 15$ do not match with the rest of the data for the second time, indicating divergent behaviour compared to the other roughness heights. It can also be seen that, for the larger roughness heights, the data intersects the original damping function twice. In between, the original damping function returns a higher $\mathcal{G}$ value than required. This corresponds to the

findings of the previous chapter. In the previous chapter it was seen that for a certain range of Δy^+ the original damping function, in combination with the current implementation of the model from Aupoix [5], over predicted the decrease in heat transfer.

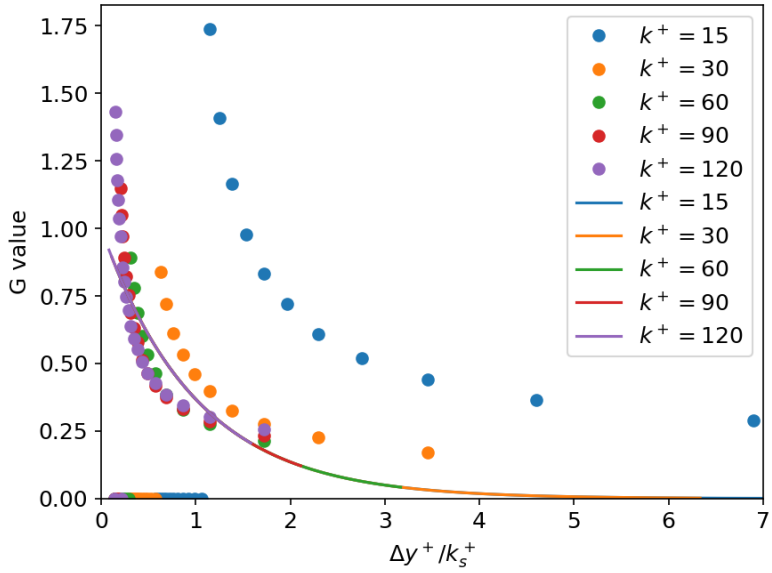

Figure 5.4: $\mathcal{G}$ as function of $\Delta y^+/k_s^+$. Dots are the found values by the golden section search for the different roughness heights. Lines represent the original damping function from Aupoix [5].

In Figure 5.4 the distance from the wall to the cell center of the wall adjacent cell is normalized by the equivalent sand grain height (again both in wall units). It can again be seen that the three largest roughness heights overlap with each other and that the two other, smaller, roughness heights deviate from this trend. The difference between Figures 5.3 and 5.4 is small because also the difference between k^+ and k_s^+ is small for this roughness type ($k_s^+ \approx 0.87k^+$).
Therefore, the damping function for the three largest roughness heights can be described by a single equation.

5.3.2. Regular roughness

The second case which has been calibrated is the cyclic channel flow with regular roughness on both walls from MacDonald et al. [46]. The golden section search algorithm has been used on the six roughness heights and 55 different mesh sizes. The mesh sizes were varied by changing the number of cells in the channel-half height from 2 to 56 cells. The finest mesh of 56 cells has been chosen because for $k^+ = 93.3$, the corresponding friction Reynolds number was 1680. This would give an estimated Δy^+ of 15. It has already be shown that for smaller values of Δy^+, the momentum prediction fails. Therefore $\Delta y^+ = 15$ has been set as the minimum cell size. For the roughness heights where Re_τ was 1200, 720, 590 and 395, Δy^+ could be smaller than 15 for certain numbers of cells. For these cases the value for $\mathcal{G}$ has again been set to 0 in the algorithm and no CFD simulations have been run to decrease the computational time.
The calibrated values for $\mathcal{G}$ have been plotted in the same way to find a possible relationship between different input parameters. Three different graphs have been made using the same data set. Firstly, the calculated values of $\mathcal{G}$ have been plotted as function of Δy^+. Secondly, the calculated values have been plotted as function of $\Delta y^+/k^+$. At last, the calculated values have been plotted as function of $\Delta y^+/k_s^+$. To determine k_s^+, this time the original assumption from MacDonald et al. [46] has been used, which is $k_s^+ = 4.1k^+$. These graphs can be found in Figures 5.5, 5.6 and 5.7. In these Figures also the original damping function has been plotted as a reference.
In Figure 5.5 it can be seen that the range of Δy^+ is more than twice as large compared to the range of the previous calibration. This was possible due to higher friction Reynolds numbers of the flows. It can also be seen, when compared to the previous calibration, that when Δy^+ approaches 15, the values of $\mathcal{G}$ are larger. The results further differ from the previous calibration in the sense that the four

smallest roughness heights overlap each other (the two larger roughness heights do not). Besides these differences, also a similarity can be seen in the graph. When the roughness height decreases, the overall value for $\mathcal{G}$ decreases as well. For the previous results this was true up till $k^+ = 30$. For these results this is true up till $k^+ = 40$, so the difference might be explained by the differences in roughness height range of the two cases.

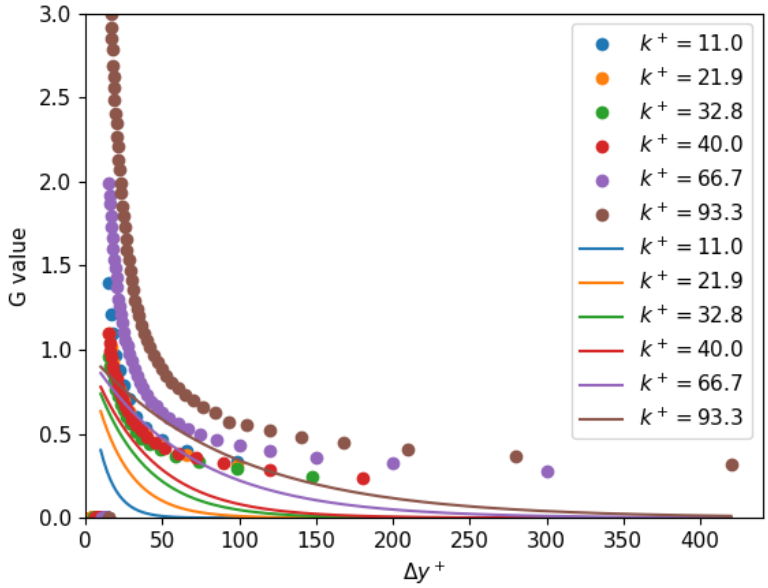

Figure 5.5: $\mathcal{G}$ as function of Δy^+. Dots are the found values by the golden section search for the different roughness heights. Lines represent the original damping function from Aupoix [5].

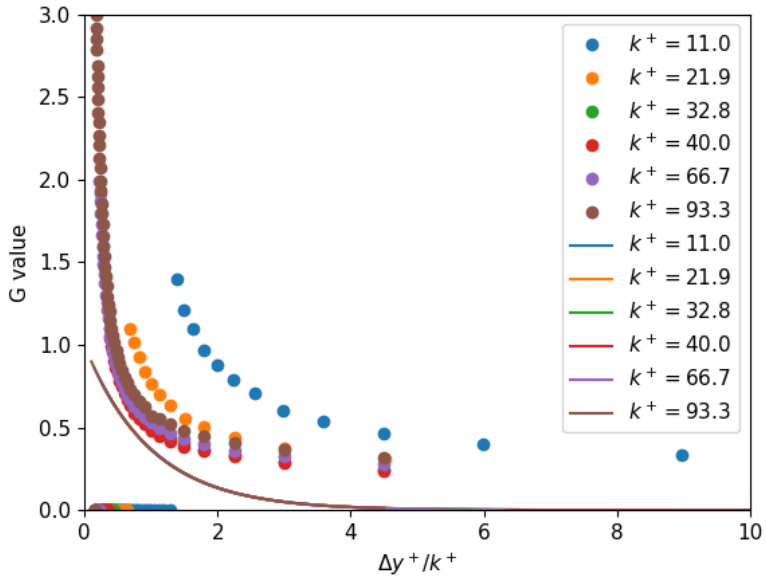

Figure 5.6: $\mathcal{G}$ as function of $\Delta y^+/k^+$. Dots are the found values by the golden section search for the different roughness heights. Lines represent the original damping function from Aupoix [5].

In Figure 5.6 the distance from the wall to the cell center of the wall adjacent cell is normalized by the roughness height (both in wall units). It can immediately be seen that the four largest roughness heights overlap with each other. For $\Delta y^+/k^+ > 1.5$, the overlap is less obvious compared to the previous calibration. The two other roughness heights deviate from this trend, especially for $k^+ = 11$. For $k^+ = 21.9$ it can be seen that around $\Delta y^+/k^+ \approx 2$ the found values for $\mathcal{G}$ start to overlap with

the larger roughness height, albeit for three data points only. It can also be seen that there is no intersection with the original damping function. The values found with the calibration are larger for all roughness heights and mesh sizes. This corresponds to the findings of the previous chapter. In the previous chapter it was seen that for all roughness heights and mesh sizes, in combination with the implementation of the model from Aupoix [5], under predicted the decrease in heat transfer.
In Figure 5.7 the distance from the wall to the cell center of the wall adjacent cell is normalized by the equivalent sand grain height (again both in wall units). The same observations as for the previous graph can be made, except for the comparison with the original damping function. This time an intersection between the data set and original damping function can be seen. The difference between Figures 5.6 and 5.7 is significant because the difference between k^+ and k_s^+ is significant as well.
From the graphs it can concluded that for this case the damping function for the four largest roughness heights can be described with a single equation.

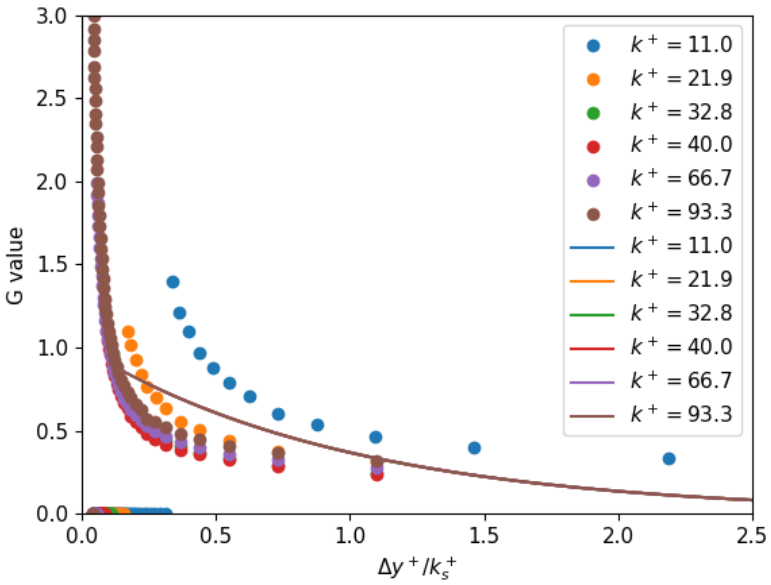

Figure 5.7: $\mathcal{G}$ as function of $\Delta y^+/k_s^+$. Dots are the found values by the golden section search for the different roughness heights. Lines represent the original damping function from Aupoix [5].

5.4. Fitting

With the data sets found for $\mathcal{G}$, several fitted functions have been made to describe the required value of the damping function. The data sets were computed for flows with two different molecular Prandtl numbers and there is no noticeable overlap between the two data sets. It is therefore expected that a correct fit is Prandtl number dependent. Because there is no data available for more Prandtl numbers, it was decided to make a separate fit for each Prandtl number instead of making a single Prandtl dependent fit.
When $\mathcal{G}$ was plotted against Δy^+, no relationship could be seen. When the data sets were normalized by either k^+ or k_s^+, it became apparent that there could be a relationship between $\mathcal{G}$ and $\Delta y^+/k^+$ or $\Delta y^+/k_s^+$. Qualitatively seen, there is no difference between the two relationships. Therefore, two distinct fitting functions have been made for each Prandtl number. Curve fitting has been used to find the equations.
A power function in the shape of Equation 5.5 was found to best suit the data. In this equation is x either $\Delta y^+/k^+$ or $\Delta y^+/k_s^+$ and a, b and c are constants which have been determined by the fitting tool. The only downside of this type of equation is that for higher values of x, $\mathcal{G}$ will reach a constant value which is equal to c. It is expected that for very high ratios between the cell and roughness heights, the true value of $\mathcal{G}$ keeps decreasing because a larger cell size corresponds to a lower value.

$$\mathcal{G} = ax^b + c \tag{5.5}$$

The fits which are a function of $\Delta y^+/k_s^+$ can be found in Equations 5.6 and 5.7 for the two different

data sets. In these equations the subscript indicates the Prandtl number for which the fit has been made. The fits which are a function of $\Delta y^+/k^+$ can easily be found by substituting $k_s^+ = 0.87k^+$ and $k_s^+ = 4.1k^+$ for $Pr = 1.0$ and $Pr = 0.7$ respectively. It can be seen that the two damping functions indeed can not be described by a single fit because the coefficients differ significantly. It is expected that the Prandtl number plays a role as well.

$$\mathcal{G}_{1.0}\left(\frac{\Delta y^+}{k_s^+}\right) = 0.1559\left(\frac{\Delta y^+}{k_s^+}\right)^{-1.088} + 0.153 \tag{5.6}$$

$$\mathcal{G}_{0.7}\left(\frac{\Delta y^+}{k_s^+}\right) = 0.0211\left(\frac{\Delta y^+}{k_s^+}\right)^{-1.539} + 0.323 \tag{5.7}$$

The fits are plotted in Figure 5.8 and 5.9 for $\Delta y^+/k^+$ and $\Delta y^+/k_s^+$ respectively. In these figures it can be seen that the range, in which $\mathcal{G}$ has been found, is larger for the MacDonald et al. [46] case.

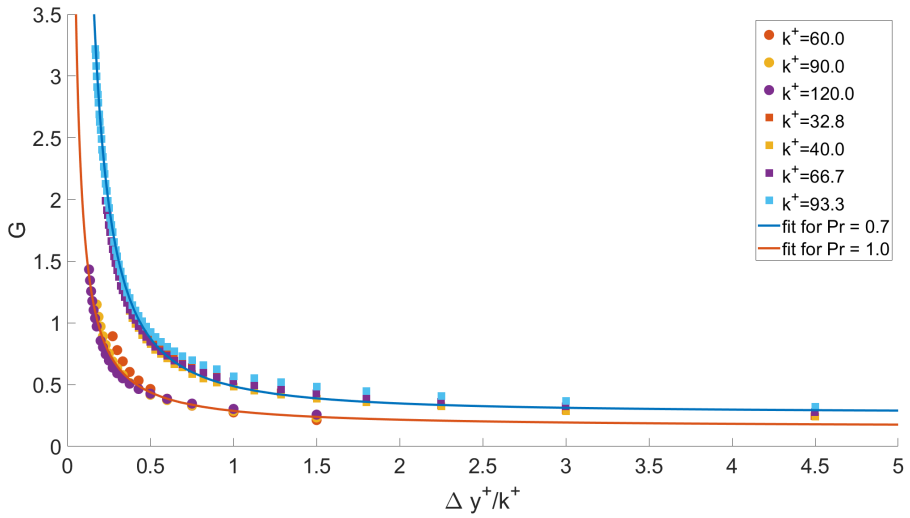

Figure 5.8: Fitted curves for $\Delta y^+/k^+$ with the data points for which the fits have been made. Circles are for Peeters and Sandham [19], squares are for MacDonald et al. [46].

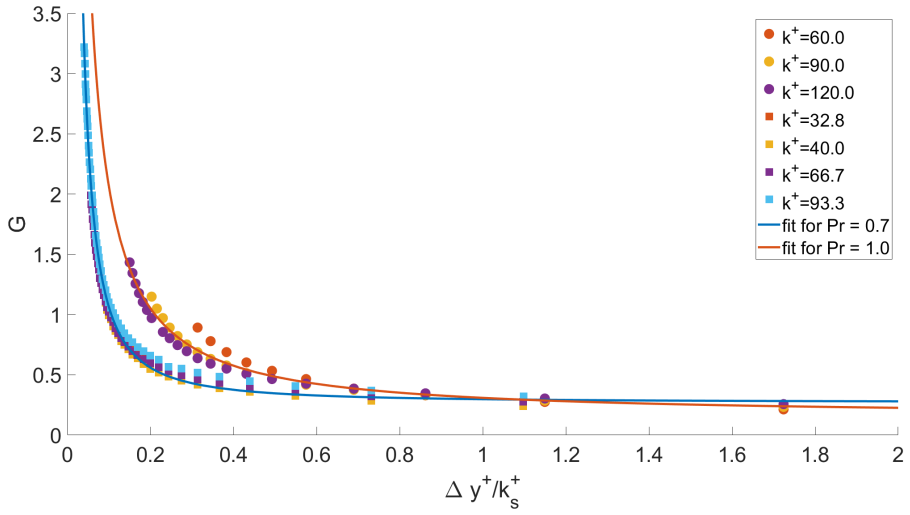

Figure 5.9: Fitted curves for $\Delta y^+/k_s^+$ with the data points for which the fits have been made. Circles are for Peeters and Sandham [19], squares are for MacDonald et al. [46].

To judge the quality of the fitted equations, the coefficient of determination (R^2) and the root mean square error ($RMSE$) have been calculated. The coefficient of determination can be calculated using Equation 5.8, in which SS_{res} is the residual sum of squares and SS_{tot} the total sum of squares. They can be calculated using Equations 5.9 and 5.10 respectively. In these equations is $\mathcal{G}_{CFD,i}$ the found value of $\mathcal{G}$ at index i, $\mathcal{G}_{fit,i}$ the value for $\mathcal{G}$ according to the fitted equation and $\overline{\mathcal{G}_{CFD}}$ the average value of the found values of $\mathcal{G}$. A R^2 close to 1 would indicate a good fit. The root mean square error can be calculated using Equation 5.11. A lower $RMSE$ would indicate a better fit. For the fitted functions, the values for R^2 and $RMSE$ can be found in Table 5.1.

$$R^2 = 1 - \frac{SS_{res}}{SS_{tot}} \tag{5.8}$$

$$SS_{res} = \sum_{i=1}^{n} \left((\mathcal{G}_{fit,i} - \mathcal{G}_{CFD,i})^2 \right) \tag{5.9}$$

$$SS_{tot} = \sum_{i=1}^{n} \left(\mathcal{G}_{CFD,i} - \overline{\mathcal{G}_{CFD}} \right) \tag{5.10}$$

$$RMSE = \sqrt{\sum_{i=1}^{n} \frac{(\mathcal{G}_{fit,i} - \mathcal{G}_{CFD,i})^2}{n}} \tag{5.11}$$

Table 5.1: Coefficient of determination and root mean square error of the fitted equations found for the damping function.

fit	R^2	$RMSE$
$\mathcal{G}_{1.0}\left(\frac{\Delta y^+}{k^+}\right)$	0.9712	0.0535
$\mathcal{G}_{1.0}\left(\frac{\Delta y^+}{k_s^+}\right)$	0.9712	0.0535
$\mathcal{G}_{0.7}\left(\frac{\Delta y^+}{k^+}\right)$	0.9954	0.0502
$\mathcal{G}_{0.7}\left(\frac{\Delta y^+}{k_s^+}\right)$	0.9954	0.0502

5.5. Validation new damping function

With the calibrated damping functions, the same cases have been validated in the same way as has been done in Chapter 4. The results will be shown without the cases where $\Delta y^+ < 12$. It is clear that in these cases the momentum prediction fails and the shift in velocity is therefore inaccurate. As a consequence the results for the temperature shift are inaccurate as well, because these results are connected to each other.

Results are only shown for the damping functions where it was assumed that $k_s^+ = k^+$ for the channel case from MacDonald et al. [46]. When the less accurate value for prediction the velocity shift has been used ($k_s^+ = 4.1k^+$ and $C_s = 0.253$), the difference was negligible. The difference between the damping functions $\mathcal{G} = f(\Delta y^+/k^+)$ and $\mathcal{G} = f(\Delta y^+/k_s^+)$ for the Peeters and Sandham [19] case was negligible as well.

5.5.1. Irregular roughness

In Figure 5.10 the results for the Peeters and Sandham [19] channel flow can be found. It can be seen that the under prediction of the temperature shift, for the meshes where N was 1, 2 and 3, has been greatly reduced. For the smallest roughness height, $k^+ = 15$, there is still a significant over prediction of around 70 %. For the mesh where $\Delta y^+ = k^+/2$, there is an over prediction for $k^+ = 30$. This was however expected because the calibrated damping function has been made without taking into account the smaller roughness heights. The most spread can be found for $k^+ = 60$, which can also be explained by looking at the fit in Figure 5.9. The fit is the least accurate for $k^+ = 60$. In general the mesh sensitivity has been significantly reduced for all meshes.

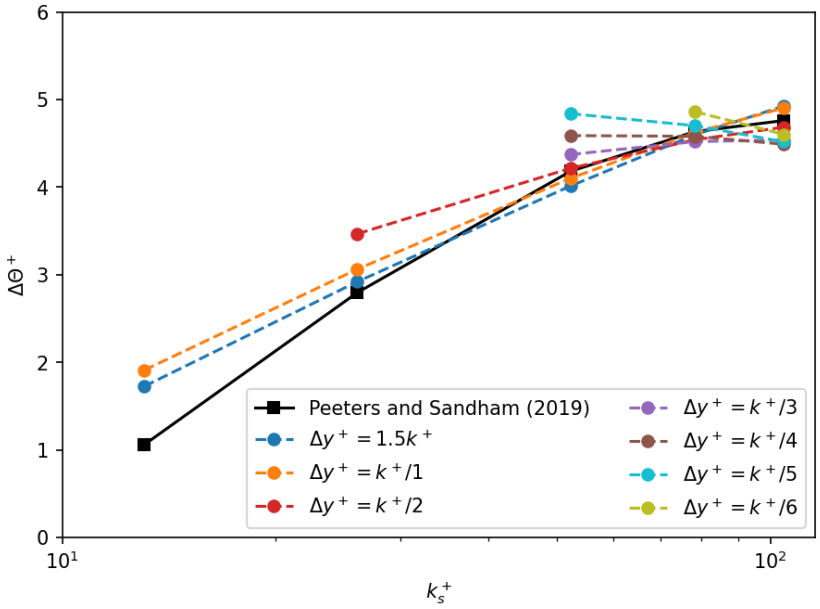

Figure 5.10: Temperature shift prediction for the Peeters and Sandham [19] case. Simulations where $\Delta y^+ < 12$ have been removed for clarity because it has been found that the velocity shift prediction fails when this criterion is met.

5.5.2. Regular roughness

In Figure 5.11 the results for MacDonald et al. [46] channel flow are shown. It can be seen that the temperature shift is still over predicted for the two smaller roughness heights, which is around 35 % for $k^+ = 11.0$ and $k^+ = 21.9$. This was however expected because the calibrated damping function has been made without taking into account the smaller roughness heights. The spread in $\Delta\Theta^+$ between meshes is less compared to the previous case. Only for $k^+ = 93.3$ the spread is more severe. In general the mesh sensitivity has been significantly reduced and accuracy has been improved for all meshes.

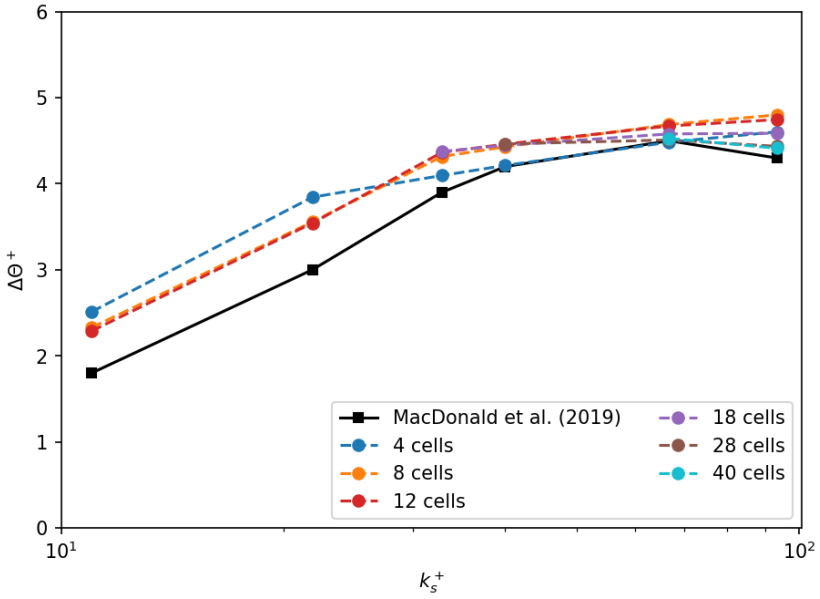

Figure 5.11: Temperature shift prediction for the MacDonald et al. [46] case. Simulations where $\Delta y^+ < 12$ have been removed for clarity because it has been found that the velocity shift prediction fails when this criterion is met. Cells in the legend means the number of cells in the y-direction in the channel half-height. It was inconvenient to scale the cell size with the roughness as has been done for the Peeters and Sandham [19] case.

5.6. Conclusion

In the previous chapter it has been found that the original damping function does not function properly when the model from Aupoix [5] is applied in the wall adjacent cell only on a HRN mesh. In this chapter, new damping functions have been found when the golden section search was applied on the two cases with different molecular Prandtl numbers from Peeters and Sandham [19] and MacDonald et al. [46]. For every roughness height and multiple mesh sizes, the correct value of $\mathcal{G}$ which corresponds to the shift in the temperature profile from the reference DNS data has been found.

After the calibration, it was seen that small roughness heights, $k^+ \leq 30$, deviated from trends. This can possibly be explained by the impact of the roughness on the flow and heat transfer. For the thermal correction model it is assumed that the roughness is fully rough, as explained in Chapter 2. When it is assumed that $k_{s,rough} = 70$ [26], most of the roughness heights are located in the transitionally rough regime. The smaller roughness heights are on the lower side of this regime, indicating roughness effects are less severe compared to the other roughness heights in the upper side of the regime. Therefore, these smaller roughness heights were neglected when the fits were defined.

For the fitted equations it has been chosen to use an equation in the form of $\mathcal{G} = ax^b + c$. In this equation x was either $\Delta y^+/k^+$ or $\Delta y^+/k_s^+$ because the data was well described using both normalizations. Because both cases were simulated with a different molecular Prandtl number, separate fits have been made for each. Therefore, four separate fitting equations have been made which all showed satisfactory values for the coefficient of determination and root mean square error.

Especially for the MacDonald et al. [46] case, the difference between the roughness height and equivalent sand grain height was significant. This resulted in a large difference between the fits for $\Delta y^+/k^+$ and $\Delta y^+/k_s^+$. It is however not difficult to swap between the two function by substituting $k_s^+ = 4.1k^+$. When these fits are compared to their counterpart fits from Peeters and Sandham [19], it is expected that the fit which is a function of k_s^+ will outperform the other. This expectation comes from the given that the original thermal correction model from Aupoix [5] has been made for fluid with a Prandtl number similar to that of air. This means that when the fluid has a higher Prandtl number, there should be extra damping of the heat transfer to compensate. This can be done with the turbulent Prandtl number. A higher turbulent Prandtl number can be seen for the fits where the value of $\mathcal{G}$ is a function of the equivalent sand grain height for $Pr = 1.0$.

When the damping function were tested on the same cases as in Chapter 4, it has been found that the mesh size dependency and accuracy has been significantly reduced and improved, respectively. The difference between these results for the two damping functions for each Prandtl number was minor, because next to the difference in damping functions, also the assumed k_s^+ altered and so the adjustments cancelled each other out.

To further test the new damping functions and determine whether using the roughness- or equivalent sand grain height is the most accurate approach, a developing boundary layer flow over a flat plate has been studied and the results are shown in the next chapter.

6

Testing the Modification

The calibrated damping function has been tested on a boundary layer flow over a flat plate. In this chapter the experimental reference data is shown together with the set-up of the simulations. Finally, the results are presented with conclusions about the performance of the calibrated damping function.

6.1. Introduction

6.1.1. Damping function

The new damping functions have been validated on a new case together with results from the original LRN model of Aupoix [5]. The original LRN model has been made for fluids with a Prandtl number of 0.71 because it was designed with CFD data where air was the flow medium. The new damping functions are made for a Prandtl number of 0.7 and 1.0. Therefore, the damping functions for $Pr = 0.7$ have been tested as the Prandtl number is close to that of air. No extra data has been found for $Pr = 1.0$ and thus the new damping function for that Prandtl number has not been tested. However, because the difference between the two fits for $Pr = 0.7$ is more significant compared to those of $Pr = 1.0$, it is more important to identify whether the correct approach would be to scale with k^+ or k_s^+ for this Prandtl number.

6.1.2. Reference experiments

The LRN model from Aupoix [5] has been validated with the use of several experiments. The common factor of these papers is that they studied a developing boundary layer over a flat plate with roughness elements. One of those experiments has been recreated in OpenFOAM to test the new damping function. The decision of which experiment has been used, is explained shortly in this section.
The first experiments come from Dukhan et al. [63]. In these experiments flow over several ice shapes have been studied. The k_s^+ values of the roughness varied between 400, 4000 and 6000. Keeping in mind the range of k_s^+ in which the damping function has been calibrated, this deemed too large. The second set of experiments is from Hosni et al. [71, 78]. In these experiments flow over truncated cones, which were placed multiple diameters apart, have been studied. The equivalent sand grain height was about 300 and is also too large compared to the calibration range for k_s^+. The third set of experiments is from Healzer et al. [65]. In these experiments flow over copper spheres, brazed together in their most closely packed form, have been studied. The k_s^+ value was approximately 200, which is still larger than the calibration range. The fourth and last experiment is from Coleman et al. [79]. In this experiment an accelerating flow over most closely packed spheres with a smooth entry length has been studied. The equivalent sand grain height was estimated to be 100, which is in the desired roughness height range. Because the case from Coleman et al. [79] uses a roughness with $k_s^+ \approx 100$, it would be logical to use these experiments to validate the calibrated damping function. However, the accelerating flow and smooth entry length introduces complexities and new variables. Therefore, it has been decided to test the new damping function on the case from Healzer et al. [65] as the roughness height of the experiment is the smallest after the experiment from Coleman et al. [79].

6.2. Experimental set up

In the experiments from Healzer et al. [65], different flows over copper spheres with a diameter of 0.05 inch (1.27 mm) have been studied in a wind tunnel. The main goal of the experiments was to study the effect of cross wind on the heat transfer, which was done by blowing air between the gaps of the copper balls perpendicular to the flow direction. The air speed of the cross flow has been varied and was also set to 0 to create a reference case for a flow over a flat plate. The results where there was no cross flow have been used.
The copper spheres were brazed together in their most densely packed configuration on a 20 by 96 inch plate (50.8 by 243.84 cm). It is assumed that this was a hexagon arrangement, which can be seen in Figure 6.1. It is furthermore assumed that due to the scale difference between the copper spheres and the plate, effects of the surface edge in the geometry can be neglected when calculating the corrected surface ratio. The corrected surface ratio was calculated to be 1.1402, which is slightly smaller than the computed value of 1.1418 by Aupoix [5]. The calculation of the corrected surface ratio is explained in section 4.3.2. The convergence of the calculated corrected surface ratio can be seen in Figure 6.2.

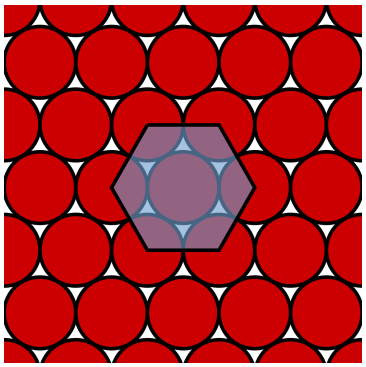

Figure 6.1: Hexagon arrangement of circle packing [80].

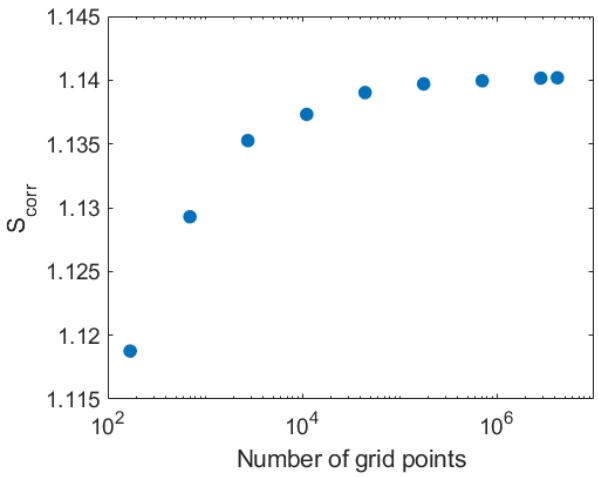

Figure 6.2: The calculated corrected surface as a function of the number of grid points. It can be seen that the value converged to 1.1402, which is slightly smaller than the given value of 1.1418 by Aupoix [5].

Because the spheres are so closely packed, they act as semi-spheres and so the equivalent sand grain height is linked to the radius [65, 5]. Healzer et al. [65] stated that $k_s = 0.07874$ mm and thus $k_s = 1.24r$ in which r is the radius of the spheres. This value deviates from the value Aupoix [5] used in his paper, which is $k_s = 1.25r$ (a diameter instead of a radius is mentioned in Aupoix [5], which is believed to be a typo). The surface roughness in the shape of semi-spheres can be seen in Figure 6.3. The rough surface in which roughness below the meltdown height is neglected can be seen in Figure 6.4.

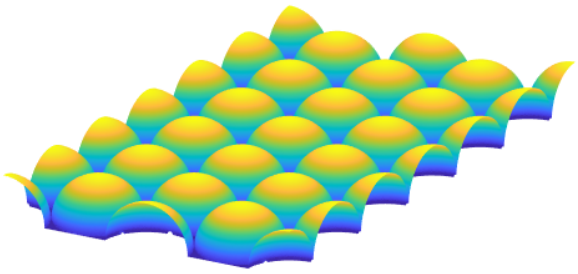

Figure 6.3: Semi-spheres in their most densely packed configuration.

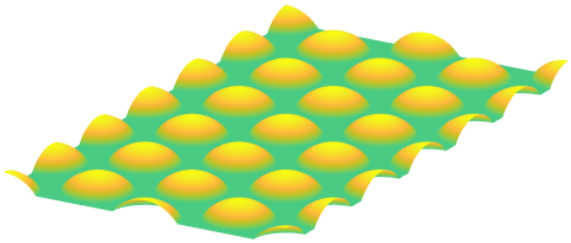

Figure 6.4: Semi-spheres in their most densely packed configuration without roughness below the meltdown height.

The flow velocity of the experiment was fixed at 242 ft/s (73.8 m/s). The temperature of the copper spheres was controlled and fixed to a constant temperature. The pressure was equal to the atmospheric pressure and the temperature was equal to the room temperature. The height of the wind tunnel test section was equal to 4 inch (101.6 mm).

6.3. OpenFOAM set up

The implementation of the experiment from Healzer et al. [65] in OpenFOAM is explained in this section. A schematic overview of the computational domain with boundary conditions can be seen in Figure 6.5. As immediately can be noted, the computational domain is slightly larger than the experimental test section. The inlet is elongated by $1/5$th the test section length because entry effect and convergence problems occurred when solving the simulations on relatively coarse meshes and these problems were less severe with this addition. To minimize the effect of this extra inlet region, the boundary conditions are a slip wall and a constant temperature equal to the inlet temperature. The height and length of the test section are equal to the dimensions of the experiment.
The temperature at the inlet was equal to the room temperature and is assumed to be 293K. The top wall at the test section is assumed to be isolated perfectly, so a zero gradient boundary condition for the temperature has been used. The inlet velocity has been set to 73.8 m/s and a no slip boundary condition has been used at the bottom wall of the test section area. The turbulent Prandtl number has been set to 0.89, which is equal to the value of Aupoix [5] for the LRN number simulations. To determine the velocity shift, a value of 0.253 for C_s has been assumed because it gave accurate predictions before for both cases at larger roughness heights.

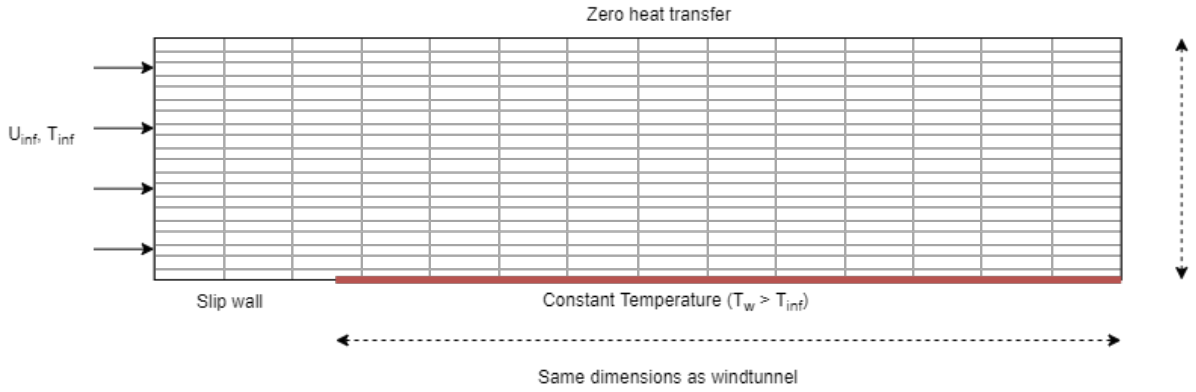

Figure 6.5: Schematic overview of the computational domain with a small inlet and accompanying boundary conditions.

The Stanton number has been calculated using Equation 6.1. In this equation, h is the heat transfer coefficient which is calculated from the heat transfer at the wall using Equation 6.2. In this equation, q_w is the heat transfer at the wall, T_w the temperature at the wall and T_∞ the free stream temperature. The boundary condition of the bottom wall is a fixed constant temperature. The choice of T_w should not matter when computing the Stanton number, because h is in theory not a function of the temperature difference when fluid properties are kept constant. It has however been found in OpenFOAM that for

lower temperature differences, the heat transfer coefficient is affected by the temperature difference after all. With an increasing difference between T_w and T_∞, the temperature dependency disappeared and an asymptote was reached. This occurred at a temperature of 500K and has therefore been used as the fixed wall temperature.

$$St_x = \frac{h\,(x)}{\rho C_p U} \tag{6.1}$$

$$q_w(x) = h(x)(T_w - T_\infty) \tag{6.2}$$

Finally, for the cyclic channel cases from the earlier chapters, the initial value for the turbulent kinetic energy was not important. It is however important for the boundary layer case because the outlet from the wind tunnel has a non-zero amount of turbulent kinetic energy and the flow is not circulated in the computational domain. An estimate for this value can be given as an intensity level, defined in Equation 6.3.

$$I = \frac{u'}{U} \tag{6.3}$$

The turbulent kinetic energy intensity level is estimated to be well below 1% for a high-end wind tunnel nozzle [81]. Because the experiment stems from 1974, a conservative estimate of 1% has been used. In OpenFOAM, a value for the turbulent kinetic energy at the inlet of the computational domain must be given, which can be computed from the turbulent kinetic energy intensity level and equations 6.4 and 6.5. In these equations, I is the turbulence intensity, u' the root-mean-square of the turbulent velocity fluctuations and U the mean free stream velocity. Subscripts indicate a specific direction of the velocity components.

$$u' = \sqrt{\frac{1}{3}\left(u_x'^2 + u_y'^2 + u_z'^2\right)} = \sqrt{\frac{2}{3}k} \tag{6.4}$$

$$U = \sqrt{U_x^2 + U_y^2 + U_z^2} \tag{6.5}$$

To compute the turbulent kinetic energy dissipation ϵ, Equation 6.6 has been used. In this equation, $C_\mu = 0.09$ and L is a length scale assumed to be the length of the plate. The turbulent kinetic energy and dissipation are calculated to be 0.817 m^2/s^2 and 0.0277 m^2/s^3 respectively.

$$\epsilon = \frac{C_\mu k^{\frac{3}{2}}}{L} \tag{6.6}$$

6.4. Results

In this section the results are presented and have been divided in three parts. The first part will show a comparison between the two different damping functions for $Pr = 0.7$ found in the previous chapter. The most accurate damping function has been chosen to be studied more in depth. The second part compares the results from the new damping function with the Reynolds analogy on both a smooth and rough wall. The third and last part compares the results of the new damping function on several mesh sizes with the original damping function on a HRN grid to show the difference in mesh size dependency. All of the comparisons include the results from the experiment of Healzer et al. [65] and the LRN solution of Aupoix [5] as a reference.
The plate length has been expressed in a local Reynolds number Re_x. The local Reynolds number has been calculated using Equation 6.7 in which x is the position at the plate in meters.

$$Re_x = \frac{\rho U_\infty x}{\mu} \tag{6.7}$$

6.4.1. Comparison new damping functions

Before showing the results for the two damping functions, the assumption of $k_s^+ = k^+$ for the MacDonald [46] case has to be recalled (see section 4.5.2). To validate this assumption two damping functions have been made, one as function of k_s^+ and one as function of k^+. This assumption has been tested in this comparison.

In Figure 6.6 the comparison between the two calibrated damping functions for $Pr = 0.7$ can be found. The results were obtained with a mesh consisting of 30 cells in the y-direction, which resulted in a Δy^+ of the wall adjacent cell of 419.2, see mesh 3 in Table 6.1. The entry region is clearly visible by the rapid increase of the Stanton number for $Re_x \lessapprox 0.15 \times 10^7$, followed by a decreasing value which is due to an increasing thickness of the thermal boundary layer. For $Re_x \gtrapprox 0.5 \times 10^7$, the solutions from the damping function for k_s^+, Healzer et al. [65] and Aupoix [5] give the same result. For $Re_x \lessapprox 0.5 \times 10^7$, the LRN solution from Aupoix is less accurate compared to $\mathcal{G} = f(\Delta y^+/k_s^+)$. Overall the damping function for k_s^+ is more accurate compared to the damping function for k^+. The damping function as a function of $\Delta y^+/k^+$ shows an over prediction of the reduction in heat transfer, although the absolute error is still small for a HRN RANS prediction. It has been decided to continue testing with the damping function which is a function of $\Delta y^+/k_s^+$.

Therefore, the assumption of $k_s^+ = k^+$ for the MacDonald [46] case is most likely not valid and assuming $k_s^+ = 4.1k^+$ would be the correct approach after all. This does not alter the outcome of the previous chapters significantly, because in section 4.5.2 it has been shown that when it was assumed that $C_s = 0.253$, for larger roughness heights, the velocity shift is predicted accurately.

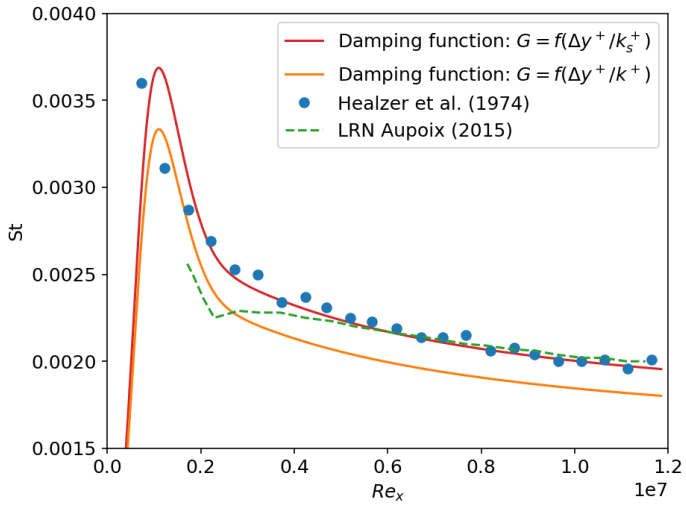

Figure 6.6: Stanton number as a function of the non-dimensional plate length Re_x. In this graph the damping functions for $Pr = 0.7$ can be seen together with results from Healzer et al. [65] and Aupoix [5]. The Δy^+ value of the wall adjacent cell is 419.2 for the HRN simulations. It is assumed that $\Delta y^+ \leq 1$ for Aupoix [5], because it was a LRN mesh.

6.4.2. Comparison smooth and rough wall

Before the comparison between the calibrated damping function and original damping function on a HRN grid and the LRN solution from Aupoix [5] is shown, first the difference between the solutions for a smooth and rough wall using the Reynolds analogy is discussed. In Figures 6.7 and 6.8 these results can be seen for the Stanton number and skin friction, respectively. The skin friction is calculated using Equation 2.8. It can be seen from the olive colored line that both the Stanton number and skin friction are lower along the whole plate, which was expected for the flow over a smooth wall. It was also expected that the Reynolds analogy on a rough surface over predicts the heat transfer. The over prediction can indeed be seen when looking at the teal line. As a visual tool to show that the calibrated damping function indeed reduces the heat transfer compared to the Reynolds analogy on a rough surface, this solution is included as well.

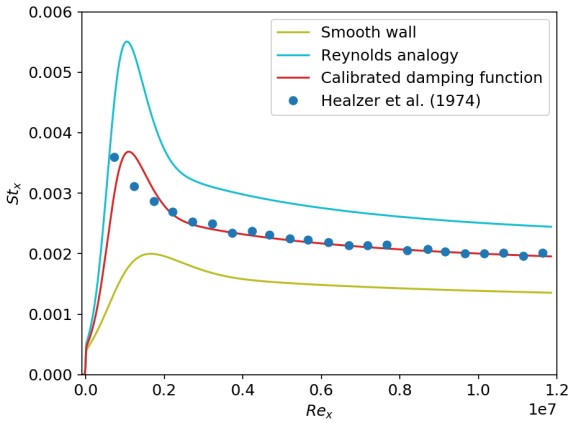

Figure 6.7: Stanton number as a function of the non-dimensional plate length Re_x. The over prediction of the Reynolds analogy for a rough wall can clearly be seen. The Δy^+ value of the wall adjacent cell is 419.2 for the three HRN simulations.

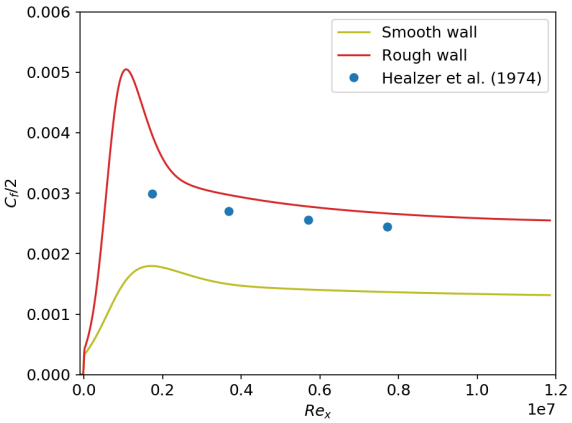

Figure 6.8: Skin friction as a function of the non-dimensional plate length Re_x. The over prediction of the Reynolds analogy for a rough wall can clearly be seen. The Δy^+ value of the wall adjacent cell is 419.2 for the two HRN simulations.

6.4.3. Comparison new and original damping function

The original and new damping function have been tested on several grid sizes varying from $\Delta y^+ = 786.2$ to 16.5. This resulted in a ratio for $\Delta y^+/k_s^+$ of 4.05 to 0.08, indicating a wide range for both the mesh size and ratio of the mesh size and roughness height. The results of both damping functions have been compared with the experiment form Healzer et al. [65] and the LRN results from Aupoix [5].

The meshes were composed of uniformly distributed cells in both the x- and y-direction, except for the mesh where Δy^+ of the wall adjacent cell was 16.5. In that mesh the ratio between the largest (at the channel half-height) and smallest cell (at the wall) was set to 20 (R_y). The cell expansion ratio was therefore approximately 1.02. This made sure that the computational time stayed within reasonable limits for a steady state RANS simulation because less cells were required to obtain a finer mesh at the wall. The number of cells in the x-direction was defined as 30 and 6 times the number of cells in the y-direction of the channel half height for the test section and inlet region respectively.

An overview of the different meshes used can be seen in Table 6.1. In this table the amount of cells in the channel half-height and ratio of the largest and smallest cell has been given which resulted in a certain Δy^+ at the wall adjacent cell.

Table 6.1: Overview of the different meshes used in the HRN simulations to compare the skin friction and Stanton number. Δy^+ is the defined as the distance from the wall to the center of the adjacent cell. The width of the cell is therefore $2\Delta y^+$. Δx^+ is the defined as the distance from the inlet to the center of the adjacent cell. The width of the cell is therefore $2\Delta x^+$. R_y and R_x are defined as the ratio between the largest and smallest cell size in the y- and x-direction respectively.

	Δy^+ of the wall adjacent cell	Δx^+ of the wall adjacent cell	Number of cells in the y-direction	Number of cells in the x-direction	$R_y (= R_x)$
Mesh 1	786.2	639.0	15	540	1
Mesh 2	609.4	495.3	20	720	1
Mesh 3	419.2	340.7	30	1080	1
Mesh 4	258.0	209.7	50	1800	1
Mesh 5	132.2	107.5	100	3600	1
Mesh 6	16.5	13.4	140	5040	20

Before showing the results for the Stanton number separately for every grid, first an overview is given of the skin friction results for the different mesh sizes. The prediction of the skin friction is important because the calculation of the heat transfer depends on this prediction, which has been shown in Chapter 4. The results for the skin friction is shown in Figure 6.9. Note that the skin friction has been divided by two on the y-axis. In this way it is easier to compare the skin friction to the Stanton number as for the Reynolds analogy it holds that $C_f/2 = St$.

It can be seen that after entry effects, the skin friction is predicted reasonably well for all the different mesh sizes. With a decreasing cell size, the position at which the skin friction follows the trend seen by Healzer et al. [65] and Aupoix [5] shifts to a lower value. This indicates a decrease of these entry effects as the number of cells in the x-direction increases. For the finest mesh, $\Delta y^+ = 16.5$, it can be seen that the skin friction increases rapidly as it approaches $Re_x = 0$. The rapid increase is expected as the skin friction is computed from the wall shear stress and the wall shear stress is computed using the gradient of the velocity at the wall. Because the inlet velocity has an uniform profile of U_∞ and the velocity at the wall is equal to 0, the gradient of $\Delta U/\Delta y$ goes to infinity as Δy goes to 0.
Furthermore, at the end of the plate length, the momentum boundary layer is developed further compared to the experimental and LRN simulation results. The boundary layer is almost fully developed. This can be seen by the small gradient of the skin friction, which is close to 0. Especially for the LRN simulation, it can be seen that the gradient is non-zero, indicating a undeveloped boundary layer.
At last, in the experimental results, no rapid increase of the skin friction has been observed at the location of the measurement point closest to the inlet. For the LRN simulation of Aupoix [5] the rapid increase can been seen with a sudden bend and is not as smooth as the HRN results.

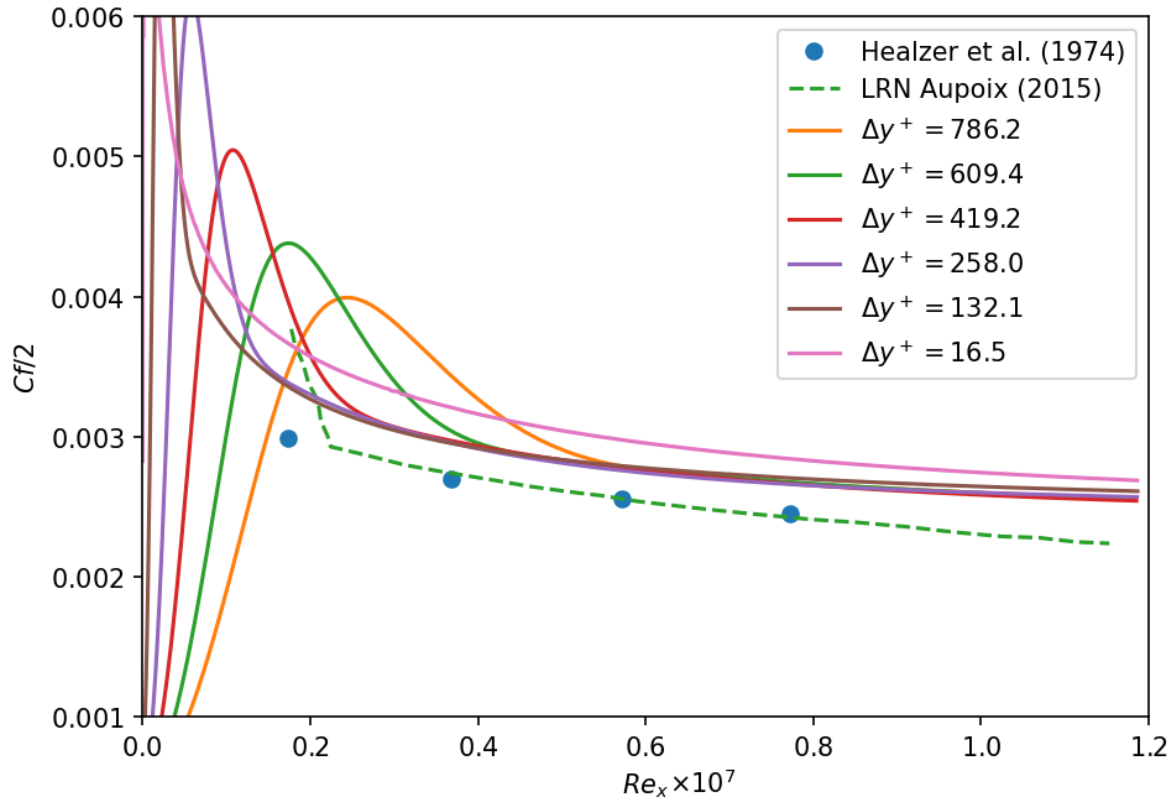

Figure 6.9: Skin friction results from the experiment of Healzer et al. [65], LRN simulation of Aupoix [5] and HRN results for different mesh sizes.

In Figure 6.10 the Stanton number results of the original damping function can be seen. Also for the Stanton number entry effects are visible, which could already be seen from the skin friction. The entry effects become less as the mesh becomes finer. Starting at $\Delta y^+ = 786.2$, it can be seen that the Stanton number is over predicted the most. As the mesh becomes finer, a minimum can be seen for $\Delta y^+ = 132.1$ indicating that with a finer mesh, a lower value for the Stanton number is calculated. In Chapter 4 it was noticed that at a certain mesh size, the temperature shift started to increase again. This can also be seen for the finest mesh, mesh 6. For this simulation the Stanton number is once more over predicted, albeit less severely compared to the three coarsest meshes. Even though the results do not overlap, they have in common that they more or less predict the same boundary layer developing speed at the end of the plate, which can be seen from the gradients.

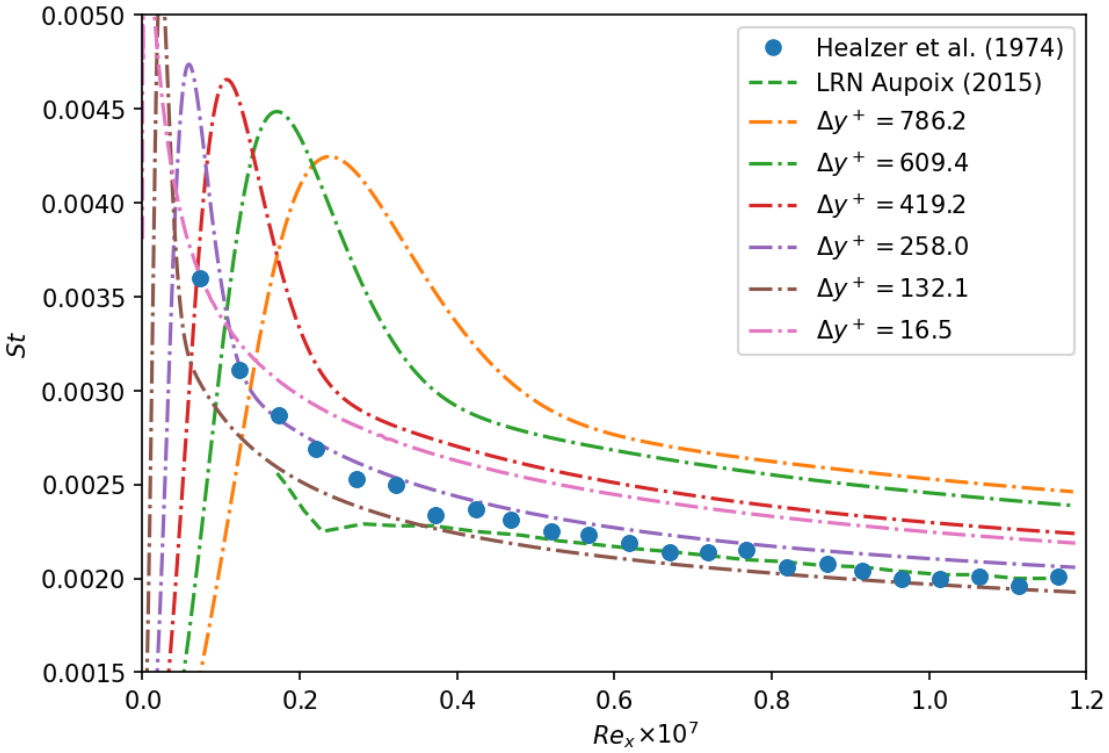

Figure 6.10: Stanton number results from the experiment of Healzer et al. [65], LRN simulation of Aupoix [5] and HRN results using the original damping function for different mesh sizes. The mesh size dependency is clearly visible.

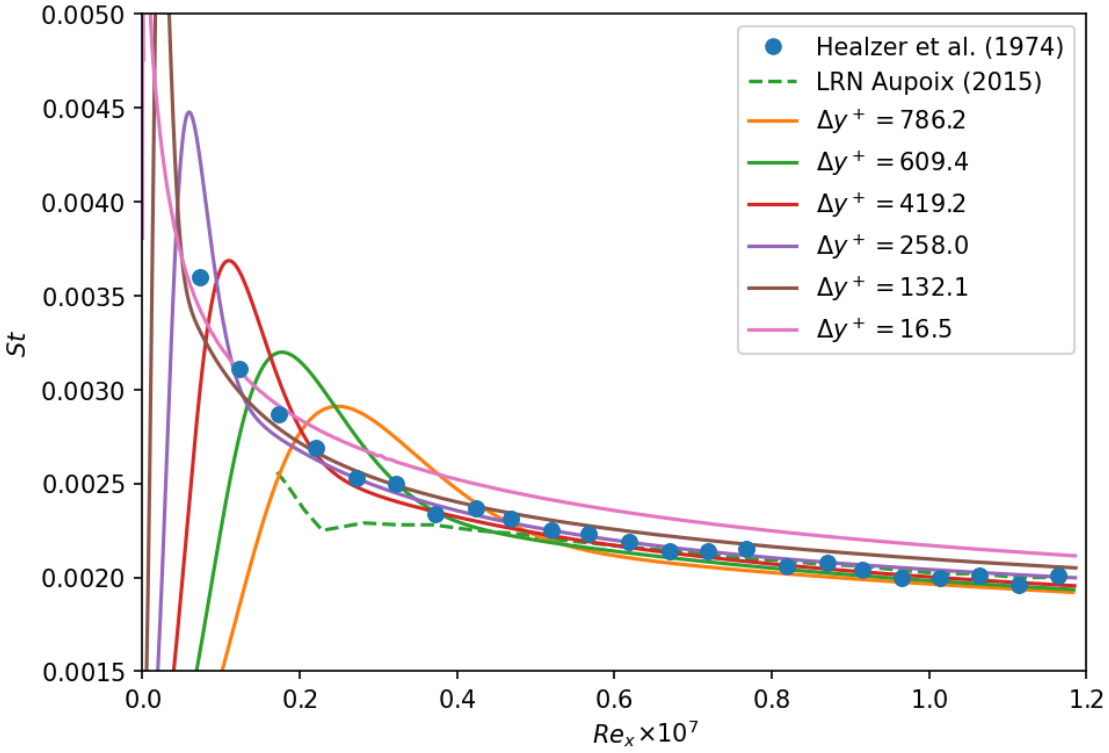

Figure 6.11: Stanton number results from the experiment of Healzer et al. [65], LRN simulation of Aupoix [5] and HRN results using the calibrated damping function for different mesh sizes. The mesh size dependency has been greatly reduced with the calibrated damping function.

In Figure 6.11 the Stanton number results of the calibrated damping function can be seen. The entry effects due to the mesh size are once more visible in this graph. When Figure 6.11 is compared with Figure 6.10, it can be seen that the mesh size dependency has been greatly reduced. There is little spread of the Stanton number prediction for $Re_x \geq 0.4 \times 10^7$. The only solution that stands a little out, is the solution for mesh 6 ($\Delta y^+ = 16.5$). The heat transfer is slightly over predicted and does not follow the same trend as the other meshes at the inlet region; the chance from a large negative gradient towards a lower negative gradient occurs a little earlier.

6.5. Conclusions

In this chapter the calibrated damping functions for $Pr = 0.7$ have been tested on a developing boundary layer flow over a rough surface where $Pr = 0.71$. It was extra important to test the two damping functions for $Pr = 0.7$ because for this new case, the introduced errors would not cancel out with if the assumption of $k_s^+ = k^+$ was wrong. It turned out that this assumption was indeed wrong and that therefore the damping function $\mathcal{G}_{Pr=0.7} = f(\Delta y^+/k_s^+)$ gave the most accurate predictions. So this damping function was used to study the effect of the mesh size on the Stanton number.
Furthermore, the over prediction of the heat transfer when the Reynolds analogy without thermal correction model is used was confirmed. The case without roughness model, or assuming a smooth wall, was shown as well to see the under prediction of the skin friction and Stanton number.

6.5.1. Skin friction

The skin friction was predicted within tolerances which can be expected from RANS computations for the different meshes. After a certain length, the values of the skin friction were equal to each other. Before that length, entry effects were visible. For finer meshes this entry length became shorter, which is probably caused by a smaller Δx^+ for these meshes because the number of cells in the x-direction scaled with the number of cells in the y-direction.
A small deviation however has been found for the mesh where $\Delta y^+ = 16.5$. The skin friction was larger across the whole plate length compared to the other meshes. Two causes have been identified for this anomaly. The first possibility concerns the ratio between the coarsest and finest cell in the y-direction. It is the only mesh without an equilateral grid. The ratio between the largest and smallest cell was 20 instead of 1. The cell expansion ratio in the y-direction was however only 1.02, which is well within guidelines, so it seems peculiar this would be the reason. The second possibility, which is more plausible, has to do with the small cell size. With $\Delta y^+ = 16.5$ it means the wall adjacent cell center is placed within the buffer layer. In Chapter 4 it has been shown that the momentum prediction fails when $\Delta y^+ < 12$. This could mean, because 16.5 is close to that boundary, the accuracy of the momentum prediction already started to decline.
Furthermore, from the gradients of the skin friction could be seen that the pace at which the momentum boundary layer developed, was smaller compared to the experiment and LRN simulation; indicating an almost developed boundary layer for the HRN simulations.
The transition from a larger negative gradient towards a smaller negative gradient of the skin friction was more gradually compared to the LRN simulation from Aupoix [5], where a sudden bend could be observed. The experiment from Healzer et al. [65] did not show an increase in skin friction at low Re_x values because no measurements were taken close to the inlet.

6.5.2. Stanton number

Also for the Stanton number entry effects were visible and they were also more severe for the coarser meshes. It was expected these entry effects were present, because in OpenFOAM the Stanton number has been calculated from the skin friction (with a thermal correction). The thermal boundary layer developing speed was however different compared to that of the momentum boundary layer. The developing speed of the thermal correction model was similar to that of the experiment and LRN simulation until the end of the plate.
The LRN simulations from Aupoix [5] showed again a sharp bend at $Re_x \approx 0.2 \times 10^7$, which was not confirmed by the experiment from Healzer et al. [65]. For the Stanton number, more measurement points have been used. Therefore the gradually increasing value of the Stanton number at the inlet of the plate could clearly be seen. The finer meshes used for the HRN simulations captured the increase of the Stanton number at the inlet well.

Finally, the goal of reducing the mesh size dependency of the thermal correction model of Aupoix [5] on a High Reynolds Number grid has been achieved. The influence of the mesh size on the results for the heat transfer has been greatly reduced with the calibrated damping function. The Stanton number was predicted accurately for a wide range of mesh sizes, both in absolute (Δy^+) and relative ($\Delta y^+/k_s^+$) value.
For the original damping function, the prediction of the Stanton number was comparable to that of the calibrated damping function when $\Delta y^+ \leq 258$. However, the influence of the mesh size on the results was still more present for this range.

7

Conclusions and Recommendations

7.1. Conclusions

In this thesis, heat transfer calculations using RANS for flows over a rough wall have been improved. It has been verified that the Reynolds analogy over predicts the heat transfer and that a correction is required. A model from Aupoix [5] gave accurate predictions for Low Reynolds Number (LRN) meshes, i.e. a mesh where the flow is resolved up to the viscous sub layer ($\Delta y^+ < 1$). However, this approach can become too computationally expensive as the Reynolds number of the flow increases. Thus a model which gives accurate results on a High Reynolds Number (HRN) mesh, i.e. a mesh where the flow is resolved up to the log layer ($\Delta y^+ > 30$), is required for industrial scale simulations. On a HRN mesh, the wall shear stress and heat transfer are computed using wall functions.

The thermal correction model has been implemented as a wall function and was tested on various HRN meshes for two different channel flow cases. It has been shown that for both cases the temperature shift was not predicted accurately and that the results were indeed dependent on the mesh size. This was expected due to the input parameters of the damping function from the thermal correction model when calculating the correction on the turbulent Prandtl number.

Because the mesh size dependency originated from the damping function, new functions have been made for the two cases with different molecular Prandtl numbers. The suggested improvement, which took the form of a modified damping function, yielded improved results on the same cases and showed a significant improved in both accuracy and mesh size dependency.

To test the performance of the newly found damping function on a new case and make sure the model can be applied in various types of flow, the calibrated damping functions have been tested on a new case as well.

Because no new case has been found for $Pr = 1$, only the damping function for $Pr = 0.7$ has been tested using an experiment of a developing boundary layer over copper spheres from Healzer et al. [65]. The thermal correction model with the calibrated damping function was tested on six different meshes in which Δy^+ varied from 786.2 to 16.5. The calibrated damping function outperformed the original damping function significantly for $\Delta y^+ > 258$ for the wall adjacent cell. For $\Delta y^+ < 258$, results were similar but it could be seen that the calibrated damping function was less sensitive on the grid size. The maximum error reduced approximately from 62% to 16% for $Re_x < 0.4 \times 10^7$ and from 22% to 9% for $Re_x \geq 0.4 \times 10^7$. This further emphasizes the improvement over the original damping function for computing the heat transfer over rough surfaces on a HRN mesh.

7.2. Recommendations

In its current form, the modified model is however not yet ready to be used in industry. To this end, the following recommendations have been made;

The damping function for a Prandtl number of 0.7 has been extensively tested, which is not the case for the damping function for a Prandtl number of 1.0. It is therefore recommended to find a suitable case to test this damping function as well, because at the moment the new function for $Pr = 1.0$ is only tested on the case on which it was calibrated.

During the validation of the original and new damping functions, it was found that the assumption for the turbulent Prandtl number ($Pr_{t,\infty}$ in Equation 4.4) had influence on the results. This can be explained by looking at the the order of magnitudes of $Pr_{t,\infty}$ and $\Delta Pr_{t,rough}$, which are both around 1. It is therefore important to gain more knowledge about these assumptions for future use of the thermal correction model.
Finally, because DNS data for only two molecular Prandtl numbers have been used, it has been decided to not make a single Prandtl number dependent fit but rather make two separate fits for each Prandtl number. A possibility to improve the quality of the damping function would be to calibrate new damping functions for other Prandtl numbers as well. When data for multiple Prandtl numbers becomes available, it might be possible to combine the data to make a single Prandtl number dependent fit.
Another possibility would be to combine the work from Latini et al. [82] with the principles applied in this thesis. Instead of applying the model from Aupoix [5] on a HRN mesh and modifying the damping function $\mathcal{G}$ (see Equation 4.5), the authors applied the model on a LRN mesh as intended, but altered the function $\mathcal{F}$ to cope with different Prandtl numbers. Only using the model from Latini et al. [82] can significantly limit the applicability as LRN meshes may be infeasible for industrial scale flows. Including this work can overcome this problem.

References

[1] NRG. *Over ons*. URL: https://www.nrg.eu/over-ons (visited on 01/14/2022).

[2] OECD Nuclear Energy Agency. *Handbook on lead-bismuth eutectic alloy and lead properties, materials compatibility, thermal-hydraulics and technologies*. Paris, FR: OECD publications, 2007, p. 91. ISBN: 9789264990029.

[3] J.R. Weeks and A.J. Romano. "Liquidus Curves and Corrosion of Fe, Ti, Zr, and Cu in Liquid Bi-Pb Alloys". In: *National Association of Corrosion Engineers* 25.3 (1969), pp. 131–136.

[4] D.J. Walter, B.K. Kendrick, V. Petrov, A. Manera, B. Collins, and T. Downar. "Proof-of-principle of high-fidelity coupled CRUD deposition and cycle depletion simulation". In: *Annals of Nuclear Energy* 85 (Nov. 2015), pp. 1152–1166. ISSN: 18732100. DOI: 10.1016/j.anucene.2015.07.034.

[5] B. Aupoix. "Improved heat transfer predictions on rough surfaces". In: *International Journal of Heat and Fluid Flow* 56 (2015), pp. 160–171. ISSN: 0142727X. DOI: 10.1016/j.ijheatfluidflow.2015.07.007.

[6] H.S. Dou. *Energy Gradient Theory of Hydrodynamic Instability*. Tech. rep. SG, 2005. URL: https://www.researchgate.net/publication/2147222.

[7] P.K Kundu, I.M Cohen, and Dowling D.R. *Fluid Mechanics*. Elsevier, 2016, pp. 412–419, 648–650. ISBN: 9780124059351.

[8] A.A. Townsend. *The Structure of Turbulent Shear Flow*. Cambridge, UK: Cambridge University Press, 1976.

[9] S.B. Pope. *Turbulent Flows*. Cambridge, UK: Cambridge University Press, 2001.

[10] J. Jimenez. "Turbulent flows over rough walls". In: *Annual Review of Fluid Mechanics* 36 (2004), pp. 173–196. ISSN: 00664189. DOI: 10.1146/annurev.fluid.36.050802.122103.

[11] P.A. Durbin and B.A. Pettersson Reif. *Statistical Theory and Modeling for Turbulent Flows, Second Edition*. UK: WILEY, 2010. ISBN: 9780470689318.

[12] F.T.M. Nieuwstadt, B.J. Boersma, and J. Westerweel. *Turbulence: Introduction to Theory and Applications of Turbulent Flows*. SW: Springer, 2016. ISBN: 978-3-319-31597-3. DOI: 10.1007/978-3-319-31599-7.

[13] M. Kadivar, D. Tormey, and G. McGranaghan. "A review on turbulent flow over rough surfaces: Fundamentals and theories". In: 10 (2021). ISSN: 26662027. DOI: 10.1016/j.ijft.2021.100077.

[14] U. Piomelli. "Recent advances in the numerical simulation of rough-wall boundary layers". In: *Physics and Chemistry of the Earth* 113 (Oct. 2019), pp. 63–72. ISSN: 14747065. DOI: 10.1016/j.pce.2018.10.005.

[15] S. Soleimani and S. Eckels. "A review of drag reduction and heat transfer enhancement by riblet surfaces in closed and open channel flow". In: *International Journal of Thermofluids* 9 (2021). ISSN: 26662027. DOI: 10.1016/j.ijft.2020.100053.

[16] A.F. Mills and C.F.M. Coimbra. *Basic Heat and Mass Transfer*. Temporal publishing, 2015, p. 276. ISBN: 9780996305303.

[17] Reynolds, O. "On the extent and action of the heating surface of steam boilers". In: *Proceedings of the Literary and Philosophical Society of Manchester* 14 (1874).

[18] A. Busse, M. Lützner, and N.D. Sandham. "Direct numerical simulation of turbulent flow over a rough surface based on a surface scan". In: *Computers and Fluids* 116 (2015), pp. 129–147. ISSN: 00457930. DOI: 10.1016/j.compfluid.2015.04.008.

[19] J.W.R. Peeters and N.D. Sandham. “Turbulent heat transfer in channels with irregular roughness”. In: *International Journal of Heat and Mass Transfer* 138 (2019), pp. 454–467. ISSN: 00179310. DOI: 10.1016/j.ijheatmasstransfer.2019.04.013.

[20] B. Zhou, M. Yang, Z. Li, Z. Wang, and Y. Zhang. “Numerical simulations of forced convection across a single tube to evaluate applicability of the DNS, LES and RSM methods”. In: *Applied Thermal Engineering* 123 (2017), pp. 123–130. ISSN: 13594311. DOI: 10.1016/j.applthermaleng.2017.05.055.

[21] W.P. Jones and B.E. Launder. “The Prediction of Laminarization with a Two-Equation Model of Turbulence”. In: *International Journal of Heat and Mass Transfer* 15 (1972), pp. 301–314. URL: https://www.researchgate.net/publication/313117966.

[22] B.E. Launder and D.P. Spalding. “The Prediction of Laminarization with a Two-Equation Model of Turbulence”. In: *Computational Methods in Applied Mechanics and Engineering* 3 (1972), pp. 269–289.

[23] D.C. Wilcox. “Reassessment of the scale-determining equation for advanced turbulence models”. In: *American Institute of Aeronautics and Astronautics* 26.11 (1988), pp. 1299–1310.

[24] F.R. Menter. “Two-Equation Eddy-Viscosity Turbulence Models for Engineering Applications”. In: *AIAA Journal* 32.8 (1994), pp. 1598–1605.

[25] C.F. Colebrook and C.M. White. “Experiments with Fluid Friction in Roughened Pipes”. In: *Proceedings of the Royal Society A* 161 (1937), pp. 367–381. URL: https://royalsocietypublishing-org.tudelft.idm.oclc.org/doi/abs/10.1098/rspa.1937.0150.

[26] J. Nikuradse. “Strömingsgesetze in Rauhen Rohren”. In: (1933).

[27] R.B. Dirling JR. “A method for computing roughwall heat transfer rates on reentry nosetips”. In: *American Institute of Aeronautics and Astronautics 8th Thermophysics Conference* (1973). DOI: 10.2514/6.1973-763.

[28] R.J. Boyle and M. Stripf. “Simplified approach to predicting rough surface transition”. In: *Journal of Turbomachinery* 131.4 (2009), pp. 1–11. ISSN: 0889504X. DOI: 10.1115/1.3072521.

[29] T. Cebeci and P. Bradshaw. *Momentum Transfer in Boundary Layers*. New York, US: McGraw-Hill Book Co, 1977.

[30] M.P. Schultz and K.A. Flack. “Outer layer similarity in fully rough turbulent boundary layers”. In: *Experiments in Fluids* 38 (2005). DOI: http://dx.doi.org/10.1007/s00348-004-0903-2.

[31] F.H. Clauser. “Turbulent Boundary Layers in Adverse Pressure Gradients”. In: *Journal of the Aeronautical Sciences* 21 (1954).

[32] F.M. White. *Viscous Fluid Flow*. New York, US: McGraw-Hill Education, 1991. ISBN: 0-07-069712-4.

[33] K.A. Flack, M.P. Schultz, and T.A. Shapiro. “Experimental support for Townsend’s Reynolds number similarity hypothesis on rough walls”. In: *Physics of Fluids* 17.3 (2005). ISSN: 10706631. DOI: 10.1063/1.1843135.

[34] W.M. Kays and M.E. Crawford. *Convective heat and mass transfer*. New York, US: McGraw-Hill Education, 1993.

[35] D.F. Dipprey and R.H. Sabersky. “Heat and momentum transfer in smooth and rough tubes at various Prandtl numbers”. In: *International Journal of Heat and Mass Transfer* 6 (1963), pp. 329–353.

[36] P.R. Owen and W.R. Thomson. “Heat transfer across rough surfaces”. In: *Journal of Fluid Mechanics* 15 (1963), pp. 321–334. ISSN: 14697645. DOI: 10.1017/S0022112063000288.

[37] H. Darcy. *Recherches expérimentales relatives au mouvement de l’eau dans les Tuyaux*. Paris, FR: Mallet-Bachelier, 1857.

[38] C.F. Colebrook, T. Blench, H. Chatley, E.H. Essex, J.R. Finniecome, G. Lacey, J. Williamson, and G.G. Macdonald. “Turbulent flow in pipes, with particular reference to the transition region between the smooth and rough pipe laws”. In: *Journal of the Institution of Civil Engineers* 11.4 (1939), pp. 133–156. DOI: https://doi-org.tudelft.idm.oclc.org/10.1680/ijoti.1939.13150.

[39] L.F. Moody and N.J. Princeton. “Friction factors for pipe flow”. In: *Transactions of the ASME* 66.8 (1944), pp. 671–684.

[40] Karen A. Flack and Michael P. Schultz. “Roughness effects on wall-bounded turbulent flows”. In: *Physics of Fluids* 26 (2014). ISSN: 10897666. DOI: 10.1063/1.4896280.

[41] M.P. Schultz and K.A. Flack. “Turbulent boundary layers on a systematically varied rough wall”. In: *Physics of Fluids* 21 (2009). ISSN: 10706631. DOI: 10.1063/1.3059630.

[42] A.M. Jacobi and R.K. Shah. “Heat transfer surface enhancement through the use of longitudinal vortices”. In: *Experimental Thermal and Fluid Science* 11 (1995), pp. 295–309.

[43] A. Stroh, K. Schäfer, P. Forooghi, and B. Frohnapfel. “Secondary flow and heat transfer in turbulent flow over streamwise ridges”. In: *International Journal of Heat and Fluid Flow* 81 (2020). ISSN: 0142727X. DOI: 10.1016/j.ijheatfluidflow.2019.108518.

[44] C.K. Stimpson, J.C. Snyder, K.A. Thole, and D. Mongillo. “Roughness effects on flow and heat transfer for additively manufactured channels”. In: *Journal of Turbomachinery* 138 (2016). ISSN: 15288900. DOI: 10.1115/1.4032167.

[45] D. Chung, N. Hutchins, M.P. Schultz, and K.A Flack. “Predicting the Drag of Rough Surfaces”. In: *Annual Review of Fluid Mechanics* 53 (2021), pp. 439–471. DOI: 10.1146/annurev-fluid-062520. URL: https://doi.org/10.1146/annurev-fluid-062520-.

[46] M. MacDonald, N. Hutchins, and D. Chung. “Roughness effects in turbulent forced convection”. In: *Journal of Fluid Mechanics* 861 (2019), pp. 138–162. ISSN: 14697645. DOI: 10.1017/jfm.2018.900.

[47] J. Bons. “A critical assessment of Reynolds analogy for turbine flows”. In: *Journal of Heat Transfer* 127 (2005), pp. 472–485. ISSN: 00221481. DOI: 10.1115/1.1861919.

[48] Z. Hantsis and U. Piomelli. “Roughness effects on scalar transport”. In: *Physical Review Fluids* 5 (2020). ISSN: 2469990X. DOI: 10.1103/PhysRevFluids.5.114607.

[49] T. Knopp. “On grid-independence of RANS predictions for aerodynamic flows using model-consistent universal wall-functions”. In: *European Conference on Computational Fluid Dynamics* (2006).

[50] B. Aupoix and P.R. Spalart. “Extensions of the Spalart - Allmaras turbulence model to account for wall roughness”. In: *International Journal of Heat and Fluid Flow* 24 (2003), pp. 454–462. ISSN: 0142727X. DOI: 10.1016/S0142-727X(03)00043-2.

[51] P.R. Spalart and S.R. Allmaras. “A one-equation turbulence model for aerodynamic flows”. In: *La Recherche Aérospatiale* 1 (1994), pp. 5–21.

[52] B. Aupoix. “Roughness Corrections for the k–ω Shear Stress Transport Model: Status and Proposals”. In: *Journal of Fluids Engineering* 137 (2015). DOI: 10.1115/1.4028122.

[53] D.C. Wilcox. “Reassessment of the scale-determining equation for advanced turbulence models”. In: *American Institute of Aeronautics and Astronautics Inc.* 26.11 (1988), pp. 1299–1310.

[54] T. Knopp, B. Eisfeld, and J.B. Calvo. “A new extension for k-ω turbulence models to account for wall roughness”. In: *International Journal of Heat and Fluid Flow* 30.1 (2009), pp. 54–65. ISSN: 0142727X. DOI: 10.1016/j.ijheatfluidflow.2008.09.009.

[55] W. Ambrosini, A. Pucciarelli, and I. Borroni. “A methodology for including wall roughness effects in k-ϵ low-Reynolds turbulence models: Part I. Basis of the methodology”. In: *Nuclear Engineering and Design* 286 (2015), pp. 175–194. ISSN: 00295493. DOI: 10.1016/j.nucengdes.2015.01.008.

[56] A. Prakash and E. Laurendeau. “Consistent surface roughness extension for wall functions”. In: *International Journal of Heat and Fluid Flow* 82 (2020). ISSN: 0142727X. DOI: 10.1016/j.ijheatfluidflow.2020.108552.

[57] T.J. Craft, A.V. Gerasimov, H. Iacovides, and B.E. Launder. “Progress in the generalization of wall-function treatments”. In: *International Journal of Heat and Fluid Flow* 23 (2002), pp. 148–160.

[58] T.J. Craft, S.E. Gant, H. Iacovides, and B.E. Launder. “A new wall function strategy for complex turbulent flows”. In: *Numerical Heat Transfer, Part B: Fundamentals* 45.4 (2004), pp. 301–318. ISSN: 10407790. DOI: 10.1080/10407790490277931.

[59] K. Suga, T.J. Craft, and H. Iacovides. “An analytical wall-function for turbulent flows and heat transfer over rough walls”. In: *International Journal of Heat and Fluid Flow* 27 (2006), pp. 852–866. ISSN: 0142727X. DOI: 10.1016/j.ijheatfluidflow.2006.03.011.

[60] Y. Nagano, H. Hattori, and T. Houra. “DNS of velocity and thermal fields in turbulent channel flow with transverse-rib roughness”. In: *International Journal of Heat and Fluid Flow* 25 (2004), pp. 393–403. ISSN: 0142727X. DOI: 10.1016/j.ijheatfluidflow.2004.02.011.

[61] M. Olazabal-Loume, F. Danvin, J. Mathiaud, and B. Aupoix. “Study on k-ω shear stress transport model corrections applied to rough wall turbulent hypersonic boundary layers”. In: *7th European Conference for Aeronautics and Space Sciences* (2017). DOI: 10.13009/EUCASS2017-604.

[62] C. Grigson. “Drag Losses of New Ships Caused by Hull Finish”. In: *Journal of Ship Research* 36.2 (1992), pp. 182–196. URL: http://onepetro.org/JSR/article-pdf/36/02/182/2230720/sname-jsr-1992-36-2-182.pdf/1.

[63] N. Dukhan, K.C. Masiulaniec, K.J. De Witt, and G.J. Van Fossen. “Experimental heat transfer coefficients from ice-roughened surfaces for aircraft deicing design”. In: *Journal of Aircraft* 36.6 (1999), pp. 948–956. ISSN: 00218669. DOI: 10.2514/2.2556.

[64] F. Morency and H. Beaugendre. “Comparison of turbulent Prandtl number correction models for the Stanton evaluation over rough surfaces”. In: *International Journal of Computational Fluid Dynamics* 34.4 (2020), pp. 278–298. ISSN: 10290257. DOI: 10.1080/10618562.2020.1753712.

[65] J.M. Healzer, R.J. Moffat, and W.M. Kays. “Turbulent Boundary Layer on a Porous, Rough Plate: Experimental Heat Transfer with Uniform Blowing”. In: *American Society of Mechanical Engineers*. 74 -HT-14. 1974. DOI: 10.2514/6.1974-680.

[66] P.M. Ligrani, R.J. Moffat, and W.M. Kays. *The Thermal and Hydrodynamic Behavior of Thick, Rough-Wall, Turbulent Boundary Layers*. Tech. rep. Stanford University California Thermosciences Division, 1979.

[67] E. Radenac, A. Kontogiannis, C. Bayeux, and P. Villedieu. “An extended rough-wall model for an integral boundary layer model intended for ice accretion calculations”. In: *2018 Atmospheric and Space Environments Conference* (2018).

[68] K. Ignatowicz, F. Morency, and H. Beaugendre. “Sensitivity study of ice accretion simulation to roughness thermal correction model”. In: *Aerospace* 8.84 (2021). ISSN: 22264310. DOI: 10.3390/aerospace8030084.

[69] F. Chedevergne. “Analytical wall function including roughness corrections”. In: *International Journal of Heat and Fluid Flow* 73 (2018), pp. 258–269. ISSN: 0142727X. DOI: 10.1016/j.ijheatfluidflow.2018.08.001.

[70] H. Reichardt. “Vorstallege darstellung der turbulenten geschwindigskeitsverteilung in glatten leitungen”. In: (1951), pp. 208–219.

[71] M.H. Hosni, H.W Coleman, and R.P. Taylor. “Measurements and calculations of rough-wall heat transfer in the turbulent boundary layer”. In: *International Journal of Heat and Mass Transfer* 34.4/5 (1991), pp. 1067–1082.

[72] OpenFOAM Foundation. *User Guide*. URL: https://doc.cfd.direct/openfoam/user-guide-v10/index (visited on 08/23/2022).

[73] V. Habiyaremye. “Modeling of bubble coalescence and break-up: Comparing population balance and closure models”. In: *MSc. thesis* (2021).

[74] H.K. Versteeg and W. Malalasekera. *An Introduction to Computational Fluid Dynamics Second Edition*. 2007. URL: www.pearsoned.co.uk/versteeg.

[75] OpenFOAM. *OpenFOAM code*. URL: https://github.com/OpenFOAM/OpenFOAM-9 (visited on 08/17/2022).

[76] M. Thakkar, A. Busse, and N.D. Sandham. “Direct numerical simulation of turbulent channel flow over a surrogate for Nikuradse-type roughness”. In: *Journal of Fluid Mechanics* 837 (2018), R11–R111. ISSN: 14697645. DOI: 10.1017/jfm.2017.873.

[77] J. Kiefer. “Sequential Minimax Search for a Maximum”. In: *Proceedings of the American mathematical society* 4.3 (1953), pp. 502–506. URL: https://www.jstor.org/stable/2032161.

[78] M.H. Hosni, H. W. Coleman, J.W. Garner, and R.P. Taylor. “Roughness element shape effects on heat transfer and skin friction in rough-wall turbulent boundary layers”. In: *International Journal of Heat and Mass Transfer* 36 (1993), pp. 147–153.

[79] H.W. Coleman, R.J. Moffat, and W.M. Kays. “The accelerated fully rough turbulent boundary layer”. In: *Journal of Fluid Mechanics* 82.3 (1977), pp. 507–528. ISSN: 14697645. DOI: 10.1017/S0022112077000810.

[80] *Circle packing (hexagonal)*. URL: https://en.wikipedia.org/wiki/Circle_packing (visited on 08/10/2022).

[81] *Turbulence intensity*. URL: https://www.cfd-online.com/Wiki/Turbulence_intensity (visited on 03/22/2022).

[82] B. Latini, M. Fiore, and F. Nasuti. “Modeling liquid rocket engine coolant flow and heat transfer in high roughness channels”. In: *Aerospace Science and Technology* 126 (July 2022). ISSN: 12709638. DOI: 10.1016/j.ast.2022.107672.